UMONS
Université de Mons

Faculté
des Sciences

Analytical and numerical investigation of resonant phenomena based on hyperbolic metamaterial designs

Fabio Vaianella

Thesis presented in fulfilment of the requirements for the degree of
Doctor of Sciences

Thesis supervisor
Bjorn MAES

University of Mons
Faculty of Sciences
Micro- and Nanophotonic Materials Group

Academic year
2017-2018

Supervisor

Prof. Bjorn Maes	University of Mons (MMNP)

Jury members

Prof. Michel Voué	University of Mons (LPMO)
Prof. Patrice Mégret	University of Mons
Prof. Yan Pennec	Université de Lille, France
Dr. Gilles Rosolen	University of Mons
Dr. Joachim M. Hamm	Imperial College London, United Kingdom

University of Mons
Faculty of Sciences

Micro- and Nanophotonic Materials Group (MMNP)
Place du Parc 20
7000 Mons
Belgium

Tel.: +32-65/37.33.85
http://www.umons.ac.be/nanophot

This thesis was carried out in the context of a doctoral fellowship from the Fonds pour la Formation à la Recherche dans l'Industrie et dans l'Agriculture (FRIA-FNRS) - Wallonia (Belgium)

Acknowledgements

I would like to thank all the people who contributed, from a distance or close up, to the work described in this thesis.

My first thanks goes to my supervisor Prof. Bjorn Maes for giving me the opportunity to pursue a PhD thesis in his group, but also for his patience, availability and guidance. He scheduled regular meetings, gave accurate advices based on his knowledge or on an amazingly fast research in the literature.

I also thank Prof. Michel Voué and Prof. Patrice Mégret, members of my Support Committee for their interest in my work and for the constructive discussions we had, together with all the other members of my thesis jury.

My sincere thanks also goes to Dr. Joachim Hamm and Prof. Ortwin Hess for their thoughtful welcome at Imperial College and the possibility of living and working in London they offered me. My collaboration with them was precious to apprehend new theoretical framework and to widen my research from various perspectives. A particular thanks to Dr. Joachim Hamm who provided me his total support at any moment, if my stay in London was a success, it is mainly thanks to him.

I would also like to thank Dr. Shaojun Wang and Prof. Jaime Gomez-Rivas for the straight collaboration we have managed outside the framework of my thesis.

J'aimerais également remercier mes petits collègues de bureau sans qui ces quatres années de doctorat n'auraient pas été pareilles. Vous m'avez tous apporté des qualités essentielles pour la suite de ma carrière, à savoir: améliorer mes capacités de montages photographiques avec Mathieu Stock, entrainer mon agilité grâce aux défis de petites balles de Dr. Nicolas Rivolta, affiner mon humour avec les vidéos 'spéciales' de Corentin Guyot, devenir un nageur de haute compétition avec Galaad Altares et devenir champion de belote du Borinage grâce aux tournois de Dr. Gilles Rosolen. Et, bon, vous m'avez également aidé régulièrement sur des problèmes

scientifiques, c'est aussi à souligner.

Evidemment, mes remerciements ne se limitent pas uniquement aux collègues de bureau, mais également à toutes les personnes du 'couloir' des services de Physique des Particules Elementaires et de Physique des Matériaux et Optiques avec qui j'ai pu échanger quotidiennement dans la bonne humeur.

E per concludere questi ringraziamenti, vorrei ringraziare tutta la mia famiglia e amici per il loro sostegno senza limiti e per avermi sopportato fino alla fine, anche se concordo che non sempre è facile.

And, of course, thank you for reading those lines!

Summary

Metamaterials, photonic designs with subwavelength structures, have attracted tremendous interest over the last decades thanks to the new possibilities they offer to control electromagnetic fields. Among them, hyperbolic metamaterials have a plethora of interesting properties such as extreme photonic density of states, super-Planckian thermal radiation, negative refraction and the most famous capability to overcome the diffraction limit with the so-called hyperlens. Our goal is to explore hyperbolic metamaterials and to investigate their behaviours in various designs, which may have applications as photodetectors, sensors and lasing.

In this thesis we study the coupling mechanism of the elementary excitations of two-dimensional hyperbolic metamaterials and develop a method to describe their dispersion relations. We demonstrate this way an influence of the geometry, frequency regime and symmetry of the mode on the coupling. Next, we explore the scattering properties of tilted hyperbolic cavities and show that even extremely subwavelength cavities support Fano resonances thanks to the simultaneous excitation of propagating and evanescent modes. Furthermore, we study the physic of four-level dye infiltrated hyperbolic multilayers and demonstrate that ohmic loss compensation in these materials are accompanied by the generation of exceptional points, and, under certain conditions, also by strong coupling. Finally, we combine some of the previous results and explore the angular dispersion of dye-infiltrated tilted cavities and study the strong coupling regime with Fano resonances, highlighting phenomena such as absorption-induced transparency.

Contents

1

Introduction

1.1 State of the art

Electromagnetic properties of a material result from the interaction between waves and these materials. Various ways of manipulating light are thus possible by combining different media, such as dielectrics or metals. The scope of electromagnetic functionalities is thus mainly limited by the properties of the materials found in nature. To overcome this limit, novel platforms are synthesized at the molecular or atomic level to bring new capabilities, such as polytetrafluoroethylene (better known as Teflon, with a very low effective index and perfectly transparent from the deep-UV to the IR, over a large temperature range) [1] or more recently with two-dimensional materials like graphene [2] and transition metal dichalcogenide monolayers [3], but the range of applications is still limited by the material itself.

This is exactly where **metamaterials** come into play. The philosophy behind metamaterials is well resumed by the following quote of Nelson Mandela:

> *'It always seems impossible until it's done.'*

Indeed, the prefix 'meta' originates from the greek '$\mu\epsilon\tau\alpha$' meaning 'beyond', so metamaterials are an artificial platform that offers possibilities to steer light in a

manner beyond what is observed in nature with common materials. Unlike natural materials that take their optical properties from the interaction of light at the atomic or molecular level, metamaterials get their attributes from the interaction of light with a subwavelength architecture: the building blocks of metamaterials are thus not atoms or molecules, but functional inclusions often called 'meta-atoms' (Figure 1.1). The scale of these composite structures is still much smaller than the wavelength of interest and their electromagnetic responses can be expressed in terms of homogenized effective material parameters.

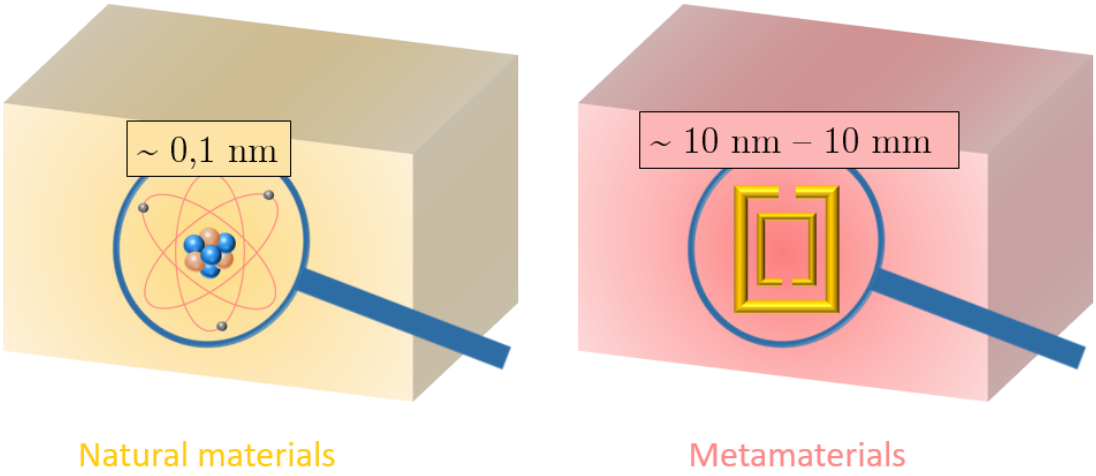

Figure 1.1: Key concept of natural materials (left) and metamaterials (right). Natural materials get their properties from the interaction of the electromagnetic field with the atoms ($\approx$ 0.1 nm) while metamaterials take their properties from subwavelength meta-atoms with size ranging from 10 nm to 10 mm depending on the frequency regime.

The first paper on the study of materials with properties not found in nature, opening the way to the new discipline of metamaterials, was written by Veselago in 1968 on the problem of left-handed materials, where he theorized the behaviour of an imaginary medium with both negative permittivity and permeability [4]. However, the field of metamaterials has really grown, in combination with the improvement of nanolithography, after the first experimental demonstration in 2000 of a left-handed material in the microwave regime by Smith *et al.* with an array of subwavelength nonmagnetic split-ring resonators [5]. This paper also marked the first use of the term 'metamaterial' to describe a medium that provides new properties from its subwavelength geometries, rather than from the materials it is built with.

In this field a particular recent class of metamaterials called 'hyperbolic metamaterials' (HMMs) aroused the curiosity of the scientific community, thanks to their astonishing applications and ease of fabrication, as shown by the growth of scientific literature on the subject (Figure 1.2). Originally introduced to overcome the diffraction limit with the description of the hyperlens [6, 7], HMMs also demonstrated an extremely broadband and large photonic density of states, super-Planckian thermal radiation and negative refraction [8, 9].

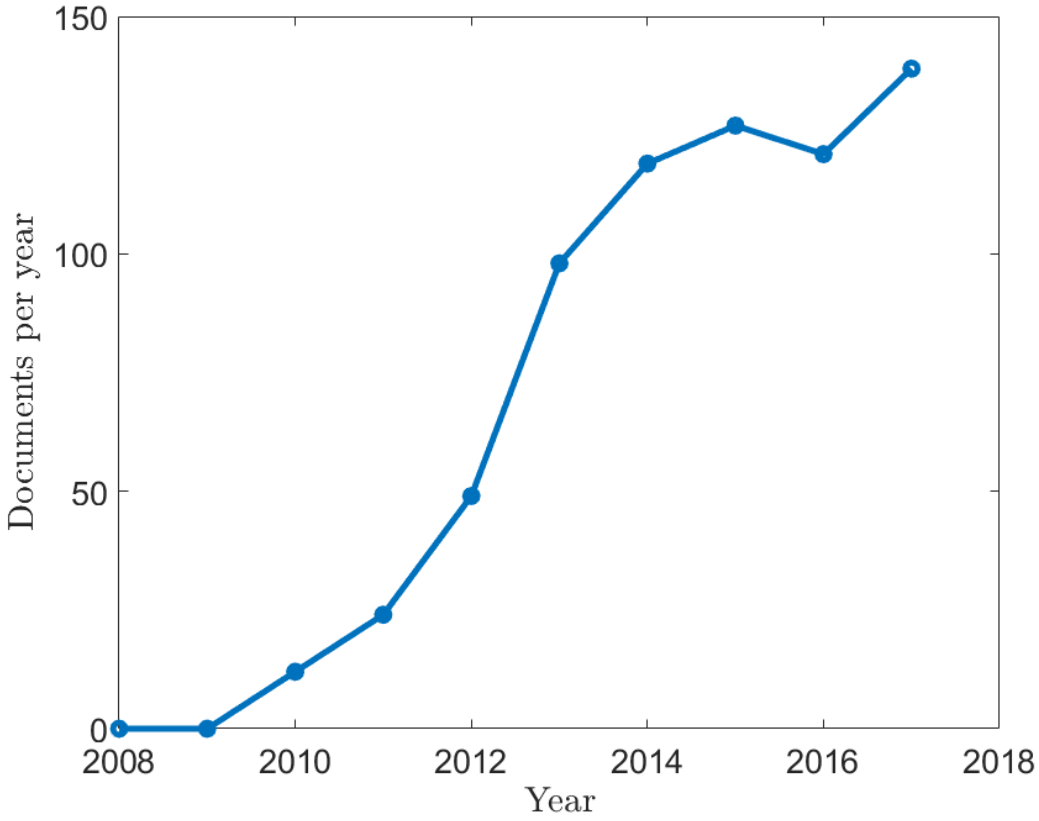

Figure 1.2: Documents published each year since 2008 containing the term 'hyperbolic metamaterial(s)' in the title or in the abstract, from the citation database Scopus [10].

The main directions of study for HMMs are the hyperlens [11, 12], spontaneous emission control [13–15], thermal emission engineering [16, 17], and active and tunable HMMs [18–22]. Very recently, the field explored other opportunities, such as the emergence of magnetic metamaterials that support both TE and TM hyperbolic polaritons [23], and the search for naturally hyperbolic two-dimensional transition metal dichalcogenides [24]. In this thesis we do not explore these directions (except for the active and tunability part) as they are already extensively examined in the literature. We rather study these structures for a fundamental analysis in Chapter 4, in connection with cavity and sensing applications in Chapter 5, for lasing and light-matter engineering in Chapter 6. We introduce these chapters in the next section.

1.2 Outline

This thesis is structured as follows. Chapter 2 describes the optical properties of dielectrics and metals (including a brief review on graphene). We then demonstrate how to homogenize a periodic multilayer of subwavelength metal and dielectric layers, and the appearance of hyperbolic properties. We present the limit of these ho-

mogenized models and compare it to the exact model with a transfer-matrix method description. Finally, we show analytically that the dispersion and features of hyperbolic multilayers originate from the coupling of the surface plasmon polaritons at each metal-dielectric interface of the stack.

Chapter 3 reviews the various resonant phenomena involved in the following chapters, and the methods used to model them. We start from the Fresnel coefficient description of a single interface between two media to explain Fabry-Perot resonances in cavities. We then explore more complicated phenomena such as Fano resonances that appear when a sharp resonant process interferes with a slowly varying background. Moreover, we develop a two-oscillator model to describe the effects of strong coupling and $\mathcal{PT}$-symmetry. Finally, we explain the two modeling methods used in this thesis, which are the finite element and transfer-matrix methods.

Then, Chapter 4 gives a detailed theory on the dispersion of two-dimensional arrays of deeply subwavelength metallic nanorods in a dielectric host. The dispersion is described via the coupling of specific 'elementary excitations' that exist inside these metamaterials. We numerically calculate the dispersion of these elementary structures and compare them systematically with the plasmonic bands of the full arrays. We show that there are various regimes of coupling, depending on the symmetry of the modes inside the plasmonic band, the frequency range and the size and shape of the nanorods.

Next, we deal in Chapter 5 with the scattering properties of a hyperbolic multilayer with a sudden tilting of the layers. In this way we create a cavity that is hyperbolic, but with the optical axis that is slanted with respect to the normal. We show that in this cavity, a propagating and an evanescent mode are always excited at normal incidence. The propagating mode is then responsible for narrow Fabry-Perot resonances while the evanescent mode provides an exponential output for light as a slowly varying background. The interference between these two distinct processes gives rise to sharp, highly asymmetric Fano resonances, even for extremely compact cavities. Furthermore, we demonstrate this general concept for tunable graphene-based multilayers, which is interesting e.g. for sensing applications.

In Chapter 6 we focus on the problem of ohmic loss compensation in hyperbolic metamaterials. Because of the metal content, many applications of HMMs are limited by their intrinsic losses. We semi-analytically and numerically study the impact of loss compensation using four-level dyes, and present a design to overcome the problem of light incoupling to realize population inversion of the emitters. We explore two regimes discriminated by the coupling strength of the dyes with the electromagnetic field. First, we demonstrate that the weak coupling strength corresponds to only a small perturbation of the discrete plasmonic modes (for finite stacks) or bands (for infinite stacks). Next, we show that large coupling strength leads to strong coupling and a fork'-like distortion of the hyperbolic modes of a finite hyperbolic stack at the absorption and emission lines, respectively. It turns out that exceptional points are generated at the plasmonic band edges when gain-loss compensation is achieved.

Chapter 7 combines concepts introduced in Chapters 5 and 6 and examines the angular dispersion of the Fano resonances of tilted multilayer cavities and their interaction with excitonic lines of absorption. We demonstrate that the conditions

for the generation of Fano resonances can be fulfilled even for non-normal incidence but with different physical processes. In particular, we expose that anisotropy is present in the cavity and this leads to the excitation of different modes depending on the energy flow direction, combined with the excitation of complex modes instead of purely evanescent modes. The transverse momentum inside the cavity controls the interference phenomenon between the slowly varying background generated by these complex modes and the anisotropic Fabry-Perot resonances, allowing to manipulate the shape and amplitude (or Fano parameter) of the resonances. We then introduce an excitonic line of absorption in the cavity and study the interaction with various resonances. We demonstrate a link between the Fano parameter and the Rabi splitting in the strong coupling regime, together with the existence of an absorption-induced transparency zone for specific angular incidences and anisotropic absorbances of the cavity.

Finally, Chapter 8 concludes the thesis with a brief review of the different results and an outlook.

1.3 Publications

The following is a list of contributions during the PhD work.

1.3.1 Publications in international journals

- **F. Vaianella**, G. Rosolen and B. Maes, Graphene as a transparent electrode for amorphous silicon-based solar cells, *Journal of Applied Physics*, vol. 117, 243102, 2015.

- **F. Vaianella** and B. Maes, Describing the dispersion of plasmonic nanorod arrays via coupling of elementary excitations, *Physical Review B*, vol. 93, 165417, 2016.

- **F. Vaianella** and B. Maes, Fano resonance engineering in slanted cavities with hyperbolic metamaterials, *Physical Review B*, vol. 94, 125442, 2016.

- **F. Vaianella**, J. M. Hamm, O. Hess and B. Maes, Strong coupling and exceptional points in optically pumped active hyperbolic metamaterials, *ACS Photonics*, vol. 5, 2486, 2018.

- **F. Vaianella** and B. Maes, Fano resonances in slanted hyperbolic metamaterial cavities in 'Fano resonances in optics and microwaves: Physics and application', Springer, 2018.

- S. Wang, Q. Le Van, **F. Vaianella**, B. Maes, S. Eizagirre Barker, R. Hjelmgart-Godiksen, A. Curto and J. Gomez-Rivas, Strong coupling of excitons in multilayer WS_2 with collective plasmonic resonances. In preparation.

- **F. Vaianella** and B. Maes, Angular dispersion and absorption-induced transparency in dye-infiltrated hyperbolic metamaterial cavities. In preparation.

1.3.2 Contributions in international conferences

- F. Vaianella and B. Maes, *Hyperbolic metamaterials: basic properties and formalism to describe the dispersion*, 18th Annual Workshop of the IEEE Photonics Society Benelux Chapter, Mons, Belgium, 2015.
- F. Vaianella and B. Maes, *Optimizing the geometry and losses in hyperbolic metamaterials*, Quantum Plasmonics, Benasque, Spain, 2015.
- F. Vaianella, B. Maes, *Describing the dispersion of hyperbolic metamaterials by elementary excitation coupling*, 20th Annual Symposium of the IEEE Photonics Society Benelux Chapter, Brussels, Belgium, 2016.
- F. Vaianella, B. Maes, *Analysis of 2D hyperbolic metamaterial dispersion by elementary excitation coupling*, SPIE Photonics Europe, Bruxelles, Belgium, 2016.
- F. Vaianella, B. Maes, *Strongly subwavelength cavities in multilayer hyperbolic metamaterials based on nanometric steps*, Meta'16 - 7th International Conference on Metamaterials, Photonic Crystals and Plasmonics, Malaga, Spain, 2016.
- F. Vaianella, B. Maes, *Fano resonance engineering in a slanted hyperbolic metamaterial cavity*, 21st Annual Symposium of the IEEE Photonics Society Benelux Chapter, Ghent, Belgium, 2016.
- F. Vaianella and B. Maes, *Exciting Fano resonances in structured hyperbolic metamaterials*, General Scientific Meeting of the Belgian Physical Society, Mons, Belgium, 2017.
- F. Vaianella and B. Maes, *Fano resonance excitations in slanted hyperbolic cavities*, 11th International Congress on Engineered Material Platforms for Novel Wave Phenomena, Marseille, France, 2017.
- F. Vaianella, J. M. Hamm, O. Hess and B. Maes, *Generation of exceptional points in dye-infiltrated hyperbolic metamaterials in the strong-coupling regime*, 22nd Annual Symposium of the IEEE Photonics Society Benelux Chapter, Delft, Netherlands, 2017.
- F. Vaianella, J. M. Hamm, O. Hess and B. Maes, *Exceptional points in the strong-coupling regime with active hyperbolic metamaterials*, SPIE Photonics Europe, Strasbourg, France, 2018.

1.3.3 Award

- *Umicore Materials Technology MSc Award 2015* for the Master thesis entitled 'Using graphene as a transparent and conductive electrode for photovoltaic cells'. The prize is awarded for original contributions in fields such as fine particles, sustainable energy, catalysis and economic and societal issues about metal-based materials.

2

Materials and hyperbolic multilayers

Metamaterials are artificial structures that obtain their astonishing properties from their subwavelength design - often called 'meta-atoms' - built from materials found in nature [25]. Even if the optical response of metamaterials is generally completely different from the one of their constitutive materials, it is important to study the optical properties of the latter.

In this chapter we review the mechanisms that are responsible for the electromagnetic behaviours of dielectrics in Section 2.1 and metals in Section 2.2. In Section 2.3 we discuss the effective medium theory of metal-dielectric composites, focusing on multilayer hyperbolic metamaterials, wich are periodic stacks of a metal and a dielectric with deeply subwavelength thicknesses, and present some of their interesting properties. Finally we use an exact formalism to explore the dispersion of these hyperbolic multilayers and explain how they originate from the coupling of their elementary excitations in Section 2.4.

2.1 Dielectrics

Dielectrics are a particular class of materials where the valence and conduction band are separated by a large band gap, typically larger than 5 eV. For this reason, electrons from the completely filled valence band cannot pass to the conduction

band, and no electrical current flow is allowed inside the material when applying a potential difference. For the same reason, dielectrics are usually transparent in the visible regime.

When applying an electric field to a dielectric, bound electrons will not flow as they will do in a metal. However, they will move slightly from their equilibrium position inducing dipole moments and causing the dielectric to be polarized. The interaction of light with these media in the linear regime can be analyzed using the constitutives equations [26]:

$$\mathbf{D} = \varepsilon_0 \mathbf{E} + \mathbf{P} = \varepsilon_0 (1 + \chi_e) \mathbf{E} = \varepsilon_0 \varepsilon_r \mathbf{E} \tag{2.1}$$

$$\mathbf{B} = \mu_0 (\mathbf{H} + \mathbf{M}) = \mu_0 (1 + \chi_m) \mathbf{H} = \mu_0 \mu_r \mathbf{H} \tag{2.2}$$

where $\mathbf{D}$ and $\mathbf{B}$ are the electric displacement and magnetic induction, $\mathbf{E}$ and $\mathbf{H}$ the electric and magnetic fields, $\mathbf{P}$ and $\mathbf{M}$ the polarization and magnetisation densities, χ_e and χ_m the electric and magnetic susceptibilities, ε_0 and μ_0 the free-space permittivity and permeability, and ε_r and μ_r the relative permittivity and permeability. In the following, we omit to use the subscript r for the relative quantities, which does not introduce notation ambiguities.

In this thesis we do not study optical structures with magnetic materials, so that $\mu_r = 1$ (or $\chi_m = 0$). Note that Equation 2.1 is valid only in the frequency domain and usually not in the time domain (especially for the high frequencies of the visible regime). The dispersion of dielectrics is directly obtained from Equation 2.1 combined with a damped oscillator model and we can show the dielectric function $\varepsilon(\omega)$, expressed in the classical Lorentz-Drude model, takes the form:

$$\varepsilon(\omega) = \varepsilon_b + \sum_i \frac{g_i \omega_i^2}{\omega_i^2 - \omega^2 - i\omega\gamma_i} \tag{2.3}$$

with g_i the oscillator strength, ω_i and γ_i the frequencies and damping constants of the resonant modes that exist in the dielectric and ε_b the intrinsic permittivity of the dielectric. The real part of the dielectric function is normally positive for a dielectric.

Typically, the resonant modes responsible for absorption and dispersion of the material are phonon resonances in the mid-infrared and infrared regime, and electron-hole transitions over the band gap in the UV regime. In the optical regime where we work however, there are usually no resonances and the dielectrics appears to be transparent and dispersionless. For this reason, we usually fix in our studies the dielectric function as a constant, and the dispersion of the metamaterial will arise exclusively from the metallic components that we describe in the next section.

In Chapter 6, where we explore active metamaterials, we introduce organic dyes inside the dielectric constituants of our structure to overcome ohmic losses of the metal. The excitonic transitions of these dyes introduce dispersion and gain/loss in the material, which means that its dielectric function cannot be considered as a constant anymore. To account for this effect, we developped a model to describe these transitions and the dielectric function takes the special form (see Appendix A for more details):

$$\varepsilon(\omega) = \varepsilon_b + \sum_i g_i L(\omega_i, \gamma_i) \tag{2.4}$$

with $L(\omega_i, \gamma_i)$ the second order Lorentzian line-shape complex function

$$L(\omega_i, \gamma_i) = -\frac{1}{\pi} \frac{2\omega_i}{(\omega^2 - \omega_i^2 - \gamma_i^2) + 2i\gamma_i} \tag{2.5}$$

using the same notations as in Equation 2.3. This form of the permittivity arises directly from Maxwell-Bloch equation and, unlike the typical form of Equation 2.3, allows to connect directly the coupling strength of the oscillator to the cross-section of the excitonic transition and thus the dipole matrix element and population density in the ground and excited states.

2.2 Metals

Metals are materials that have their Fermi level that sits inside a continuous energy band, which is partially filled with electrons. Consequently, any photon that interacts with a metal can excite an electron to a higher level. The electrons are thus free to move in this type of materials and to participate to the current flow. In contrast to dielectrics, light cannot propagate in the metal and penetrate inside it as an evanescent wave to a distance commonly smaller than 100 nm [27].

In this section we review the optical properties of metal in Section 2.2.1 and graphene (which is not properly a metal as we will discuss) in Section 2.2.2.

2.2.1 Free electron gas

As we did for dielectrics, the physics behind the optical properties of metals is derived directly from the constitutive equations (Equations 2.1 and 2.2) in combination with the motion equation of electrons, which we suppose are free to move. The equation of motion of a free electron driven by a time harmonic incident field is:

$$m\frac{\mathrm{d}^2\mathbf{r}(t)}{\mathrm{d}t^2} + m\gamma_m\frac{\mathrm{d}\mathbf{r}(t)}{\mathrm{d}t} = -e\mathbf{E}_0 e^{-i\omega t} \tag{2.6}$$

with m and e the effective mass and charge of the electron, γ_m the damping constant (or electron collision rate), $\mathbf{r}(t)$ the position vector of the electron, $\mathbf{E}_0$ the incident electric field amplitude and ω the frequency of the driving light. This movement of the electron creates an electrical dipole moment in the material equal to $\mathbf{p}(t) = -e\mathbf{r}(t)$.

The net polarization density $\mathbf{P}$ created by all the dipole moments is then given by:

$$\mathbf{P} = -ne\mathbf{r} = -\frac{ne^2}{m(\omega^2 + i\gamma\omega)}\mathbf{E}_0 e^{-i\omega t} \tag{2.7}$$

where we have replaced $\mathbf{r}$ by solving the equation of motion (namely Equation 2.6), with n the density of free electrons. Combining Equations 2.1 and 2.7, we finally arrive to the Drude model form of the dielectric function for a free electron gas:

$$\varepsilon_m(\omega) = 1 - \frac{\omega_p^2}{\omega^2 + i\gamma_m\omega} \tag{2.8}$$

where we introduce the plasma frequency

$$\omega_p = \sqrt{\frac{ne^2}{\varepsilon_0 m}} \tag{2.9}$$

which is the characteristic frequency resonance of the collective oscillation of the electrons in the metal, also called a plasmon. The real part of the permittivity of metals is negative for frequencies below the plasma frequency ω_p, which means that above this frequency metals start to behave like dielectrics.

In this thesis, we essentially use silver as metal since it is the best platform to be used in plasmonics in the visible regime when it comes to propagation of surface waves. Typical values of plasma frequency and damping rate for silver are $\omega_p = 1.26 \times 10^{16}$ rad/s and $\gamma_m = 5 \times 10^{13}\,\mathrm{s}^{-1}$.

One should note that at this time we did not talk about size effects on the optical properties of metals. However, the damping rate of metal is directly linked to the Fermi velocity v_F by $\gamma_m = v_F/l_c$, with l_c the mean free path of the electrons. When the size of the metallic structure is on the order of the free path of the electrons, the metal edges are physical boundaries that reduce the effective mean free path, and are also accompagnied by quantum effects, increasing the damping rate. In this thesis, we never use metallic layers thinner than 5 nm, which is the usual limit where these phenomena start to appear [8, 27]. We can thus omit these particulars and consider the damping rate as a constant.

2.2.2 Graphene

This section is of particular interest for our study in Section 5.4 on graphene-based hyperbolic metamaterials in the terahertz regime. Graphene is a bidimensional crystal of carbon atoms arranged in a honey-comb lattice, with inter-atomic distance of about 0.142 nm [28]. Graphene can support surface waves similar to the surface plasmon polariton at the dielectric-metal interface, which renders it usable for plasmonic applications [29, 30].

This material has the interesting property that its valence and conduction bands touch each other at the center of the reciprocal lattice, creating the so-called 'Dirac point', which means that graphene is a semi conductor with zero bandgap or a semi-metal. In the vicinity of the Dirac point, the energy dispersion is generally considered as linear [31], with the form:

$$E^{\pm}(k) = \pm v_F \hbar |k| \tag{2.10}$$

where $E(k)^{\pm}$ is the energy of the conduction (+) and valence (-) band, $v_F \approx 10^6\,\mathrm{ms}^{-1}$ the Fermi velocity, $\hbar$ the Planck constant and k the wavevector. This particular shape of the dispersion contrasts with the usual parabolic shape of classical materials, and provides graphene with outstanding transport properties.

There are two mechanisms that contribute to the conductivity of a single layer of graphene. One contribution is from the intraband electron-photon scattering processes (σ_{intra}), the other is related to the interband electron transitions (σ_{inter}), which means that the total conductivity of a single layer is $\sigma = \sigma_{intra} + \sigma_{inter}$. The

two contributions can be derived from the well-known Kubo-Greenwood formula [32]:

$$\sigma_{intra}(\omega, E_F) = \frac{2ie^2 k_B T}{\hbar^2 \pi(\omega + i\tau^{-1})} \ln\left[2\cosh\left(\frac{E_F}{2k_B T}\right)\right] \tag{2.11}$$

$$\sigma_{inter}(\omega, E_F) = \frac{e^2}{4\hbar}\left[\frac{1}{2} + \frac{1}{\pi}\arctan\left(\frac{\hbar\omega - 2E_F}{2k_B T}\right) - \frac{i}{2\pi}\ln\frac{(\hbar\omega + 2E_F)^2}{(\hbar\omega - 2E_F)^2 + (2k_B T)^2}\right] \tag{2.12}$$

with T the temperature (we use only room temperature 300 K), k_B the Boltzmann constant, E_F the Fermi level (or doping level) and τ the scattering lifetime of the carriers ($\approx 10^{-13}$ s). Note that σ_{intra} is similar to the Drude model of classical metals, which we have described in the previous section as Equation 2.8.

The conductivity can be linked to the permittivity of the single layer using the formula [33]:

$$\varepsilon(\omega, E_F) = 1 - \frac{i\sigma(\omega, E_F)}{\varepsilon_0 \omega d_g} \tag{2.13}$$

with d_g the thickness of a single layer of graphene ($\approx$ 0.5 nm). We do not use directly the permittivity in our simulations of Section 5.4, instead we describe the graphene with a surface current as boundary condition (so the thickness $d_g \to 0$), using the conductivities derived in Equations 2.11 and 2.12. In this way, we avoid the problem of meshing layers that have subnanometer dimensions when using finite element method (see Section 3.2.2), which would lead to large computational times.

2.3 Effective medium theory for metal-dielectric multilayers

As stated in the introduction of this chapter, metamaterials are artificial structures that obtain their properties from their building blocks. Usually, these building blocks are composed of metals and dielectrics, and the amazing properties of metamaterials arise from the contrast between the optical response of these two classes of materials.

When the inhomogeneity scale is much smaller than the used wavelength, light cannot see the features of the building blocks, and feels the metamaterial as an homogenous bulk material. Thus under this condition we can describe a microscopically heterogenous system as a macroscopically homogenous medium, usually presenting anisotropy [25, 34, 35].

The properties of this homogenized medium are also described by the constitutive equations, Equations 2.1 and 2.2. As a reminder, we do not explore the field of magnetic metamaterials, so only Equation 2.1 describing the relation between electric displacement and electric field is required for our purpose.

2.3.1 Effective parameters

Browsing through the literature, there is an incredibly large number of mixing rules to homogenize composite media, going from the most popular Maxwell-Garnett

theory [36, 37] and Bruggeman's model [38, 39], to less-known models such as the Looyengas formula and De Loor model [40, 41]. Each of these models has its advantages and disadvantages, and there is still not, to this day, a homogenized theory that works for every structure and every optical regime. The history of effective medium theory (EMT) begins more than a century ago and is still a hot topic today [42–45].

In this thesis we explore mainly 1D metamaterials based on a periodic stack of a metal and a dielectric with thicknesses of about 10 nm (much smaller than the wavelength in the visible regime), as shown in Figure 2.1. We then restrict the discussion to describe effective medium theory for this class of structures. In the following, the subscript m will refer to the metal and d to the dielectric.

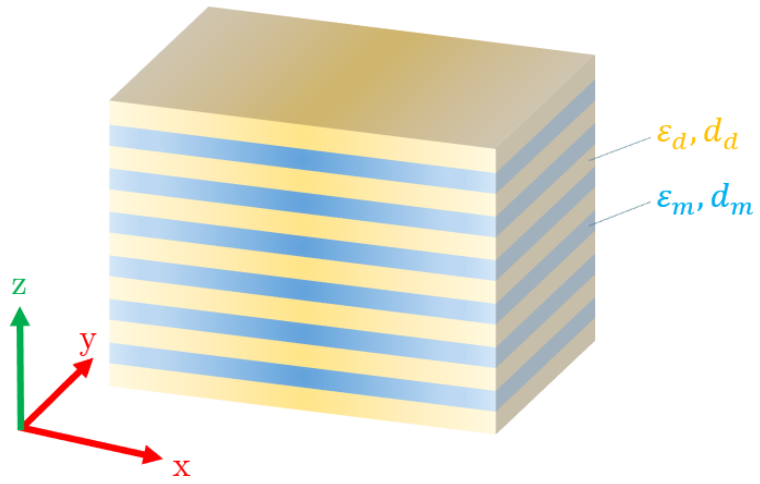

Figure 2.1: Multilayer of metal and dielectric with subwavelength thicknesses d_m and d_d. The metal has permittivity ε_m and the dielectric has permittivity ε_d.

Depending on the light polarization, the optical response of the multilayer is different. Indeed, when the incident wave is polarized parallel to the interfaces of the layers, from Maxwell equations we know the electric field needs to be continuous across each interface and supposing that the electric field is constant at the period scale (because the period is much smaller than the wavelength), we have:

$$E_d = E_m = E_{eff} \tag{2.14}$$

where E_{eff} is the electric field for the effective medium. We suppose the effective electric displacement D_{eff} to be equal to the weighted mean of the electric displacement in each layer, meaning that:

$$D_{eff} = \varepsilon_{\parallel} E_{eff} = f_d D_d + f_m D_m \tag{2.15}$$

and thus

$$\varepsilon_{\parallel} = f_d \varepsilon_d + f_m \varepsilon_m \tag{2.16}$$

where $\varepsilon_{\parallel}$ is the effective permittivity for a wave polarized in the xy-plane and $f_{d,m}$ the volume filling fraction of the dielectric and metal, respectively, defined as $f_{d,m} = \frac{d_{d,m}}{d_d + d_m}$, so that $f_m + f_d = 1$.

For a wave polarized in the direction normal to the growth direction (z direction), however, Maxwell equations state that the electric displacement is continuous across each interface, meaning (still supposing that the electric displacement is constant at the period scale):

$$D_{eff} = \varepsilon_{\perp} E_{eff} = D_m = D_d \tag{2.17}$$

In this scenario, the effective electric field is the weighted mean of the electric field in each layer so that:

$$E_{eff} = f_d E_d + f_m E_m. \tag{2.18}$$

Combining Equations 2.17 and 2.18 with the constitutive Equation 2.1 we find for the effective permittivity of waves polarized in z direction:

$$\varepsilon_{\perp} = \frac{\varepsilon_m \varepsilon_d}{f_d \varepsilon_m + f_m \varepsilon_d} \tag{2.19}$$

As we can see from our calculation of the effective parameters, the multilayer is anisotropic and its parameters do not depend on the thickness of the layers, but only on their relative filling fraction.

The effective permittivities (Equations 2.16 and 2.19) could have been derived from the famous Bruggeman's formula [38] which describes the effective response of a composite material where every constituent has a similar behaviour (unlike the Maxwell-Garnett model where one of the constituent is considered as the host matrix), with the formula:

$$f_m \frac{\varepsilon_m - \varepsilon_{eff}}{\varepsilon_m + \kappa \varepsilon_{eff}} + f_d \frac{\varepsilon_d - \varepsilon_{eff}}{\varepsilon_d + \kappa \varepsilon_{eff}} = 0 \tag{2.20}$$

where κ is the screening parameters of the external field. In this way, $\varepsilon_{\parallel}$ is the limit case when the field is aligned with the layer so that $\kappa \to \infty$ and $\varepsilon_{\perp}$ is the limit case when the field is normal to the layers so that $\kappa \to 0$.

2.3.2 Dispersion relation

As derived in the previous section, multilayers of metals and dielectrics are uniaxial crystals with permittivity tensor $\overline{\overline{\varepsilon}}$ as [8, 46]

$$\overline{\overline{\varepsilon}} = \begin{pmatrix} \varepsilon_{\parallel} & 0 & 0 \\ 0 & \varepsilon_{\parallel} & 0 \\ 0 & 0 & \varepsilon_{\perp} \end{pmatrix} \tag{2.21}$$

with $\varepsilon_{\parallel}$ and $\varepsilon_{\perp}$ that depend on the frequency.

To determine the dispersion relation of light in a medium described by Equation 2.21, let us consider the following two Maxwell's equations in the absence of sources:

$$\nabla \times \mathbf{E} = -\frac{\partial \mathbf{B}}{\partial t} \tag{2.22}$$

$$\nabla \times \mathbf{H} = \frac{\partial \mathbf{D}}{\partial t} \tag{2.23}$$

Using the constitutive equations (Equations 2.1 and 2.2) and using plane wave expressions for the field, we obtain:

$$\mathbf{k} \times \mathbf{E} = \omega \mu_0 \mathbf{H} \tag{2.24}$$

$$\mathbf{k} \times \mathbf{H} = -\omega \varepsilon_0 \bar{\bar{\varepsilon}} \mathbf{E} \tag{2.25}$$

Inserting Equation 2.24 in Equation 2.25 we find the relation

$$\mathbf{k} \times (\mathbf{k} \times \mathbf{E}) + \omega^2 \mu_0 \varepsilon_0 \bar{\bar{\varepsilon}} \mathbf{E} = 0 \tag{2.26}$$

which can be developed in matrix form as:

$$\begin{bmatrix} k_0^2\varepsilon_\parallel - k_y^2 - k_z^2 & k_x k_y & k_x k_z \\ k_x k_y & k_0^2\varepsilon_\parallel - k_x^2 - k_z^2 & k_y k_z \\ k_x k_z & k_y k_z & k_0^2\varepsilon_\perp - k_x^2 - k_y^2 \end{bmatrix} \begin{bmatrix} \mathrm{E}_x \\ \mathrm{E}_y \\ \mathrm{E}_z \end{bmatrix} = 0 \tag{2.27}$$

with k_0 the momentum in free-space.

The presence of nontrivial solutions imposes the determinant of the matrix to be equal to zero, and this leads to the dispersion relation (with $k_\parallel = \sqrt{k_x^2 + k_y^2}$):

$$(k_\parallel^2 + k_z^2 - \varepsilon_\parallel k_0^2) \left(\frac{k_\parallel^2}{\varepsilon_\perp} + \frac{k_z^2}{\varepsilon_\parallel} - k_0^2 \right) = 0 \tag{2.28}$$

When set to zero, the left factor corresponds to the dispersion of TE polarized waves (electric field along y direction, $\mathbf{E} = [0, E_y, 0]$ and $\mathbf{H} = [H_x, 0, H_z]$), and the right factor to the dispersion of TM polarized waves (magnetic field along y direction, $\mathbf{E} = [E_x, 0, E_z]$ and $\mathbf{H} = [0, H_y, 0]$).

We are particularly interested in the TM dispersion relation because the two components $\varepsilon_\perp$ and $\varepsilon_\parallel$ appear in its expression (and the surface plasmon polaritons that are responsible for hyperbolicity, as we discuss in the next section, are supported only in TM polarization). From Equations 2.16 and 2.19, thanks to the sharp contrast in the optical parameters of metals (negative permittivity) and dielectrics (positive permittivity), it is possible that the two components have opposite sign ($\varepsilon_\parallel.\varepsilon_\perp < 0$) and thus, the dispersion relation becomes the equation of a hyperbola. This is the reason metamaterials that have this property are called **hyperbolic metamaterials** (HMMs), which are the metamaterials we focus on this thesis.

Figure 2.2 shows typical value of the effective permittivities of a multilayer of silver (lossless Drude model) and TiO_2 ($n = 2.7$), with f_m=1/3. The zones highlighted in yellow are the regions where the components have opposite sign and the multilayer is thus hyperbolic.

We can distinguish two classes of hyperbolic metamaterials: HMMs of Type I when ($\varepsilon_\parallel > 0$, $\varepsilon_\perp < 0$), also called dielectric HMMs, and HMMs of Type II when ($\varepsilon_\parallel < 0$, $\varepsilon_\perp > 0$), also called metallic HMMs. Figure 2.3 shows the isofrequency surfaces (the surface of equal frequency in wavevector space) of an isotropic medium (a sphere), a typical anisotropic medium (an ellipsoid) and HMMS (two types of hyperboloid). Note that we use mainly Type II HMMs in this thesis since Type I HMMs with multilayers are usually obtained in the ultraviolet regime.

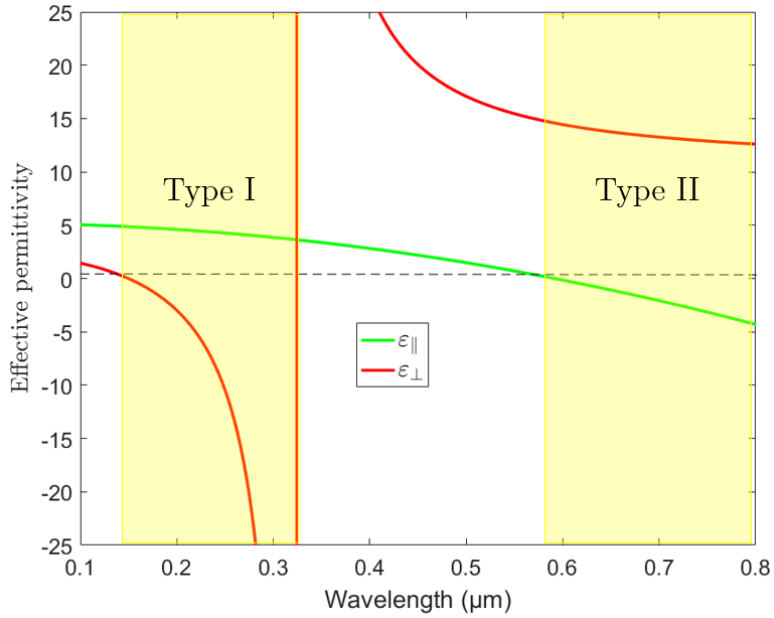

Figure 2.2: Effective parameters of a multilayer made of (lossless Drude model) silver and TiO_2 for a metal fill fraction f_m= 1/3. In the regions highlighted in yellow the multilayer is hyperbolic. The left yellow region is HMM Type I ($\varepsilon_\parallel > 0$, $\varepsilon_\perp < 0$), the right yellow region is HMM Type II ($\varepsilon_\parallel < 0$, $\varepsilon_\perp > 0$).

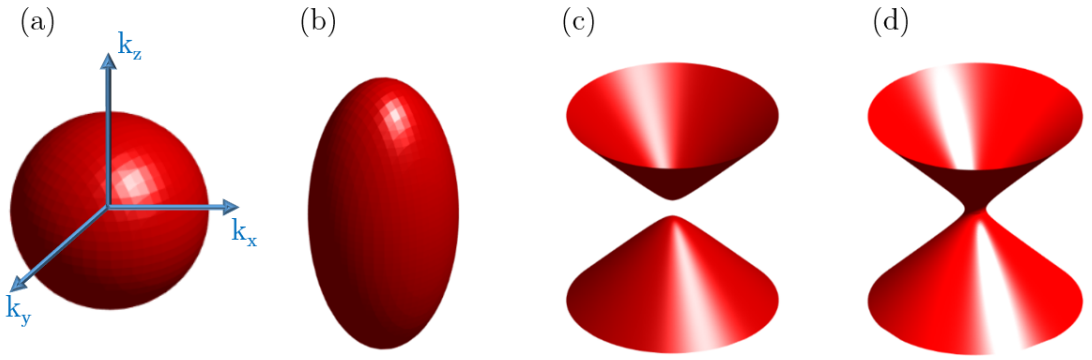

Figure 2.3: Typical isofrequency surface of: (a) an isotropic medium ($\varepsilon_\parallel = \varepsilon_\perp$), (b) an anisotropic medium ($\varepsilon_{\parallel,\perp} > 0$), (c) a HMM Type I ($\varepsilon_\parallel > 0$, $\varepsilon_\perp < 0$), (d) a HMM Type II ($\varepsilon_\parallel < 0$, $\varepsilon_\perp > 0$).

They key concept that offers HMMs their interesting properties stems from the special shape of their isofrequency surface: unlike isotropic or classical anisotropic media, their isofrequency surfaces are open surfaces, and the wavevectors inside HMMs are thus unbound, and could take infinite values (in theory, under effective medium theory and without loss).

2.3.3 Some properties and applications

As mentioned, the amazing properties and applications derive from the special shape of their isofrequency surfaces. The three major axes of applications are:

- *The hyperlens (exploiting the unbound wavector property).* When examining the Fourier decomposition of light emitted or scattered by an object, low momentum waves encode large geometric features, while high momentum waves encode smaller details. These large momentum waves cannot propagate inside isotropic and typical anisotropic media, because the maximum wavector is bound to the isofrequency surfaces, which are closed. In HMMs, however, propagating waves can have an infinitely large momentum, and one can overcome the diffraction limit, creating what we call *hyperlenses* [7]. Figure 2.4 shows an experimental realization [11].

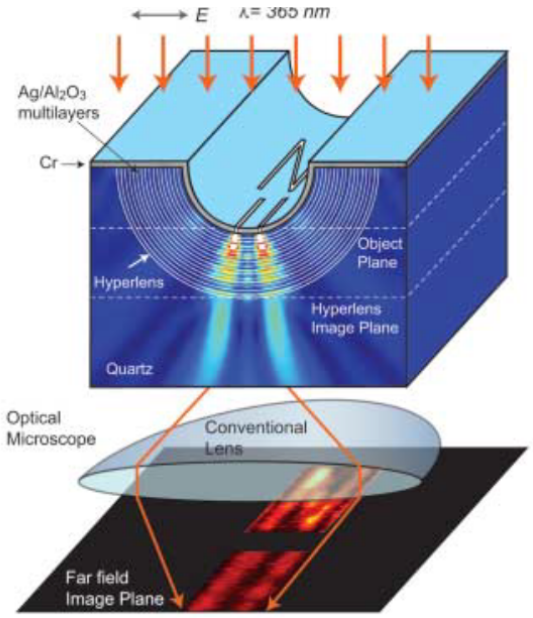

Figure 2.4: Schematic of a hyperlens and numerical simulation of imaging of sub-diffraction-limited objects. The high-k waves scattered by the features printed by nanolithography propagate inside the cylindrical HMM and can be resolved beyond the diffraction limit. Figure from [11].

- *Spontaneous emission control (exploiting the extremely high photonic density of states) and super-Planckian thermal emission.* Emission from dyes and quantum dots not only depends on their dipole moments, but also on the electromagnetic environment that surrounds them. This effect is called the Purcell effect. Usually, cavities or surface plasmon polaritons are used to decrease the lifetime of emitters, but these methods have the disadvantage of relying on a resonant process. However, when an emitter is placed inside or in proximity of a HMM, Fermi's golden rule tells that the emission rate is related to the density of states, which is extremely high for HMMs in a broadband fashion, as shown in Figure 2.5a [13]. Indeed, theoretically, for lossless HMMs the density of states is proportional to the shell volume between the isofrequency surfaces at ω and $\omega + \mathrm{d}\omega$ that is infinite, reducing drastically the lifetime of emitters in their vicinity as shown in Figure 2.5b [14, 15, 19]. The thermal emission beyond the black body limit arises from the same principle [16, 17].

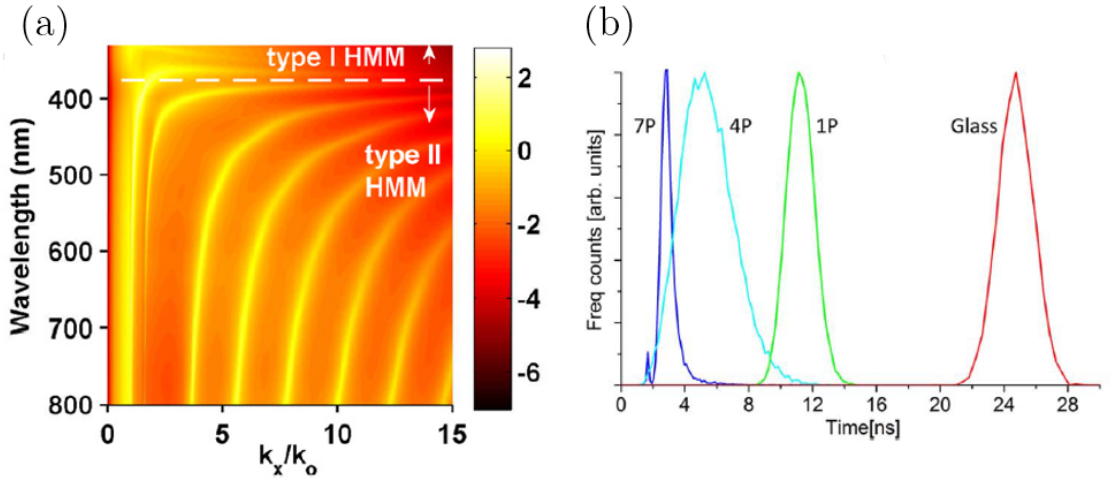

Figure 2.5: (a) Normalized local density of states in the near-field of an eight-layer HMM with effective medium theory in logarithmic scale. (b) Emitter lifetime when placed inside a HMM compared with glass as reference. Figure (a) from [13] and figure (b) from [19].

- *Negative refraction (from group velocity and phase velocity misalignment).* In conventional materials, the wavevector $\mathbf{k}$ and Poynting vector $\langle \mathbf{S} \rangle = \frac{\mathrm{Re}(\mathbf{E} \times \mathbf{H}^*)}{2}$ are aligned. However, in a HMM the wavector is constrained to the hyperbolic isofrequency contour, while the Poynting vector (or group velocity) is normal to it. As an example, Figure 2.6 shows the behaviour of light at the interface between an isotropic medium and a HMM (with $\varepsilon_x < 0$). At the interface, the transverse z component of the wavevector (k_z) is conserved. In the isotropic medium, the Poynting vector S_i is aligned with the wavevector and directed in the positive z direction, while in the HMM, it is normal to the isofrequency contour and $S_z = \frac{k_z}{\varepsilon_x} \frac{H_0^2}{2\omega\varepsilon_0} < 0$. The Poynting vector is thus directed in the negative z direction, meaning that energy undergoes negative refraction at the interface [18, 47].

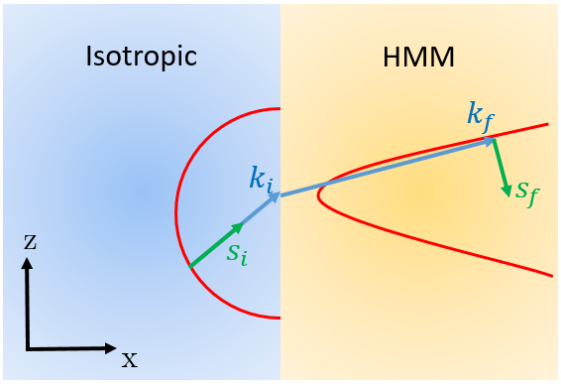

Figure 2.6: Negative refraction of light at the interface between an isotropic medium and a hyperbolic metamaterial. The red curves are the isofrequency contours in both media, blue arrows are the wavevectors and green arrows are the Poynting vectors.

2.4 Hyperbolic multilayers: exact formalism

In the previous section we analyzed the metal-dielectric multilayer as an effective medium using homogenization theory based on field averaging. However, this model fails to represent the rich physics of HMMs because it does not take into account the excitation of surface plasmon polaritons (SPPs) at each interface, and the extreme variation of field they are responsible for. A clear example of this effective medium breakdown is presented in Chapter 5.

We develop the exact dispersion relation of multilayer HMMs, and show the presence of a second mode caused by the non-local nature of SPPs in Section 2.4.1. We explain how this dispersion can be derived from the coupling of the elementary excitations of the stack in Section 2.4.2.

2.4.1 Exact dispersion relation

The exact dispersion relation in TM polarization of a metal-dielectric multilayer can be derived using a transfer-matrix method (more details in Section 3.2.1) combined with Bloch's eigenvalue equation as [48, 49]:

$$M\mathbf{b} = \lambda_{\pm}\mathbf{b} \tag{2.29}$$

with $\mathbf{b}$ the Bloch eigenvectors, $\lambda_{\pm} = e^{\pm ik_z D}$ the Bloch eigenvalues (where $D = d_m + d_d$ is the period and k_z the Bloch wavevector) and M the transfer matrix of a unit cell of the multilayer. M can be evaluated using the conversion matrix $U_{m,d}$ in the metal and dielectric and the propagation matrix $P_{m,d}$ (see Section 3.2.1 for the exact definition of these matrices) so that:

$$M = P_d(d_d/2)U_d^{-1}U_m P_m(dm)U_m^{-1}U_d P_d(d_d/2) \tag{2.30}$$

where we used a parity symmmetric unit cell with a metal layer of thickness d_m surrounded by two dielectric layers of thickness $d_d/2$. Solving the eigenvalue problem and using the fact that $(\lambda_+ + \lambda_-)/2 = \cos(k_z D) = \Lambda$, we obtain the dispersion relation (for TM waves):

$$\begin{aligned}\Lambda = \cos(k_z D) = &\frac{(\kappa_d\varepsilon_m + \kappa_m\varepsilon_d)^2}{4\kappa_d\kappa_m\varepsilon_d\varepsilon_m}\cosh(\kappa_d d_d + \kappa_m d_m) \\ &- \frac{(\kappa_d\varepsilon_m - \kappa_m\varepsilon_d)^2}{4\kappa_d\kappa_m\varepsilon_d\varepsilon_m}\cosh(\kappa_d d_d - \kappa_m d_m)\end{aligned} \tag{2.31}$$

with $\kappa_{d,m} = (k_x^2 - k_0^2\varepsilon_{d,m})^{1/2}$ the decay coefficients in the dielectric and metallic layers. The effective permittivities $\varepsilon_{\parallel,\perp}(\omega, \mathbf{k})$ depend thus on the wavevector and thicknesses of the layers, and not only on the frequency as we obtained using EMT. The underlying non-locality emerges from the plasmonic nature of the dispersion, with surface plasmon polaritons being supported at each metal-dielectric interface. Moreover, we can show that the typical plasmon saturation occurs at the SPP resonance frequency $\omega_{SPP} = \omega_p/\sqrt{1+\varepsilon_d}$, while the EMT predicts a saturation at the frequency $\omega_{EMT} = \omega_p/\sqrt{1+(d_m/d_d)\varepsilon_d}$ (resonant behaviour for $\varepsilon_\perp \to \infty$).

Analyzing the dispersion relation at the center of the Brillouin zone ($k_z = 0$), Equation 2.31 becomes:

$$\left[\frac{\kappa_d}{\varepsilon_d}\tanh\left(\frac{\kappa_d d_d}{2}\right)+\frac{\kappa_m}{\varepsilon_m}\tanh\left(\frac{\kappa_m d_m}{2}\right)\right].\left[\frac{\kappa_d}{\varepsilon_d}\cosh\left(\frac{\kappa_d d_d}{2}\right)+\frac{\kappa_m}{\varepsilon_m}\cosh\left(\frac{\kappa_m d_m}{2}\right)\right]=0 \tag{2.32}$$

and so, each bracket corresponds to the dispersion of a propagating mode. Thus, the multilayers support two plasmonic bands, and not one as predicted by the EMT, as shown in Figure 2.7. The presence of two propagating waves instead of one is a consequence of non-locality caused by SPPs at each metal-dielectric interfaces [50].

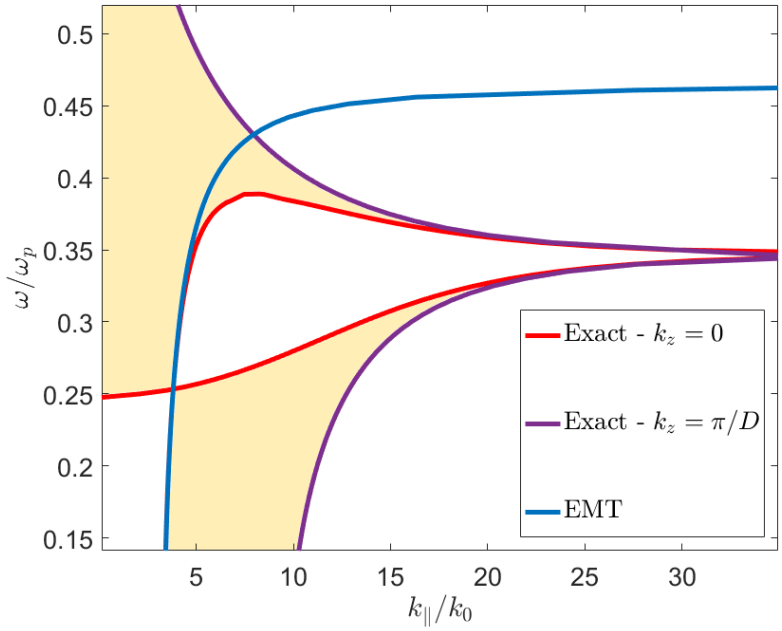

Figure 2.7: Typical plasmonic bands (highlighted in yellow) of a metal-dielectric multilayer HMM with $d_m < d_d$ (in this particular case, $d_d = 20$ nm and $d_m = 10$ nm). The red curves are the dispersion curves at the center of Brillouin zone ($k_z = 0$), purple curves are the dispersion curves at the edge of the Brillouin zone ($k_z = \pi/D$) and blue curve the dispersion curve obtained using the Bruggeman's effective medium theory described in Section 2.3.

2.4.2 Elementary excitation coupling

The metal-dielectric multilayer is nothing else than an infinite succession of metal-dielectric interfaces, each supporting SPPs. Looking simply at the bulk mode of the multilayer just as the coupling between the SPPs at each of these interfaces is however erroneous. The reason of this is because the coupling of the SPPs through the metal and through the dielectric is indeed not the same. In fact, we can write

the coupling strength between two adjacent SPPs as [51]:

$$c_d = \frac{1}{d_d}\int_0^{d_d} f_{SPP}(x) f_{SPP}(-x+d_d)\,\mathrm{d}x = e^{-\kappa_d d_d} \tag{2.33}$$

$$c_m = \frac{1}{d_m}\int_{-d_m}^{0} f_{SPP}(x) f_{SPP}(-x-d_m)\,\mathrm{d}x = e^{-\kappa_m d_m} \tag{2.34}$$

where c_d (c_m) is the coupling coefficient through the dielectric (metal) and f_{SPP} is the mode profile of the SPP across the interface. c_m and c_d are of course not equivalent generally.

It is however more correct to descrive the multilayer dispersion from the coupling of gap (metal-dielectric-metal structure) plasmons when $c_m > c_d$, or slab (dielectric-metal-dielectric structure) plasmons when $c_d > c_m$. The transition between the two regime occurs when $c_m = c_d$ and so:

$$\kappa_m d_m - \kappa_d d_d = 0. \tag{2.35}$$

Inserting this criterion (Equation 2.35) inside the two dispersion relations we have calculated at $k_z = 0$ (Equation 2.32), we prove that the two mode dispersions intersect when:

$$\kappa_m \varepsilon_d + \kappa_d \varepsilon_m = 0 \tag{2.36}$$

which occurs at the exact coordinates:

$$\omega_i = \frac{\omega_p}{\sqrt{1+\varepsilon_d \frac{d_d}{d_m}}} \tag{2.37}$$

$$k_{x,i} = \frac{\omega_i}{c}\sqrt{\frac{\varepsilon_d}{1-\frac{d_m}{d_d}}}. \tag{2.38}$$

We immediately conclude from Equation 2.38 that the two plasmonic bands intersect only if $d_m < d_d$ as we can see from Figures 2.8a and 2.8b.

Figure 2.8 shows that when $d_m > d_d$, the multilayer is always 'slab-like' and the slab plasmon dispersion is always at the center of the plasmonic bands. When $d_m < d_d$, however, both 'slab-like' and 'gap-like' regimes exist.

This result is of crucial importance when we want to design our multilayer HMM to yield a band structure with predefined desired properties. For instance, we apply this procedure in Chapter 6 with dye-infiltrated HMMs where we design our stack so that the excitonic lines of the dyes surround the intersection point. Furthermore, in Chapter 4, we show that the dispersion originates from the coupling of elementary excitations not only for multilayers, but a priori for any kind of HMMs. In particular, there we analyze the dispersion mechanism of arrays of square and rectangular metallic nanorods in a dielectric host. More useful than for multilayer, our results allow to quickly predict the dispersion behaviour of such metamaterials, even if they do not have analytical solutions up to this day.

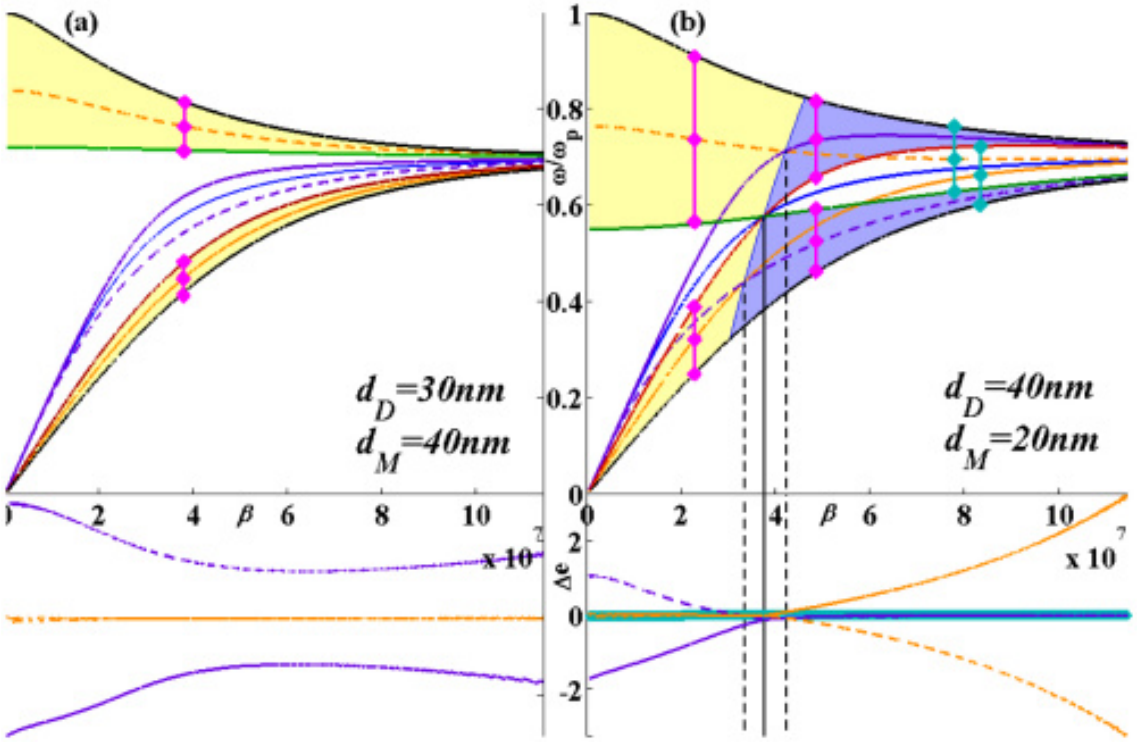

Figure 2.8: The two plasmonic bands of a periodic metal-dielectric stack when (a) $d_m > d_d$ and (b) $d_m < d_d$, along with the slab plasmon dispersion (yellow) and gap plasmon dispersion (purple). Lower subplots show the relative deviation between the center of plasmonic bands and the gap and slab dispersions [51].

3

Optical concepts and methods

This chapter introduces the basic theoretical concepts involved in our HMM structures in Section 3.1, and we discuss the semi analytical and numerical tools employed to describe them in Section 3.2. In particular, we review (in preparation of Chapter 5) the basic theory of Fabry-Perot cavities in Section 3.1.1, and examine a special type of asymmetrically-shaped resonances called 'Fano resonances' in Section 3.1.2. Sections 3.1.3 and 3.1.4 explore the theory of strong coupling and $\mathcal{PT}$-symmetry, which are of particular interest for Chapter 6 treating the interplay of hyperbolic modes with active media.

3.1 Resonant phenomena

3.1.1 Fabry-Perot cavities

Fabry-Perot cavities are characterized by two parallel partially transmitting mirrors that induce interference phenomena in reflection and transmission when illumunated by a plane wave. This interference is responsible for the apparition of resonances so that the transmittance (and reflectance) spectra are characterized by local maxima (minima) [52]. We first briefly review the theory of reflection and transmission of a single interface and then describe the properties of two-mirror based structures, which is essential for the comprehension of Chapters 5 and 7.

Fresnel coefficients

At the interface between two different media (noted 1 for the incident medium with refractive index n_1, and 2 for the transmission medium with refractive index n_2), an incident plane wave can either be reflected or transmitted. We can describe this phenomenon using the electromagnetic continuity equations (without external current and charge):

$$\widehat{\mathbf{n}} \cdot \{\mathbf{D}_1 - \mathbf{D}_2\} = 0 \qquad \widehat{\mathbf{n}} \cdot \{\mathbf{B}_1 - \mathbf{B}_2\} = 0 \tag{3.1}$$

$$\widehat{\mathbf{n}} \times \{\mathbf{E}_1 - \mathbf{E}_2\} = 0 \qquad \widehat{\mathbf{n}} \times \{\mathbf{H}_1 - \mathbf{H}_2\} = 0 \tag{3.2}$$

with $\widehat{\mathbf{n}}$ the unity vector normal to the interface (x direction in our study). For TE polarisation, where the electric field is normal to the incidence plane (y direction here), the continuity equations impose that the electric field is continuous across the interface, meaning that:

$$E_i + E_r = E_t \Rightarrow 1 + r_{TE} = t_{TE} \tag{3.3}$$

where E_i, E_r and E_t are the incident, reflected and transmitted electric field, respectively, $r_{TE} = E_r/E_i$ and $t_{TE} = E_t/E_i$ the Fresnel coefficients for reflection and transmission. Continuity of the tangential component of magnetic field imposes (using the Maxwell-Faraday equation for plane waves $\mathbf{H} = \frac{1}{\omega\mu_0}\mathbf{k} \times \mathbf{E}$):

$$-k_{x,1}E_i + k_{x,1}E_r = -k_{x,2}E_t \Rightarrow k_{x,1}(1 - r_{TE}) = k_{x,2}t_{TE}. \tag{3.4}$$

Combining Equations 3.3 and 3.4 we finally derive the expressions for the Fresnel coefficients:

$$r_{TE} = \frac{k_{x,1} - k_{x,2}}{k_{x,1} + k_{x,2}}, \qquad t_{TE} = \frac{2k_{x,1}}{k_{x,1} + k_{x,2}}. \tag{3.5}$$

The Fresnel coefficients for TM polarization are obtained in a similar way:

$$r_{TM} = \frac{n_2^2 k_{x,1} - n_1^2 k_{x,2}}{n_2^2 k_{x,1} + n_1^2 k_{x,2}}, \qquad t_{TM} = \frac{2n_1 n_2 k_{x,1}}{n_2^2 k_{x,1} + n_1^2 k_{x,2}}. \tag{3.6}$$

The energy flow of electromagnetic waves, carried by the Poynting vector $\mathbf{S}$ is defined as:

$$\langle \mathbf{S} \rangle = \frac{1}{2}\mathrm{Re}(\mathbf{E} \times \mathbf{H}^*) \tag{3.7}$$

and we can rewrite for plane wave excitation as:

$$|\langle \mathbf{S} \rangle| = \frac{\mathrm{Re}(k)}{2\mu_0\omega}|\mathbf{E}|^2 = \frac{\mathrm{Re}(n)}{2\mu_0 c}|\mathbf{E}|^2. \tag{3.8}$$

Using Equation 3.8 with the definition of the Fresnel coefficients (r, t), the transmittance T and reflectance R of light at an interface, valid for both polarizations, can be calculated as:

$$R = \frac{\langle S_r \rangle}{\langle S_i \rangle} = \frac{|E_r|^2}{|E_i|^2} = |r|^2, \qquad T = \frac{\langle S_t \rangle}{\langle S_i \rangle} = \frac{\mathrm{Re}(n_2)|E_t|^2}{\mathrm{Re}(n_1)|E_i|^2} = \frac{\mathrm{Re}(n_2)}{\mathrm{Re}(n_1)}|t|^2. \tag{3.9}$$

Two-interface cavities

Fabry-Perot cavities are structures with two partially transmitting mirrors separated by a distance L. For instance, a three-layer structure ($n_1 - n_2 - n_1$, where n_2 is the index of the cavity and n_1 of the surrounding layers) with large optical contrast is a typical Fabry-Perot cavity. At each interface, light can either be reflected or transmitted, generating outside the cavity interference from the multiple reflected or transmitted waves.

The reflection and transmission amplitudes for such a cavity, determined from the superposition of all plane waves at the output, normalized by the incident field, are given by:

$$r = \frac{E_r}{E_i} = r_{12} + \frac{t_{12}t_{21}r_{21}e^{2i\phi}}{1 - r_{21}^2 e^{2i\phi}}, \qquad t = \frac{E_t}{E_i} = \frac{t_{12}t_{21}e^{2i\phi}}{1 - r_{21}^2 e^{2i\phi}} \tag{3.10}$$

where the subscript '12' tells from medium 1 to medium 2' and with $\phi = k_x L$ the propagation phase. The reflectance and transmittance are obtained by taking the square of the norm of these amplitudes.

Resonances appear when constructive interferences occur, which is realized when the phase accumulated during a round-trip inside the cavity is equal to

$$2k_x L + \varphi_1 + \varphi_2 = 2m\pi \tag{3.11}$$

where m is an integer, φ_1 and φ_2 are the phases induced by the reflection at interface 1 and 2, respectively. The frequency separation between two resonances, for a dispersionless cavity, is:

$$|\Delta\omega| = \frac{\pi c}{n_2 L} \tag{3.12}$$

or, in terms of wavelength (also called the free-spectral range):

$$|\Delta\lambda| = \frac{\lambda_1 \lambda_2}{2n_2 L} \tag{3.13}$$

where λ_1 and λ_2 are two successive resonant wavelengths. This free-spectral range is an important quantity to define the finesse of the peaks $\mathcal{F}$ as:

$$\mathcal{F} = \frac{\Delta\lambda}{\delta\lambda} \approx \frac{\pi R_s^{1/2}}{1 - R_s}. \tag{3.14}$$

with $\delta\lambda$ is the full width at half maximum of the peaks and R_s the reflectance of the interface betweem medium 1 and 2. The Fabry-Perot resonances are thus more sharp when the reflectance of the interfaces is high. We use these properties in Chapter 5, where we tilt the layers of a multilayer HMM, leading to large effective index of the propagating mode in the cavity, and thus a large optical contrast and reflectivity at the interfaces.

3.1.2 Fano resonance

Ugo Fano developed in 1961 a theory to describe the asymmetrically-shape resonances in the studies of the Rydberg series for a phenomenon called auto-ionization [53]. This type of resonance, that arises from the interference between discrete quantum states and a continuum of states are well defined by the famous Fano formula:

$$\sigma(E) = D^2 \frac{(q+\Omega)^2}{1+\Omega^2} \tag{3.15}$$

where $\sigma(E)$ is the absorption spectrum or a scattering cross-section, E is the energy, $q = \cot\delta$ is the Fano parameter with δ the phase shift of the continuum, $\Omega = 2(E - E_0)/\Gamma$ with E_0 and Γ the energy and damping of the resonance, and $D^2 = 4\sin^2\delta$. Figure 3.1 shows typical Fano resonances for different Fano parameters q.

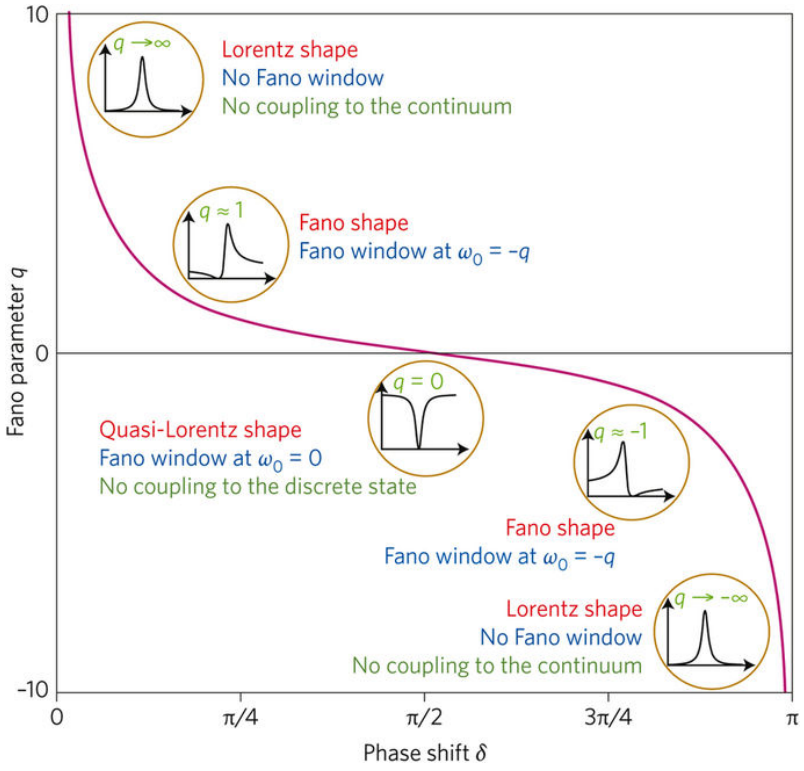

Figure 3.1: Typical Fano resonances for various limit cases of the Fano parameter q. Figure from [54].

The limit $q \to \pm\infty$ corresponds to the case where the external perturbation does not couple with the continuum, and the resonances thus have a typical lorentzian shape. The case $q = 0$ is the limit where the perturbation does not couple to the discrete state and the Fano has an inverted lorentzian shape, sometimes called anti-resonance. The case $q = 1$ is the typical picture of a Fano resonance, with the scattering going from a minimum to a maximum in a very sharp fashion.

Even if it was first observed in atomic physics, Fano resonances are present in practically every discipline, including photonics [54–56]. The spectrally asymmetric shape can for instance be derived in the scattering properties of a single-mode resonator coupled to two ports, using coupled mode theory (CMT), which we briefly describe in the following [57].

The temporal equation of CMT (using typical Dirac bracket notation $\langle v| = [v_1^*, v_2^*]$) is:

$$\frac{da}{dt} = \left(i\omega_0 - \frac{1}{\tau}\right) a + \left(\langle\kappa|^*\right)|s_+\rangle \tag{3.16}$$

$$|s_-\rangle = C|s_+\rangle + a|d\rangle \tag{3.17}$$

where a is the complex amplitude of the mode in the cavity, ω_0 and τ the frequency and lifetime of the resonance. s_+ and s_- correspond to the input and output excitations at the ports, respectively. $\langle\kappa|$ describes the coupling of the resonator with the input and $\langle d|$ for the output. In addition, the incoming and outgoing waves in the ports can also couple through a direct pathway with scattering matrix C.

Using time-reversal transformation and energy conservation one can show that $\langle d|$ and $\langle\kappa|$ are related to the other parameters by:

$$|\kappa\rangle = |d\rangle \tag{3.18}$$

$$\langle d|d\rangle = 2/\tau \tag{3.19}$$

$$C|d\rangle^* = -|d\rangle \tag{3.20}$$

For a structure with mirror symmetry, the problem is simpler with $d_1^2 = d_2^2$, and the scattering matrix for the direct process C has the special form:

$$C = e^{i\phi}\begin{pmatrix} r & it \\ it & r \end{pmatrix} \tag{3.21}$$

where r, t, ϕ are real constants with $r^2 + t^2 = 1$. Using Equations 3.19 and 3.20, we can determine the scattering matrix S of the system as:

$$S = e^{i\phi}\left[\begin{pmatrix} r & it \\ it & r \end{pmatrix} + \frac{1/\tau}{i(\omega-\omega_0)+1/\tau}\begin{pmatrix} -(r\pm it) & \mp(r\pm it) \\ \mp(r\pm it) & -(r\pm it) \end{pmatrix}\right] \tag{3.22}$$

with (+) sign corresponding to the case where the resonant mode is even, and (-) sign for the odd one. The related reflectance is therefore

$$R = \frac{r^2(\omega-\omega_0)^2 + t^2(1/\tau)^2 \mp 2rt(\omega-\omega_0)(1/\tau)}{(\omega-\omega_0)^2 + (1/\tau)^2} \tag{3.23}$$

which has a Fano asymmetric line shape.

In Chapter 5 we demonstrate Fano resonances in a HMM tilted cavity. These resonances arise from the simultaneous excitation of and interference between a propagating and an evanescent mode, the former providing for rapidly varying Fabry-Perot resonances, and the latter leading to a slowly varying background (the continuum or direct channel).

3.1.3 Strong coupling

The strong coupling regime is reached when the coherent energy exchange between two damped coupled oscillators is faster than their average dissipation rate. The

spectral signature of this effect is the splitting of the power dissipation spectrum, with the apparition of two distinct hybrid states [58, 59]. From the photonic point-of-view that interests us, in the strong coupling regime, light enters in a dressed state with matter transitions which leads to the generation of two distinct light-matter hybrid states (or polaritons).

A typical example is the strong interaction of an excitonic material inside a cavity, where the strong coupling between the excitonic absorption and the cavity mode gives rise to two independent hybrid polaritons, and so, two peaks of absorption instead of just one [60, 61].

We can describe this interesting regime using a damped coupled oscillator model, with just one driving force. The limit between the weak and strong coupling is different when using a classical or a quantum theory to describe these effects. We develop the two point-of-views in the following.

Classical model

The equation of motion for two damped coupled oscillators is given by:

$$\ddot{x}_i + \gamma_i \dot{x}_i + \omega_i^2 x_i - \Omega^2 x_j = F_i \tag{3.24}$$

where x_i are the displacement from equilibrium, $\dot{x}_i$ the speed, $\ddot{x}_i$ the acceleration, ω_i and γ_i the uncoupled resonance frequency and damping rate of the oscillator 'i' (with i=1, 2). Ω is the coupling constant between the two oscillators, F_i the driving force per mass on oscillator 'i'.

If we suppose a harmonic driving force only on oscillator 1 with frequency ω ($F_1 e^{-i\omega t}$), we can assume that the amplitude of the oscillators have the same harmonic dependence, so that $x_i(t) = x_{i0} e^{-i\omega t}$. The coupled equation of motion of Equation 3.24 can then be written in matrix form as:

$$\begin{pmatrix} \omega_1^2 - \omega^2 - i\gamma_1\omega & -\Omega^2 \\ -\Omega^2 & \omega_2^2 - \omega^2 - i\gamma_2\omega \end{pmatrix} \begin{pmatrix} x_1 \\ x_2 \end{pmatrix} = \begin{pmatrix} F_1 e^{-i\omega t} \\ 0 \end{pmatrix}. \tag{3.25}$$

Note that the same system of coupled equations could be used to describe the Fano resonances of the previous section, with $|\gamma_1| >> |\gamma_2|$ and $|\Omega^2| << |\gamma_1|$. The dissipated power of oscillator 'i' is $P_i = \omega^2 \gamma_i |x_i(\omega)|^2$, so we need the displacement from equilibrium of both oscillators. This can be easily extracted by inverting Equation 3.25 as:

$$\begin{pmatrix} x_1 \\ x_2 \end{pmatrix} = \frac{1}{Z} \begin{pmatrix} \omega_2^2 - \omega^2 - i\gamma_2\omega & \Omega^2 \\ \Omega^2 & \omega_1^2 - \omega^2 - i\gamma_1\omega \end{pmatrix} \begin{pmatrix} F_1 e^{-i\omega t} \\ 0 \end{pmatrix} \tag{3.26}$$

where $Z = (\omega_1^2 - \omega^2 - i\gamma_1\omega)(\omega_2^2 - \omega^2 - i\gamma_2\omega) - \Omega^4$.

If the two oscillators have different resonance frequencies $\omega_1 \neq \omega_2$, the exchange of energy is not efficient and the regime is similar to weak coupling. They must thus have the same resonance frequency $\omega_1 = \omega_2 = \omega_0$. A condition to see a splitting behaviour in the dissipated power is that $\Omega^2/(\omega_0(\gamma_1 + \gamma_2)) \geq 1$, which means it is necessary that the energy exchange between the two oscillators does more than one cycle before dissipation.

A typical strong coupling splitting is shown in Figure 3.2b, compared to the weak coupling regime in Figure 3.2a. As we can see in Figure 3.2b, the initial oscillators with resonances ω_0 are split in two resonances, one at a frequency $\omega_0 - \omega_{Rabi}/2$, the other at frequency $\omega_0 + \omega_{Rabi}/2$, with $\hbar\omega_{Rabi}$ the Rabi splitting energy (also sometimes called Autler-Townes splitting).

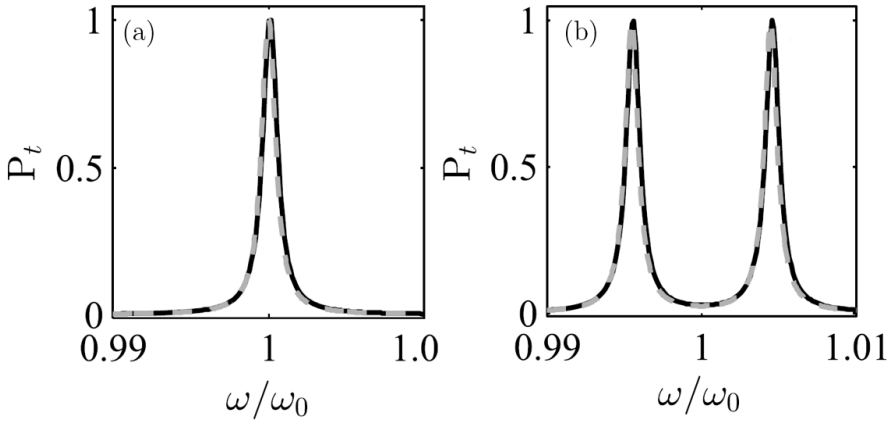

Figure 3.2: Total power dissipated by two damped coupled oscillators with the same resonance frequency when only one oscillator is driven by an external force. (a) In the weak coupling regime when $\Omega^2/(\omega_0\gamma) = 0.5$. In the strong coupling regime when $\Omega^2/(\omega_0\gamma) = 3$. Figure from [58].

Quantum model

The Hamiltonian describing the dynamics of a system of two damped coupled oscillators is non-hermitian, meaning that the energy spectrum is complex, with the imaginary part of the energy related directly to dissipation. As we have seen in the previous section, strong coupling is achieved only when $\omega_1 \approx \omega_2$. Dividing the first row of the 2×2 matrix on the left side of Equation 3.25 by $(\omega_1 + \omega)$ and the second row by $(\omega_2 + \omega)$, the equation of motion becomes (in the case $\omega_1 \approx \omega_2 \approx \omega$):

$$\begin{pmatrix} \omega_1 - i\gamma_1/2 - \omega & -\frac{\Omega^2}{2\omega} \\ -\frac{\Omega^2}{2\omega} & \omega_2 - i\gamma_2/2 - \omega \end{pmatrix} \begin{pmatrix} x_1 \\ x_2 \end{pmatrix} = \begin{pmatrix} 0 \\ 0 \end{pmatrix}. \tag{3.27}$$

The 2×2 matrix on the left side can be rewritten as $H - \omega I$, with I the identity matrix and H the Hamiltonian matrix (normalized by $\hbar$)[58, 62]:

$$H = \begin{pmatrix} \omega_1 - i\gamma_1/2 & g_c \\ g_c & \omega_2 - i\gamma_2/2 \end{pmatrix} \tag{3.28}$$

where $g_c = -\Omega^2/2\omega$ is the effective coupling constant.

A non-trivial solution of this system is possible only if $\det(H - \omega I) = 0$ which leads to the eigenfrequencies:

$$\omega_\pm = \tilde{\omega} \pm \sqrt{g_c^2 + \frac{\Delta^2}{4}} \tag{3.29}$$

with $\tilde{\omega} = (\omega_1 + \omega_2)/2 - i(\gamma_1 + \gamma_2)/4$ the average complex frequency of the uncoupled states and $\Delta = (\omega_1 - \omega_2) - i(\gamma_1 - \gamma_2)/2$ their detuning. When the states are lossless ($\gamma_1 = \gamma_2 = 0$) and degenerate ($\omega_1 = \omega_2$), $\Delta = 0$ and the two eigenstates of the coupled system are separated by the Rabi splitting energy $\hbar\omega_{Rabi} = \hbar|\omega_+ - \omega_-| = \hbar|g_c|$.

When $|g_c| << |\Delta/2|$, the eigenfrequencies $\omega_\pm = \tilde{\omega} \pm \Delta/2$ are just the frequencies of the bare states, showing that the influence of the coupling is weak and we can treat it as a perturbation. We cannot consider the system as perturbed as soon as $|2g_c/\Delta| \geq 1$, which is the quantum condition for strong coupling.

For use in Chapter 6 we have developed a semi-classical model to describe the coupling of excitonic lines in a one-dimensional periodic structure. This model is described in detail in Appendix A.

3.1.4 $\mathcal{PT}$-symmetry and exceptional points

An axiom of quantum mechanics states that the Hamiltonian operator H, expressing the dynamics of a system, must be Hermitian [63], meaning:

$$H = H^\dagger \tag{3.30}$$

where † stands for the Dirac Hermitian conjugation (combination of matrix transposition and complex conjugation). Hermicity ensures that the eigenvalues of H are real and that the time-evolution operator is unitary.

This statement was questioned in 1998, when Bender and Boettcher [64] made a breakthrough affirming that non-Hermitian Hamiltonian operators with parity-time ($\mathcal{PT}$) symmetry provide a real energy spectrum, and could thus describe quantum systems. This condition is weaker than requiring hermicity and thus opens the way to previously unknown phenomena [65]. An Hamiltonian is said to be $\mathcal{PT}$ symmetric if it commutes with the $\mathcal{PT}$ operator ($[H, \mathcal{PT}] = 0$). But because $\mathcal{PT}$ is not linear [$\mathcal{PT}(\lambda\phi) = \lambda^*\mathcal{PT}(\phi)$], the eigenstates of H are not necessarily eigenstates of $\mathcal{PT}$. One can show that if ϕ is an eigenstate of H and $\mathcal{PT}$, this imposes that the eigenvalue E of H related to this eigenstate is real.

If every eigenstate of H is also an eigenstate of $\mathcal{PT}$, then their eigenvalues are real and we say that the $\mathcal{PT}$ symmetry of H is unbroken. Conversely, if some eigenstates of H are not eigenstates of $\mathcal{PT}$, then their eigenvalues are not necessarily real and we say that the $\mathcal{PT}$ symmetry of H is broken.

By tuning some parameters of H, it is possible to pass from the broken phase to the unbroken phase, with drastic changes in the behaviour of the system. At the transition between these two regimes lies what is called an 'exceptional point', a point where the eigenvalues coalesce and are degenerate.

For a typical Hamiltonian of the form:

$$H = \frac{\hat{p}^2}{2m} + V(\hat{r}), \tag{3.31}$$

the condition for the Hamiltonian to be $\mathcal{PT}$ symmetric is that the potential V has the property (because the impulsion operator $\hat{p}$ is invariant through the $\mathcal{PT}$

operator):

$$V(\hat{r}) = V^*(-\hat{r}). \tag{3.32}$$

This condition means that the real part of the potential needs to be symmetric with respect to the operator P, unlike the imaginary part, which has to be antisymmetric.

The equivalent of the potential in the photonic field is the permittivity $\varepsilon(r)$, which must thus satisfy the conditions:

$$\begin{aligned} \mathrm{Re}\left[\varepsilon(r)\right] &= \mathrm{Re}\left[\varepsilon(-r)\right] \\ \mathrm{Im}\left[\varepsilon(r)\right] &= -\mathrm{Im}\left[\varepsilon(-r)\right], \end{aligned} \tag{3.33}$$

that is, the real part of the refractive index is symmetric, while the imaginary part (related to gain and loss) has to be antisymmetric.

A classical example to present the effect of $\mathcal{PT}$ symmetry is the directional coupler. A directional coupler is a simple structure consisting of two single-mode waveguides that couple with each other. For the coupler to be $\mathcal{PT}$ symmetric, it must satisfy the conditions of Equation 3.33, meaning that the two waveguides need to be identical (same real part of refractive index n_r), but one must experience gain ($\mathrm{Im}(\mathcal{N}_{eff}) = -\gamma$ with $\mathcal{N}_{eff} = n_{eff} - i\gamma$ the effective index of the unperturbed waveguide, n_{eff} the real part of the effective index and γ the gain/loss (positive) modal effective parameter) while the other experiences loss with the same magnitude ($\mathrm{Im}(\mathcal{N}_{eff}) = \gamma$).

The system is described by the equations [66]:

$$\frac{i}{k_0}\frac{d}{dz}\begin{pmatrix} c_1 \\ c_2 \end{pmatrix} = \begin{pmatrix} n_{eff} - i\gamma & g \\ g & n_{eff} + i\gamma \end{pmatrix}\begin{pmatrix} c_1 \\ c_2 \end{pmatrix} \tag{3.34}$$

with c_i the amplitude of the mode in waveguide 'i', and g the coupling constant between the two waveguides. The effective indices of the two supermodes are then given by:

$$\mathcal{N}_{\pm} = n_{eff} \pm \sqrt{g^2 - \gamma^2}. \tag{3.35}$$

Note the similarity between Equations 3.35 and 3.29, showing that $\mathcal{PT}$ symmetry is an analogue to the strong coupling regime for systems where the gain is exactly balanced by the loss ($\gamma_1 = -\gamma_2$). Figure 3.3 shows the typical 'fork-like' evolution of the effective indices of the two supermodes with the gain/loss parameter. When $\gamma < g$, the effective index of the two supermodes are real and they propagate without loss or gain. This regime is called the unbroken $\mathcal{PT}$ symmetry phase. When $\gamma > g$ we enter the broken $\mathcal{PT}$ symmetry phase where the real part of the effective indices are equal but the imaginary parts are opposite, wich means that one supermode experiences dissipation while the other is amplified.

At the junction of the two regimes lies an exceptional point (EP), a point where the two eigenmodes coalesce and are degenerate. These EPs present interesting physical properties, such as extreme spontaneous emission enhancement [67, 68], resonance narrowing, laser oscillation [69], and stopped light behaviour [70]. The latter stopped light is a crucial result for enhanced light-matter interaction [71].

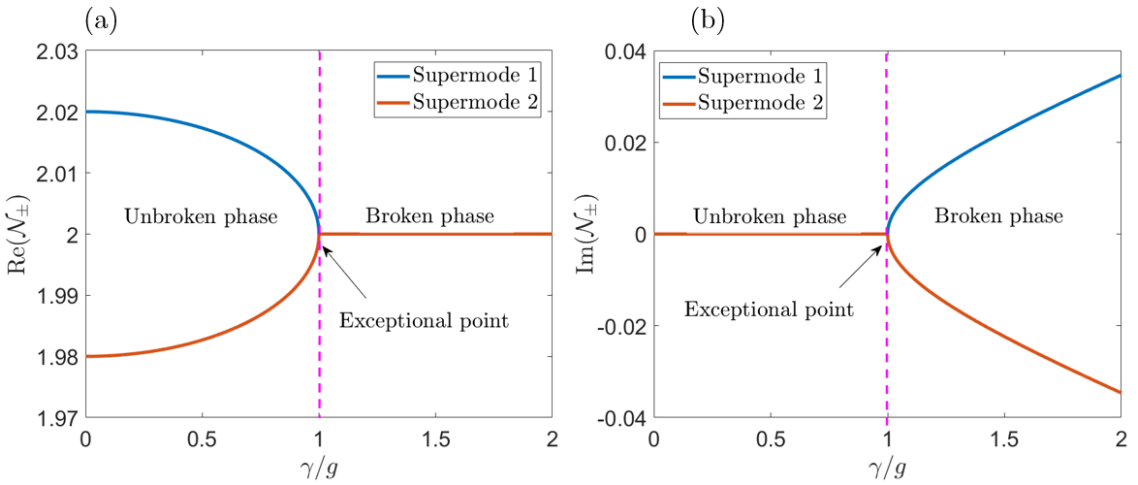

Figure 3.3: Evolution of the real (a) and imaginary (b) part of the effective indices $\mathcal{N}_\pm$ of the two supermodes as a function of the gain/loss factor γ. When $\gamma < g$ one has the unbroken phase, while when $\gamma > g$ one has the broken phase. At $\gamma = g$ the two supermodes coalesce and an exceptional point appears. We used $n_{eff} = 2$ and $g = 0.02$.

3.2 Semi-analytical and numerical methods

During this work we employ various methods to solve the electromagnetic Maxwell equations. In particular, in Chapters 4 and 5 the structures are too complex to resolve the equations completely in an analytical way. For this reason, we use the finite element method to analyze the optical response, and we introduce the method briefly in Section 3.2.2. Chapter 6 treats the physics of active stratified media, structures for which an analytical solution exists that can be derived with the transfer-matrix method, which we describe in Section 3.2.1.

3.2.1 Transfer-matrix method

This section introduces the transfer-matrix formalism necessary to understand the scattering properties of light in stratified media. This method is of particular interest for Chapter 6 where we study the interaction of quantum emitters in multilayers. We limit our presentation to nonmagnetic, linear and isotropic media, as these are the only materials used in this thesis.

If we examine the propagation of light in a given fixed direction, the transfer-matrix M links the amplitudes of the incoming and outgoing field from one side of the structure, to the amplitudes on the other side as:

$$\begin{pmatrix} A_U^+ \\ A_U^- \end{pmatrix} = M \begin{pmatrix} A_B^+ \\ A_B^- \end{pmatrix} \tag{3.36}$$

with the amplitude definition shown in Figure 3.4.

In each layer of the stratified medium, the electric and magnetic field are related

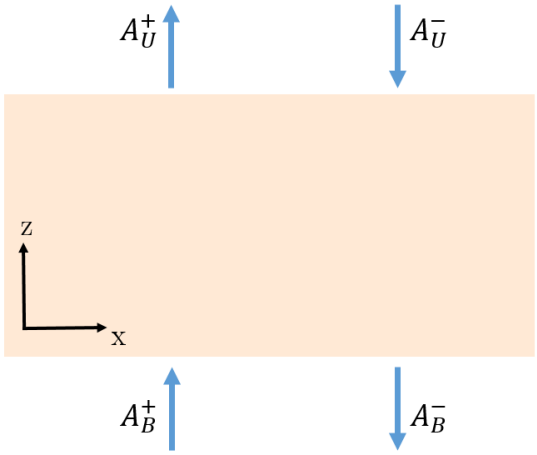

Figure 3.4: Definition of the amplitudes on each side of a structure linked by the transfer-matrix M.

to the amplitudes A by:

$$\begin{aligned} E_{\parallel} &= A^+ e^{ik_z z} - A^- e^{-ik_z z} \\ Z_0 H_{\parallel} &= Z_{\parallel}^{-1}(A^+ e^{ik_z z} + A^- e^{-ik_z z}) \end{aligned} \tag{3.37}$$

with $k_z = \sqrt{\varepsilon k_0^2 - k_x^2}$ the momentum in z direction (the direction normal to the layers), $Z_0 = \sqrt{\mu_0/\varepsilon_0}$ the wave impedance of free space and $Z_{\parallel}$ the impedance of the layer, depending on the polarization and defined as:

$$\begin{aligned} &\text{(TM)} \qquad \mathrm{Z}_{\parallel} = \frac{\mathrm{k_z}}{\varepsilon \mathrm{k_0}}, \\ &\text{(TE)} \qquad \mathrm{Z}_{\parallel} = \frac{\mathrm{k_0}}{\mathrm{k_z}}. \end{aligned} \tag{3.38}$$

The continuity at the interface being only relevant for the field and not for the amplitude, we need to define the conversion matrix U using equation 3.37 as:

$$\begin{pmatrix} E_{\parallel} \\ Z_0 H_{\parallel} \end{pmatrix} = U \begin{pmatrix} A^+ \\ A^- \end{pmatrix} = \begin{pmatrix} 1 & -1 \\ Z_{\parallel}^{-1} & Z_{\parallel}^{-1} \end{pmatrix} \begin{pmatrix} A^+ \\ A^- \end{pmatrix}. \tag{3.39}$$

The amplitude propagation over a distance d is represented by the propagation matrix P as:

$$\begin{pmatrix} A_2^+ \\ A_2^- \end{pmatrix} = P(d) \begin{pmatrix} A_1^+ \\ A_1^- \end{pmatrix} = \begin{pmatrix} e^{ik_z d} & 0 \\ 0 & e^{-ik_z d} \end{pmatrix} \begin{pmatrix} A_1^+ \\ A_1^- \end{pmatrix}. \tag{3.40}$$

With these two matrices, we can build the total transfer-matrix and describe the scattering properties of any stratified media (without current lines). If we suppose a layer 'i' of thickness d_i with permittivity ε_i, the transfer of the fields across this layer is:

$$M_i = U_i P_i(d_i) U_i^{-1}. \tag{3.41}$$

If we suppose a structure with a semi-infinite substrate (with subscript 1) and a semi-infinite superstrate (with subscript n), the total transfer-matrix of the multilayer is then just the product of each individual transfer-matrix:

$$M = U_n^{-1} \left(\prod_{i=2}^{n-1} M_i \right) U_1. \tag{3.42}$$

If we suppose an excitation from the top, from causality we have $A_B^+ = 0$ and we can fix arbitrarily $A_B^- = 1$. Then the reflectance R and transmittance T are easily extracted using the transfer-matrix formalism as $R = |A_U^+/A_U^-|^2$ and $T = |1/A_U^-|^2$. Note that we have already presented in Section 2.4.1 how to define and use the transfer-matrix to calculate the dispersion relation of a periodic multilayer.

3.2.2 Finite element method

We study complex structures that do not have analytical solutions up to this day. Some insights can be retrieved analytically, but exact solutions to the Maxwell equations usually require numerical methods. In particular, we use the commercial package COMSOL Mutliphysics, which implements the computational method called the 'Finite Element Method' (FEM) [72, 73].

The principle of FEM is to subdivide the structure we want to model in N finite subsections, building what is called a 'mesh'. In that way we transform the problem to a large set of linear equations solvable by matrix inversion techniques. This mesh is generally triangular (tetrahedral in 3D) as it allows to fit curved boundaries better compared to cubic or squared meshes required by other techniques (Figure 3.5). The desired function ψ is then approximated by an expression such as:

$$\psi(x, y, z) = \sum_{i=0}^{M} u_i b_i(x, y, z) \tag{3.43}$$

where b_i is a basis of known functions, and u_i are the coefficients to be determined using continuity of the field across elements and the boundary conditions. One then defines a suitable functional J, so that $\partial J/\partial u_i = 0$ when the set of u_i is solution to the equation.

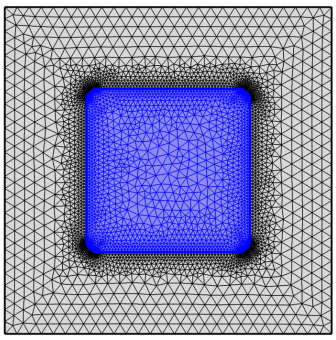

Figure 3.5: Triangular mesh of a rounded structure composed of two materials, typically studied in Chapter 4.

The *Wave Optics module* in COMSOL provides a wide range of modeling tools to solve time-harmonic electromagnetic field distributions. We mainly use two nodes for our simulations: the *Mode Analysis* node that we use to calculate the modes and disperion of a 2D cross-section of a waveguide (used in Chapter 4), and the *Boundary Mode Analysis* node that we use to calculate the modes of a given 1D periodic multilayer, which are then injected in the structure using a port boundary condition (used in Chapter 5).

4

Two-dimensional elementary excitation coupling

The multilayer we have presented in detail in Chapter 2 is not the only metal-dielectric design that provides hyperbolicity, leading to fascinating properties and applications such as a very large density of states [74, 75] and refractive index [76, 77].

In 2011 and 2013, two different groups showed that the hyperbolic properties in multilayer configurations (Figure 4.1a) arise from the plasmonic nature of the structure, and they are specifically explained as a competition between 'gap' modes (coupling of surface plasmons through the dielectric) and 'slab' modes (coupling of surface plasmons through the metal), as we have presented in Section 2.4.2 [51, 78, 79]. These studies provide for an intuitive picture to describe the modal properties in a 1D setting, by comparing the Bloch modes (judiciously averaged over the Brillouin zone (BZ)) with 'elementary' structures.

However, surface plasmon polaritons of planar metal-dielectric interfaces are clearly not the only plasmonic design at our disposal. For example, another typical structure that offers the same type of hyperbolicity is an array of cylindrical metallic nanorods in a dielectric host [80, 81].

In this chapter we discuss another type of 2D plasmonic array that is also hyperbolic. An extension of the theory developed in Section 2.4.2 for the 1D multilayer is

presented for this different design. In particular, with this extended procedure we study the dispersion of arrays of square and rectangular silver nanorods in a TiO_2 host (Figure 4.1b). The method is in this case more complex because of the higher number of modes and because of the 2D nature of the BZ for the transverse Bloch components (k_x, k_y). In addition, there are more elementary modes to consider, compared to the 1D case.

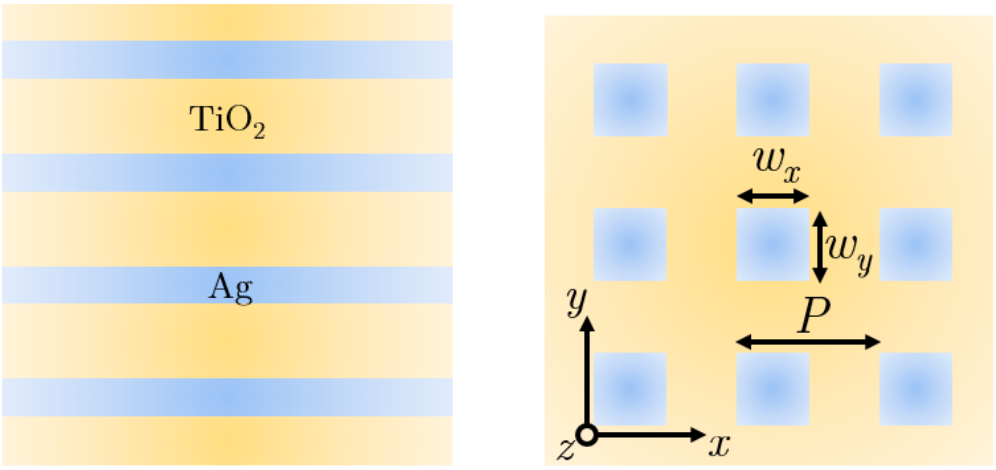

(a) (b)

Figure 4.1: (a) Multilayer consisting of periodic subwavelength layers of metal (silver (Ag)) and dielectric (TiO_2). (b) Geometry consisting of an array of square (or rectangular) silver nanorods in a TiO_2 host. w_x and w_y are the size of the nanorods in the x and y directions, respectively. P is the period of the array. $w_x = w_y = w$ for square nanorods.

We show that the dispersion of the array arises from the coupling of elementary excitations, and the particular basic structure depends on the size of the nanorods. For small and large square nanorods, the elementary geometries are a single rod and a four-corner structure, respectively. The intermediate size case arises from various elementary excitations in function of the frequency range and mode symmetry. Finally, for rectangular nanorods (one dimension much larger than the other) we find a good description via two coupled semi-infinite rods.

In Section 4.1 we explain the geometries, the notation and the analysis procedure. In Section 4.2 we examine the dispersion of arrays of small (compared to the period) square nanorods. In Sections 4.3 and 4.4 arrays of large and medium size nanorods are treated, respectively. Finally, in Section 4.5 we break the symmetry between the x and y directions with rectangular nanorods, and we conclude in Section 4.6.

4.1 Methods

4.1.1 Geometries

We study the dispersion of arrays of silver square and rectangular nanorods of various size in a dielectric TiO_2 host. From the discussion in Chapter 2 on the material

response in the visible regime, we take a dispersionless refractive index for TiO_2 of $n = 2.7$. We avoid the problem of complex wavevector propagation in this study by taking a lossless Drude model for silver from Equation 2.8:

$$\varepsilon_{Ag}(\omega) = 1 - \frac{\omega_p^2}{\omega^2} \tag{4.1}$$

with $\omega_p = 1.26 \times 10^{16}$ rad/s the plasma frequency.

We slightly round the corners of the rods (via quarter circles of 1 nm radius) in order to avoid extreme hotspots for the simulations. The influence of the period is not considered here, we fix the period of all structures to $P = 30$ nm, which is much smaller than the wavelength in the range analysed (from visible to near infrared spectrum).

For the square nanorod arrays, three cases are examined: a first case with the width w of the rods being much smaller than the period (we choose $w = 8$ nm, Figure 4.2a, analysed in Section 4.2). A second case with the width of the rods slightly smaller than the period (we choose $w = 25$ nm, Figure 4.2b, analysed in Section 4.3), and a third case with an intermediate width (we choose $w = 16.3$ nm, Figure 4.2c, analysed in Section 4.4).

Figure 4.2: Single unit cell of the structures under study: array of square nanorods with period $P = 30$ nm and nanorod width (a) $w = 8$ nm, (b) $w = 25$ nm, (c) $w = 16.3$ nm. (d) Array of rectangular nanorods of width $w_x = 20$ nm and $w_y = 10$ nm. (e) Reciprocal lattice and first Brillouin zone (in red). For square nanorod arrays, the irreducible Brillouin zone is the triangle delimited by the Γ, X_1 and M points. For rectangular nanorod arrays, the irreducible Brillouin zone is the square delimited by the Γ, X_1, X_2 and M points.

For these three cases the x and y directions are equivalent because the structures are invariant under rotation of 90° (the mode propagates along the z direction, out of the page here). The irreducible Brillouin zone is a triangle (Figure 4.2e) delimited by three important points: the center of the BZ Γ where $k_x = k_y = 0$, the $X_1(X_2)$ point where k_x (k_y) is equal to $\frac{\pi}{P}$ and the M point where $k_x = k_y = \frac{\pi}{P}$.

We also study rectangular nanorods where we break the x, y symmetry (with x direction width $w_x = 20$ nm larger than y direction width $w_y = 10$ nm, Figure 4.2d). In this case, the irreducible Brillouin zone is the square delimited by the four points Γ, X_1, X_2 and M.

Unlike the simple multilayer case, purely TM propagating modes do not exist here. All modes present the six components of the fields [82]. Thus it is very difficult

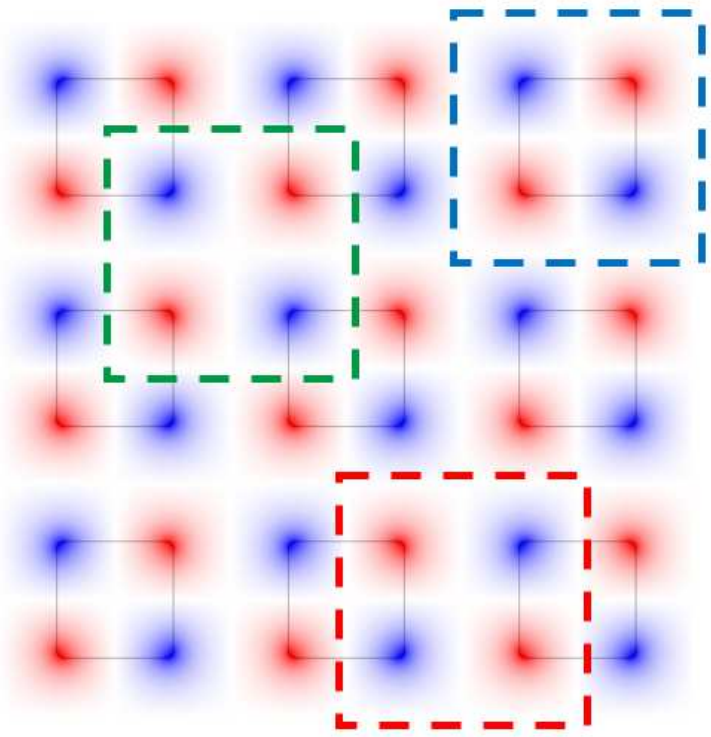

Figure 4.3: Lattice under study, which can be described from different viewpoints. The blue rectangle represents single-rod excitations. The green rectangle represents four metallic corners connected via dielectric. The red rectangle associates with structures made of two coupled (semi-infinite) rods. Shown is the z component of the electric field E_z for the aa mode (at the Γ point, $k_x = k_y = 0$) for the medium size square nanorod array at the wavelength $\lambda_0 = 700$ nm.

to analytically study these lattices, and we employ the numerical software COMSOL Multiphysics 5.1, with a mode solver based on the finite element method.

To obtain the dispersion of the structure the solver calculates the modes at a given frequency and provides the propagation constant of these modes. For the periodic arrays we simulate only one unit cell of the geometry with Floquet conditions at the lateral boundaries, with predetermined values for k_x and k_y. For the elementary geometries we do not use perfectly matched layers, as the modes are confined enough and a computational width of 200 nm with scattering boundary conditions suffices.

In analogy with the multilayer case, we look for elementary excitations or 'simpler' structures that can describe the array dispersions. To guide our search, the arrays can be seen as lattices with different bases (Figure 4.3): a lattice of single rods (blue rectangle), a lattice of four metallic corners connected via a dielectric medium (green rectangle) or a lattice of two coupled rods (red rectangle).

The simplest excitation here is no longer the surface plasmon polariton (as for the multilayer), but the plasmonic mode guided by a metallic corner. This corner plasmon can couple to neigbouring corners: through a dielectric layer, via a metallic edge or with a combination (through dielectric in one direction and via metallic edge in another direction). This leads to three elementary structures: the single-rod

structure (Figure 4.4a), the four-corner structure (Figure 4.4b) and the coupled-rod structure (Figure 4.4c), respectively. According to the size of the nanorods, we will see that the array dispersion seems to be associated with one of these elementary excitations. Note that various other fundamental geometries can be constructed, but analysis showed they do not corroborate well with the array modes.

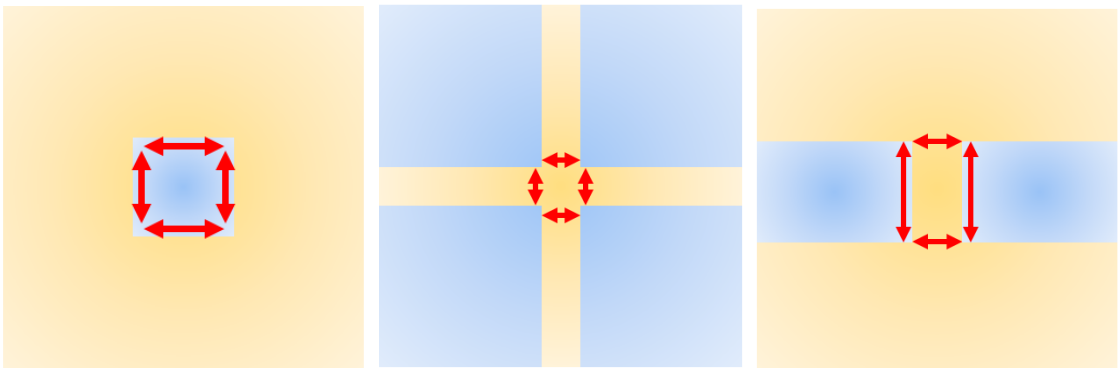

(a) (b) (c)

Figure 4.4: Elementary structures: (a) single rod in an infinite dielectric host. (b) Four metallic corners connected via dielectric medium. (c) Two coupled semi-infinite rods. Red arrows indicate the principal ways of coupling between corners.

4.1.2 Notations

Unlike the multilayer case, where only two different guided modes are present (a symmetric and an asymmetric one), four different symmetries for guided modes exist in our structures (Figure 4.5). We use a notation similar to the one adopted in [82] to indicate the mode.

A mode is described by two letters, the first letter represents the symmetry of E_z along a rod side in the x direction, and this letter can be "a" asymmetric or "s" for symmetric along x. The second letter represents the symmetry along a rod side in the y direction, with the same modalities. We only focus on the lower frequency modes, so an extra notation for the order of the mode is not needed.

The four possibilities are thus the *aa* mode (Figure 4.5a), *as* mode (Figure 4.5b), *sa* mode (Figure 4.5c) and *ss* mode (Figure 4.5d). The same nomenclature is used for the elementary structures.

Note that the *sa* and *as* modes for the arrays of square nanorods at the Γ and M points are degenerate because the x and y directions are equivalent and a rotation of 90° maps the Γ point to itself and maps the M point to the $\tilde{\mathrm{M}}$ point, which is related via a vector of the reciprocal lattice (Figure 4.2e). However, the *sa* and *as* modes are not degenerate at the X_1 (or X_2) point because a rotation of 90° maps the X_1 (X_2) point to the X_2 ($\tilde{\mathrm{X}}_1$) point that is not connected via a vector of the reciprocal lattice.

For the elementary structures, the *sa* and *as* modes are degenerate for the single-rod and the four-corner structure, because of 90° rotation equivalence, but they are not degenerate for the coupled-rod case (no 90° symmetry).

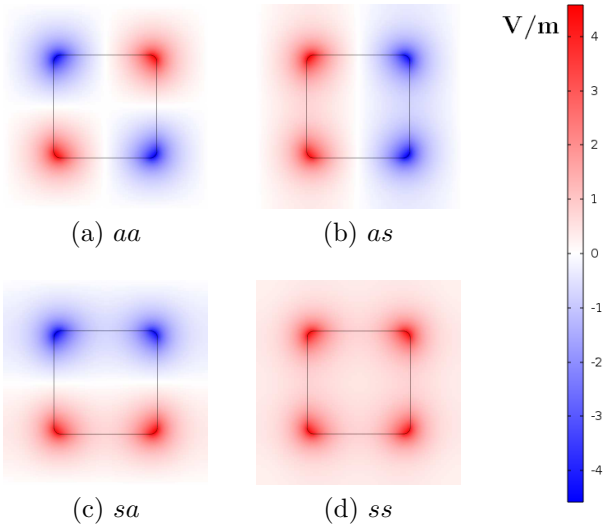

(a) *aa* (b) *as*

(c) *sa* (d) *ss*

Figure 4.5: E_z profiles of the electric field over a single unit cell for an array mode at the Γ point for $w = 16.3$ nm at $\lambda_0 = 700$ nm. (a) *aa* mode. (b) *as* mode. (c) *sa* mode. (d) *ss* mode.

Finally, the rectangular nanorod array modes and their elementary structure modes are not degenerate because the equivalence between the x and y directions is broken.

4.1.3 Dispersion analysis method

We introduce a 2D extension of the method used in [51]. They showed that the mean of the plasmonic band dispersion of a multilayer closely corresponds to the dispersion of elementary excitations of the structure ('slab' or 'gap' modes), providing for an intuitive picture to understand the 1D array modes.

In the case of 2D arrays of square nanorods, where the irreducible Brillouin zone is a triangle, the mean of the plasmonic band is calculated as

$$\omega_m(k_z) = \frac{\omega_a(\Gamma, k_z) + \omega_a(\mathrm{X}_1, k_z) + \omega_a(\mathrm{M}, k_z)}{3} \tag{4.2}$$

For arrays of rectangular nanorods, where the irreducible Brillouin zone is a square we use

$$\omega_m(k_z) = \frac{\omega_a(\Gamma, k_z) + \omega_a(\mathrm{X}_1, k_z) + \omega_a(\mathrm{X}_2, k_z) + \omega_a(\mathrm{M}, k_z)}{4} \tag{4.3}$$

with $\omega_m(k_z)$ the mean of the plasmonic band for a given propagating constant k_z. $\omega_a(\Gamma, k_z)$, $\omega_a(\mathrm{X}_1, k_z)$, $\omega_a(\mathrm{X}_2, k_z)$ and $\omega_a(\mathrm{M}, k_z)$ are the frequencies of the propagating mode of the periodic array at the Γ, X_1, X_2 and M points, respectively.

In analogy with the 1D case, we assume that a good correspondence between the mean of the plasmonic band and the dispersion of an elementary structure indicates that the array modes 'arise' from the modes of this elementary geometry. The nature of the basic structure will depend on the size and shape of the nanorods in the array. Mathematically, this assumption is simply

$$\omega_m(k_z) \approx \omega_e(k_z) \tag{4.4}$$

where $\omega_e(k_z)$ is the frequency of the elementary excitation for a given k_z.

One should pay attention that the symmetry of a given mode at the center of the Brillouin zone (Γ) is not necessarily the same at the X_1 and M points, so it requires caution when using equations 4.2 and 4.3 to calculate the mean of the plasmonic band, and to choose the adequate elementary mode.

A detailed application of this procedure is given in the next Section.

4.2 Small nanorods

We examine the dispersion for arrays of small (compared to the period) square nanorods with a width $w = 8$ nm. Using equation 4.2, we calculate the mean of the plasmonic band for each mode. In this case, the symmetry of each mode does not change between the Γ, X_1 and M points.

Figure 4.6 shows the dispersion for the small nanorod case at each specific point of the BZ. All the modes approach the horizontal asymptote defined by $\omega = 0.255\,\omega_p$, which is typical for the single corner plasmon mode. This effect is because the modes are tightly confined to the corners at this frequency, so that no coupling occurs between them. As we point out in Section 4.1.2, the *sa* and *as* modes are degenerate at the Γ and M points (red curve in Figure 4.6a and Figure 4.6c), but not degenerate at the X_1 point (red and magenta curves in Figure 4.6b).

Figure 4.6d shows the utilisation of the procedure described in Section 4.1.3 for the *ss* mode. We apply equation 4.2 to calculate the mean of the plasmonic band (black dashed curve), thus the average of the *ss* dispersion at the Γ (red curve, Figure 4.6d), X_1 (green curve, Figure 4.6d) and M (blue curve, Figure 4.6d) points. This mean is then compared to the three elementary structure dispersions in Figure 4.7d, to determine which one best describes the array.

Now Figure 4.7 shows this mean for each mode, and compares it with the three elementary modes of the same symmetry. We clearly see that the calculated mean corresponds perfectly with the dispersion of the single-rod geometry for each mode (the dashed black curve overlaps well with the blue curve).

Therefore, according to our assumption (equation 4.4), the elementary excitation that best describes the array mode seems to be the single rod structure, which comprises of four corners that are connected via metal-dielectric interfaces (the four sides of the rods). The single-rod being the 'basic' excitation is also intuitively acceptable in these small rod arrays, as the rods are too far from each other for efficient coupling.

4.3 Large nanorods

We proceed with the same treatment for large square nanorod arrays ($w = 25$ nm). Again, using equation 4.2 we calculate the mean of the plasmonic band for each mode. However, unlike the small nanorod case, the symmetry of the mode changes between the Γ, X_1 and M points, so that the modes need to be chosen carefully to apply equation 4.2. A summary of the mode symmetry changes is given in Table 4.1.

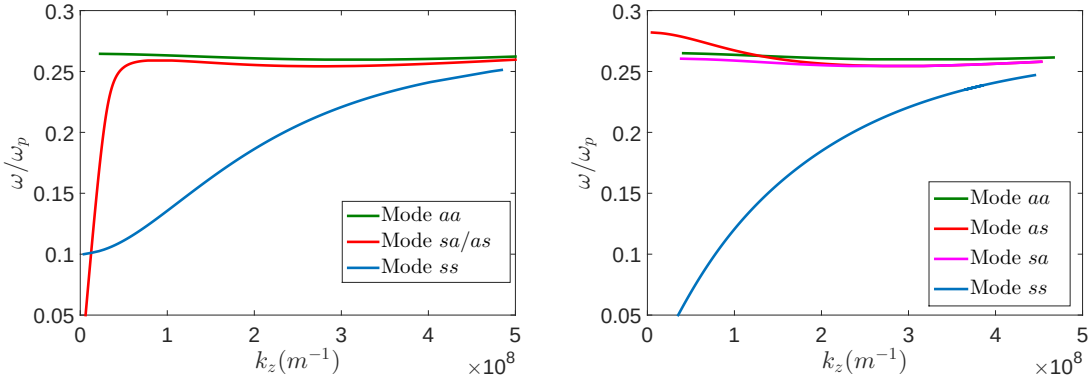

(a) Γ

(b) X_1

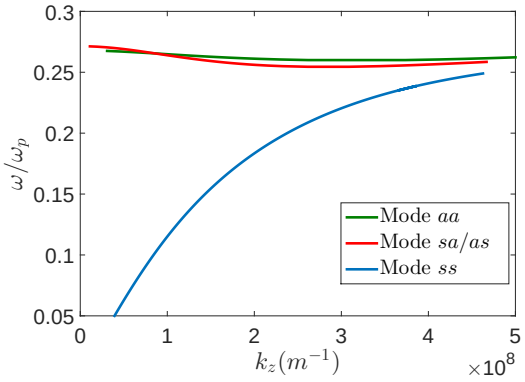

(c) M

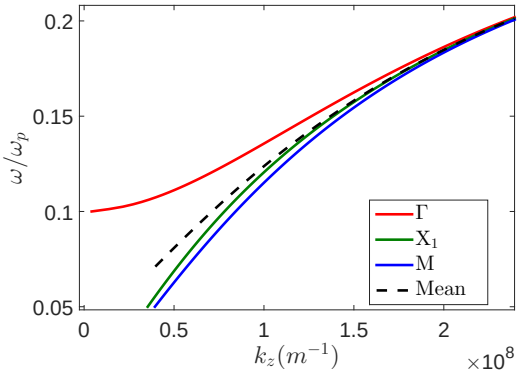

(d) ss

Figure 4.6: Dispersion of small square nanorod array ($w = 8$ nm). (a) At the Γ point ($k_x = k_y = 0$). (b) At the X_1 point ($k_x = \frac{\pi}{P}$, $k_y = 0$). (c) At the M point ($k_x = k_y = \frac{\pi}{P}$). (d) Mean of the dispersion calculated using equation 4.2 for the ss mode (black dashed line).

Γ$(0,0)$	$X_1(\frac{\pi}{P},0)$	M$(\frac{\pi}{P},\frac{\pi}{P})$
aa	sa	ss
as	ss	sa
sa	aa	as
ss	as	aa

Table 4.1: Symmetry changes for large square nanorod arrays in function of the Bloch wavevector for a given k_z. Each row corresponds to a particular mode. This Table is also valid for the medium size nanorod array above $\omega = 0.246\omega_p$.

We see that when the wavevector in the x direction changes from $k_x = 0$ to $k_x = \frac{\pi}{P}$, the symmetry in the x direction changes from symmetric to asymmetric (and vice versa). When the wavevector in the y direction changes from $k_y = 0$ to $k_y = \frac{\pi}{P}$, the same phenomenon occurs for the y-symmetry.

Figure 4.8 shows the mean for each mode and compares it again with the elementary excitations of the same symmetry. In this case, the calculated mean cor-

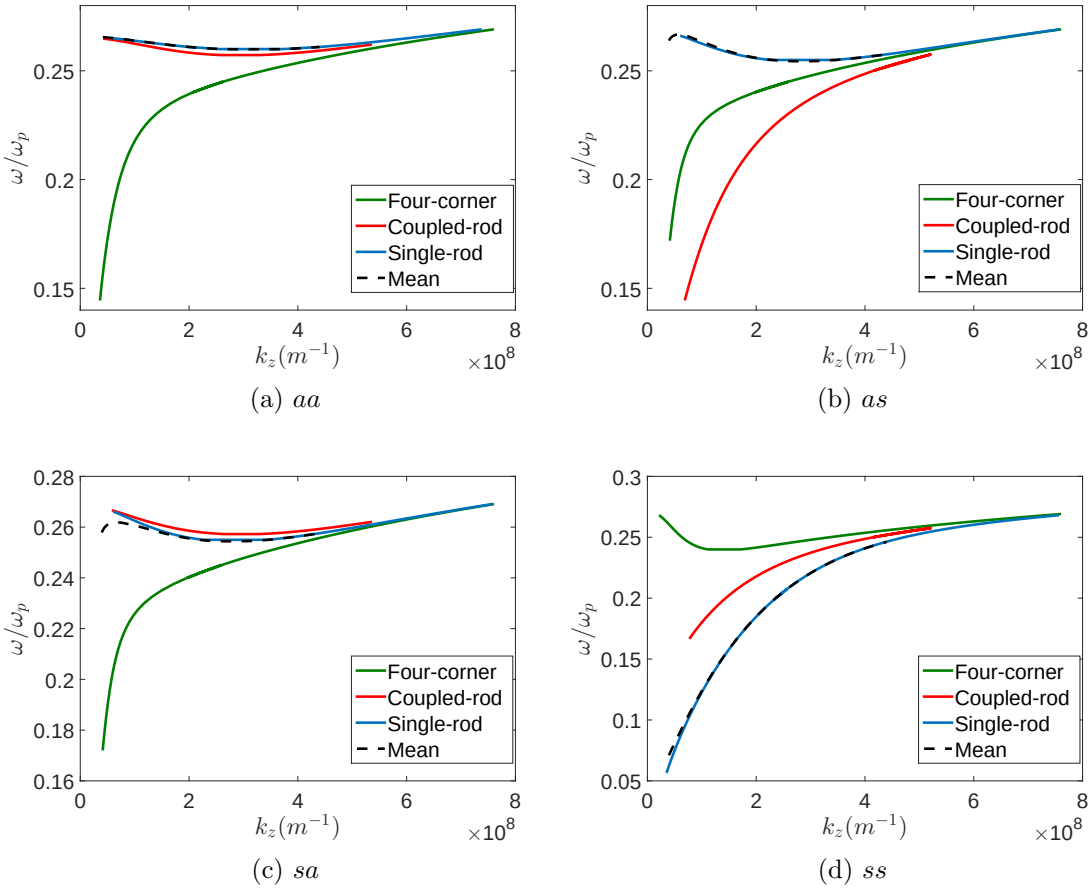

(a) *aa* (b) *as*

(c) *sa* (d) *ss*

Figure 4.7: Comparison between the mean calculated with equation 4.2 and the three possible elementary excitations for the small nanorod array. For each graph, the green curve corresponds to the four-corner structure, red curve corresponds to the coupled-rod, blue curve corresponds to the single-rod and black dashed curve correspond to the calculated mean. (a) For *aa* mode. (b) For *as* mode. (c) For *sa* mode. (d) For *ss* mode.

responds very well with the dispersion of the four-corner structure for each mode. This implies that the plasmonic mode of the large nanorod array originates from the four-corner structure, thus the plasmonic corners mainly couple through the dielectric (Figure 4.4b).

This statement is also confirmed by the field plots of the lattice at the three specific BZ points, see for example Figure 4.9 for the profiles of the *aa* band (first row of Table 4.1). At the three BZ points the same pattern emerges (Figure 4.9a-c) and this pattern is very similar to the *aa* mode of the four-corner structure (Figure 4.9d), which is thus the elementary excitation.

Note that the single-rod elementary structure does not at all correspond with the mean dispersion in this case: in Figure 4.8 the blue curves are not aligned with the dashed black curves. This is intuitively acceptable again, for the large nanorod structure the four nearby corners communicate strongly, which thus mainly happens through the thin dielectric.

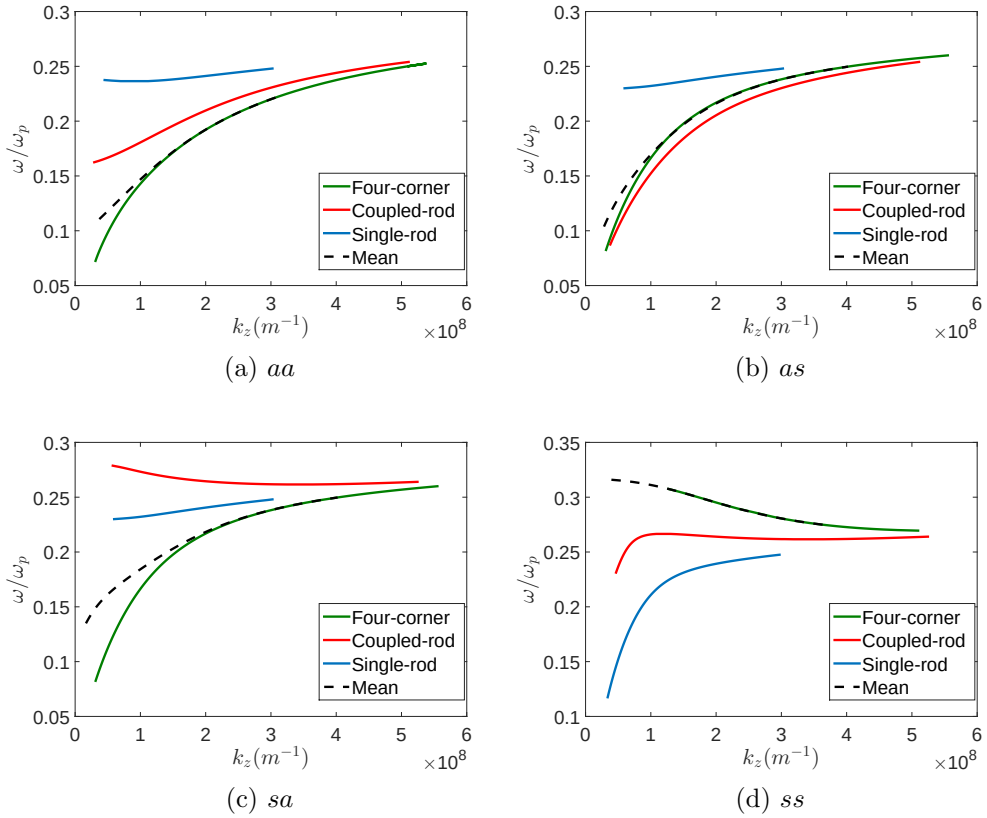

(a) *aa* (b) *as*

(c) *sa* (d) *ss*

Figure 4.8: Comparison between the mean calculated with equation 4.2 and the three possible elementary excitations for the large nanorod array. For each graph, the green curve corresponds to the four-corner structure, red curve corresponds to the coupled-rod, blue curve corresponds to the single-rod and black dashed curve correspond to the calculated mean. (a) For *aa* mode. (b) For *as* mode. (c) For *sa* mode. (d) For *ss* mode.

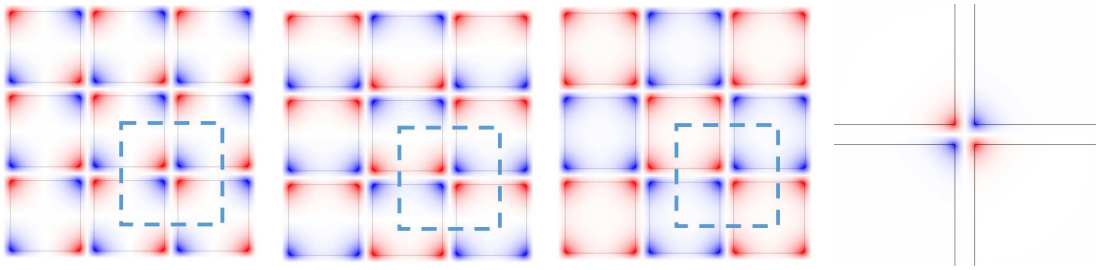

(a) Γ (b) X_1 (c) M (d) El. excitation

Figure 4.9: E_z field plots for the *aa* band (first row of Table 4.1) of the large nanorod array at three specific points for $k_z = 3 \times 10^8 m^{-1}$. (a) At the Γ point. (b) At the X_1 point. (c) At the M point. At the three specific points, the same pattern highlighted by the blue dashed square emerges. (d) Mode *aa* of the four-corner structure related to the large nanorod array, also for $k_z = 3 \times 10^8 m^{-1}$.

We remark that a coupling through dielectric is accompanied by a change of symmetry in one given direction when the Bloch wavector is equal to $\frac{\pi}{P}$ in this direction. For example for the first row in Table 4.1, we see that the symmetry in the x direction of the mode aa changes between the Γ and X_1 points (where $k_x = \frac{\pi}{P}$) and thus aa becomes sa. When the wavector in the y direction is equal to $\frac{\pi}{P}$, the symmetry in the y direction changes between the X_1 and M points and the mode sa becomes ss.

This change of symmetry does not happen when the coupling occurs via metal-dielectric interfaces (as for the small rod case of the previous Section).

4.4 Medium size nanorods

We study arrays of medium size square nanorods ($w = 16.3$ nm). This particular size was chosen by examining the dispersion at the Γ point for varying widths.

For small nanorods, the aa mode dispersion is always above the ss mode (Figure 4.10a, green above blue curve). In the case of large nanorods however, the ss mode is above the aa mode curve (Figure 4.10c, blue above green curve). At the particular width $w = 16.3$ nm, the aa and ss curves intersect each other and the modes are very close (Figure 4.10b).

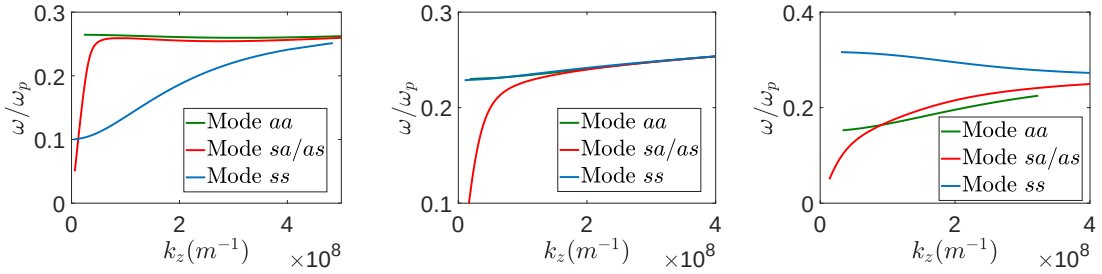

(a) $w = 8$ nm (b) $w = 16.3$ nm (c) $w = 25$ nm

Figure 4.10: Dispersion at the center of the Brillouin zone for nanorod arrays of width (a) $w = 8$ nm (b) $w = 16.3$ nm (c) $w = 25$ nm.

This width thus indicates a boundary between the two regimes analysed in the previous Sections, and a mix is expected between coupling via metal-dielectric interfaces (small nanorod case) and through dielectric (large nanorod case).

Again, using equation 4.2 we determine the mean for each mode. Here, the symmetry changes are not straightforward, because they depend on the frequency range. We delimit two frequency ranges by the intersection between the aa and the sa/as modes around $\omega = 0.246\ \omega_p$. Note that the ss and sa/as curves are very close but do not intersect. The symmetry changes for the two ranges are given in Table 4.2 (below $\omega = 0.246\omega_p$) and Table 4.1 (above $\omega = 0.246\omega_p$, same as the large nanorod case).

As we can see in the first two rows of Table 4.2, below $\omega = 0.246\ \omega_p$ the mode aa and as change symmetry only in one direction (y and x direction, respectively) and, as seen before for large nanorod arrays, this is a sign of coupling through dielectric

$\Gamma(0,0)$	$X_1(\frac{\pi}{P},0)$	$M(\frac{\pi}{P},\frac{\pi}{P})$
aa	aa	as
as	ss	ss
sa	sa	sa
ss	as	aa

Table 4.2: Symmetry changes for medium sized arrays below $\omega = 0.246\ \omega_p$ in function of the Bloch wavevector for a given k_z. Each row corresponds to a particular mode.

in the y direction for the aa mode and in the x direction for the as mode (and thus coupling via metal-dielectric interface in the x direction for aa mode and in the y direction for as mode). The elementary excitation is thus likely to be the coupled-rod structure, and this statement is confirmed by Figure 4.11a and Figure 4.11b.

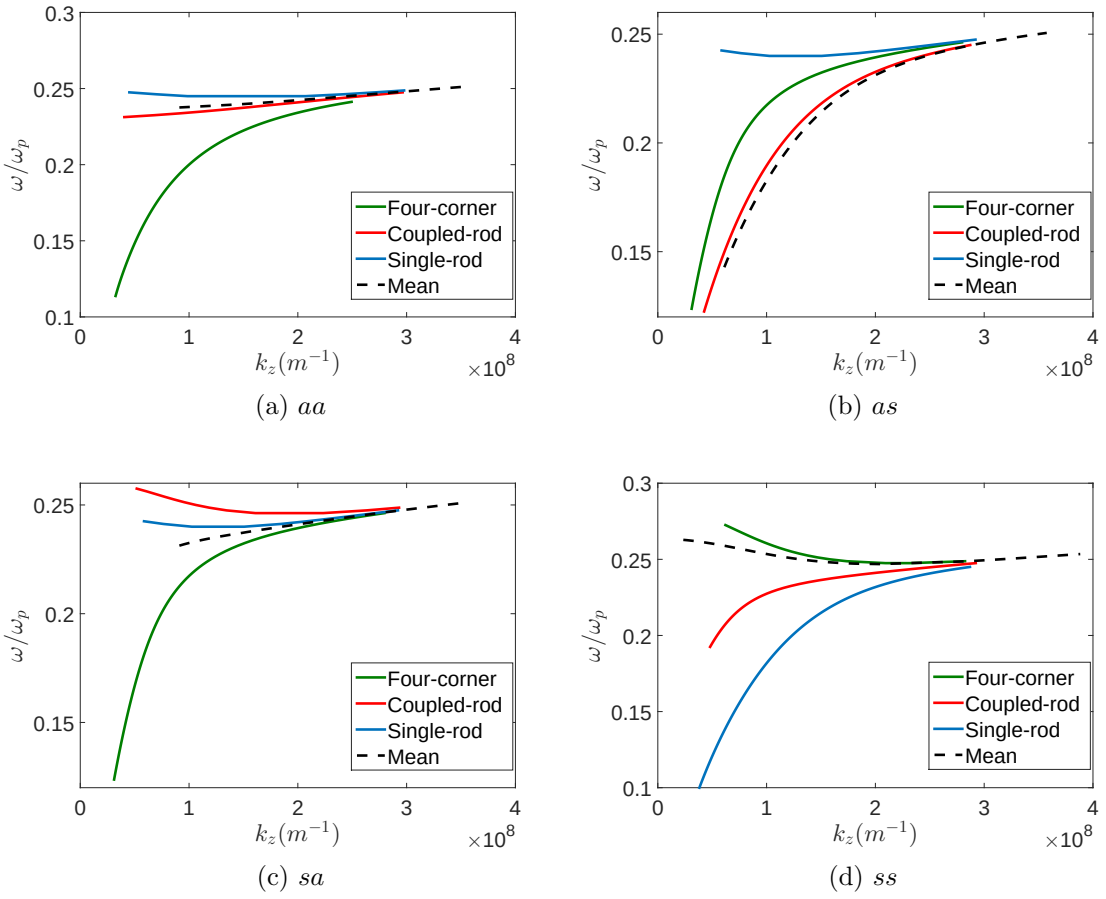

(a) aa (b) as

(c) sa (d) ss

Figure 4.11: Comparison between the mean calculated with equation 4.2 and the three possible elementary excitations for the medium size nanorod array. For each graph, the green curve corresponds to the four-corner structure, red curve to coupled-rod, blue curve to single-rod and black dashed curve to the calculated mean. (a) aa mode. (b) as mode. (c) sa mode. (d) ss mode.

In the third row of Table 4.2, we notice that the mode *sa* does not change symmetry in any direction, a coupling via metal-dielectric interface occurs and the elementary excitation is the single-rod. This statement is also confirmed with Figure 4.11c.

Finally, in the last row of Table 4.2, the symmetry of the *ss* mode changes in the two directions, a coupling through dielectric occurs and the elementary excitation is the four-corner structure, which is confirmed in Figure 4.11d.

Above $\omega = 0.246\ \omega_p$ the dispersion is difficult to analyze from Figure 4.11, as the confinement is so strong that all elementary modes converge to the single corner dispersion, so one cannot discriminate between them. However, the symmetry changes (Table 4.1) lead us to state that the elementary excitation is the four-corner structure for all modes, because the changes of symmetry are the same as for large nanorod arrays.

At medium size, the resulting elementary excitations thus depend on the symmetry and frequency range, which is intuitive because the coupling strengths via interfaces and dielectrics are similar. This is also indicated because the calculated average is not as perfectly superposed with the elementary modes, in contrast with small and large widths.

4.5 Rectangular nanorods

Now, we break the symmetry between the x and y directions by studying rectangular nanorods instead of square ones, see Figure 4.2d. The width in the x direction is much larger than the width in the y direction. A change of symmetry of the modes between the specific points is also present in this situation and is summarized in Table 4.3.

$\Gamma(0,0)$	$\mathrm{X}_1(\frac{\pi}{P},0)$	$\mathrm{X}_2(0,\frac{\pi}{P})$	$\mathrm{M}(\frac{\pi}{P},\frac{\pi}{P})$
aa	sa	aa	sa
as	ss	as	ss
sa	aa	sa	aa
ss	as	ss	as

Table 4.3: Symmetry changes for rectangular nanorod arrays in function of the Bloch wavevector for a given k_z. Each row corresponds to a particular mode.

We note that the symmetry in the x direction changes (as in the case of large square nanorods), but not in the y direction (similar to small square arrays). The coupling between corners is thus through the dielectric in the x direction, and via metal-dielectric interface in the y direction. The leading elementary excitation is therefore the coupled-rod structure, which is confirmed by Figure 4.12.

This is again intuitively acceptable because the corners are strongly connected through dielectric in the x direction, and through the metal-dielectric interfaces in the y direction.

This can also be confirmed via the field profiles at the four BZ points, see Figure 4.13a-d for the *as* band (second row of Table 4.3). The same pattern emerges,

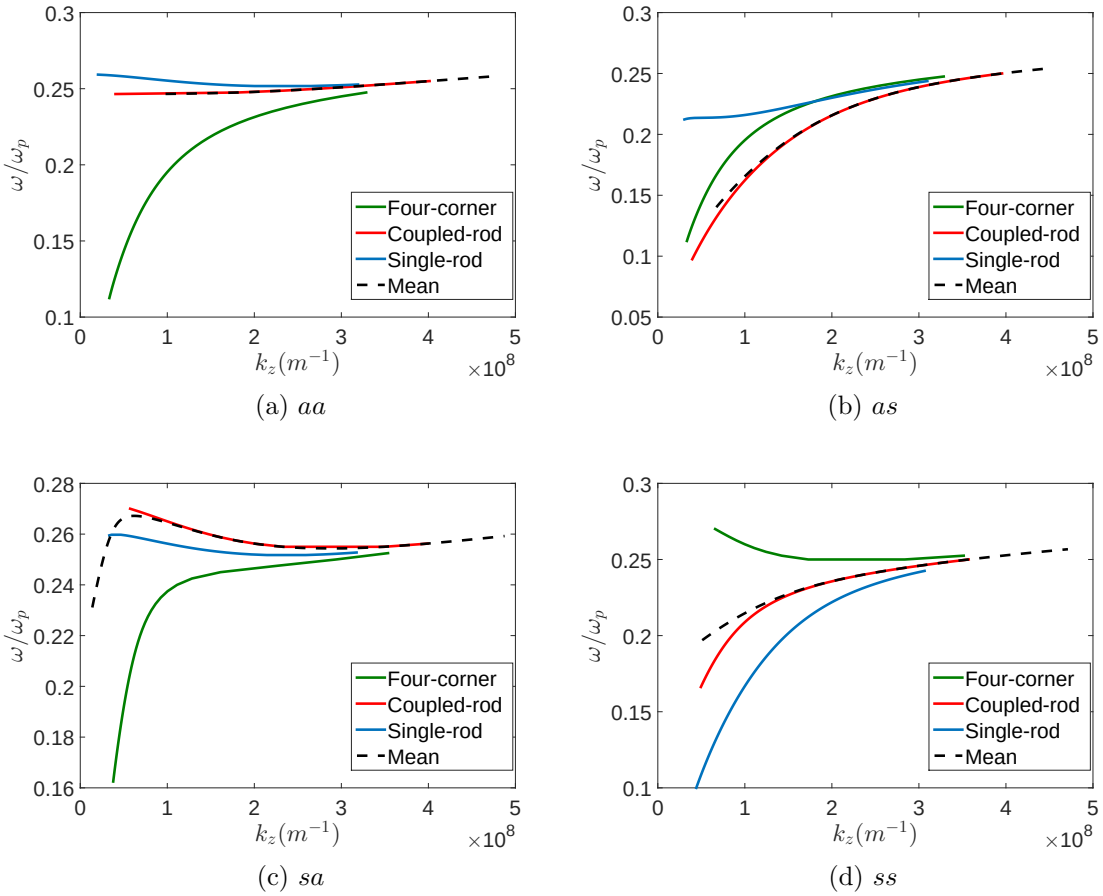

Figure 4.12: Comparison between the mean calculated with equation 4.3 and the three possible elementary excitations for the rectangular nanorod array. For each graph, the green curve corresponds to the four-corner structure, red curve to coupled-rod, blue curve to single-rod and black dashed curve to the calculated mean. (a) aa mode. (b) as mode. (c) sa mode. (d) ss mode.

which corresponds with the as mode of the coupled-rod structure (Figure 4.13e), thus forming the elementary excitation.

One should remark that the coupled-rod structure is the basic geometry in this case, because one dimension of the nanorods (w_x) is much larger than the other one (w_y), with respect to the period. If w_x and w_y were much smaller than the period, the elementary structure would be the single-rod. If both widths were close to the period, the elementary structure would be the four-corner structure.

4.6 Summary

In this chapter we have demonstrated that the dispersion of an array of square or rectangular metallic nanorods in a dielectric host can be connected directly to the modes of simpler geometries, in analogy with the gap and slab plasmon for the multilayer HMM presented in Section 2.4.2. This leading 'elementary excitation'

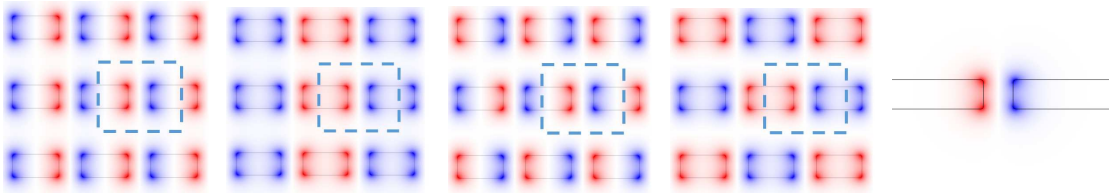

(a) Γ (b) X_1 (c) X_2 (d) M (e) El. excitation

Figure 4.13: E_z field plots for the *as* band (second row of Table 4.3) for the rectangular nanorod array at the four specific BZ points for $k_z = 3 \times 10^8 m^{-1}$. (a) At the Γ point. (b) At the X_1 point. (c) At the X_2 point. (d) At the M point. At the four points the same pattern highlighted by the blue dashed square emerges. (e) Mode *as* of the coupled-rod structure related to the rectangular nanorod array, also for $k_z = 3 \times 10^8 m^{-1}$.

depends strongly on the size and shape of the nanorods, and can be determined via the proposed analysis method, which compares the elementary dispersion with a judiciously averaged array dispersion.

The analysis also provides information on the symmetries of the modes at the particular BZ points. In fact, a strong coupling of the corners through dielectric in a given direction is accompanied by a change of symmetry when the Bloch wavevector in this direction is equal to $\frac{\pi}{P}$. This behaviour is not observed for coupling via a metal-dielectric interface.

We demonstrated that the dispersion of small square nanorod arrays originates from single-rod excitations, and that large square nanorod arrays are associated with four-corner structures. Indeed, for small squares the corners are coupled via the metallic sides, whereas for large squares the corners couple through the dielectric.

In the intermediate size regime, the array modes result from various elementary modes, depending on the frequency and mode symmetry. This complication is due to the balanced strength of coupling via the metal sides or through the dielectric.

Finally, rectangular nanorod arrays (with one relatively large dimension) can be described by the coupled-rod structure. The corners are thus connected via the metal rod sides in the narrow direction, and through dielectric in the wide direction.

In short, via the introduced analysis method one gains understanding of the dispersion in arrays of metallic nanorods, which opens the way to comprehend other types of metamaterials via their elementary excitations.

Most of the work of this chapter was presented in [83].

5

Fano resonances in tilted HMM cavities

Various designs of cavities based on HMMs have already been studied, and they present interesting features such as an anomalous scaling law [76], whispering-gallery modes [84], zeroth order Fabry-Perot resonances [85] and Fano resonances [86].

In this chapter we demonstrate a new type of cavity using hyperbolic properties, that presents very sharp Fano resonances for both classic and graphene multilayers. As we have described in Section 3.1.2, Fano resonances are asymmetrically shaped resonant phenomena that arise from the interference between a slowly varying background and a narrow resonant process [56, 87, 88]. Because their features stem from the interplay between two distinct channels, the resonances are very sensitive to any changes, rendering them interesting, among others, for sensing applications [55].

Using rigorous numerical simulations and a thorough modal analysis, we elucidate the mechanism as the simultaneous excitation of a propagating and an evanescent mode in the cavity. The propagating mode being responsible for the narrow Fabry-Perot resonances, whereas the evanescent modes leads to the slowly varying background.

This study is also a clear example to demonstrate that the effective medium model described in Section 2.3 breaks down when the effective indices start to be large [43].

Moreover, because the effective index is very high in the slanted cavity, we can create deep subwavelength cavities of a few nanometers in the visible regime

with metal-dielectric structures and a few micrometers in the terahertz regime with graphene-based multilayers. Even if the main part of this chapter treats lossless metamaterials, we show that this mechanism remains valid even in the presence of losses. In addition, the graphene-based multilayers have the advantage to offer tunability and control on position and sharpness of the Fano resonances, through variation of the doping.

In Section 5.1 we present the proposed cavity designs. Section 5.2 inspects the light behaviour using effective medium theory, leading to an incomplete description. In Section 5.3 we calculate the correct characteristics, and explain the observed behaviour for metal-dielectric multilayer, and subsequently for graphene multilayers in Section 5.4. Finally, in Section 5.5 we discuss the impact of loss in the metal-dielectric multilayer, and we conclude in Section 5.6.

5.1 Design

We study the transmission and reflection of light along the parallel direction (so $k_\perp = k_y = 0$) of a HMM with a finite section of tilted layers in the middle (Figure 5.1). The central tilt section is described by A (the vertical offset), B (the horizontal offset) and L (the parallel length) with $L = \sqrt{A^2 + B^2} = \frac{A}{\sin\theta}$, and θ is the tilt angle.

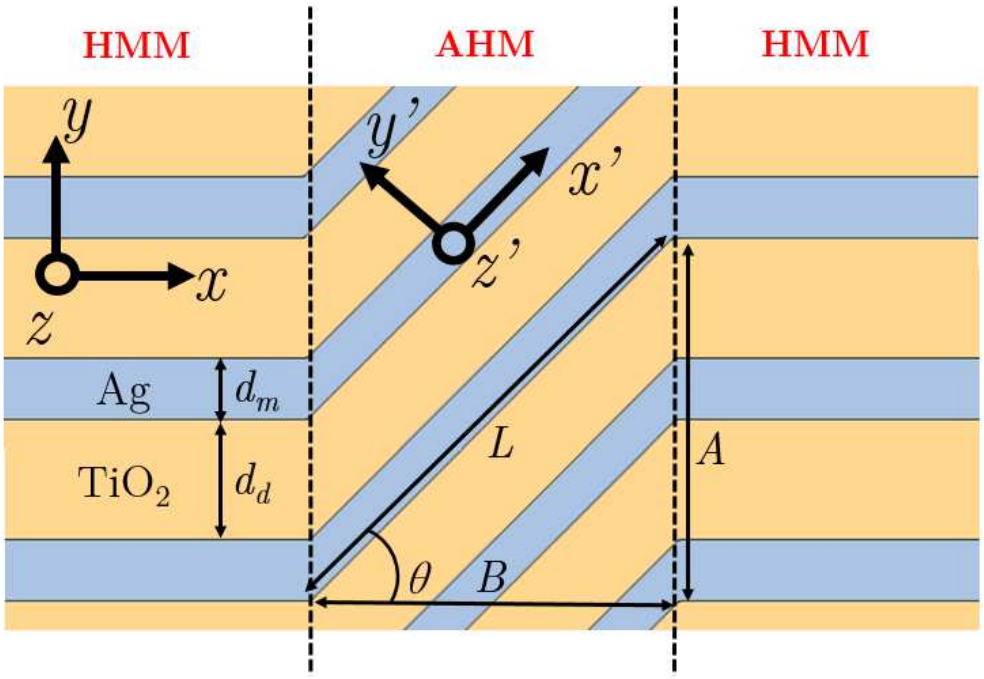

Figure 5.1: A multilayer HMM with a tilted section in the middle. The fundamental mode is excited from the left. The structure is divided in three parts along the x direction: Two identical HMMs on the left and right and an asymmetrical HMM (or AHM) in the center.

Because we work in the visible and near-infrared region, we use silver (Ag) as metal and TiO_2 as dielectric, which are well-known to provide good performances

at these frequencies [13, 89, 90]. We choose $d_m = 10$ nm for the Ag thickness and $d_d = 20$ nm for the TiO_2 thickness. For the same reasons as for Chapter 4, we use a dispersionless index for TiO_2 with $n_{TiO_2} = 2.7$ and a Drude model for Ag (using Equation 2.8):

$$\varepsilon_{\text{Ag}} = 1 - \frac{\omega_p^2}{\omega^2 + i\omega\gamma} \tag{5.1}$$

with $\omega_p = 1.26 \times 10^{16}$ rad/s the plasma frequency and γ the collision frequency that we fix equal to zero; we examine the influence of losses in Sec. 5.5.

We work in the regime where only one propagating Bloch mode exists in the HMM, hence the wavelength is larger than 600 nm in our case. We excite the structure from Figure 5.1 with this propagating mode from the left and look at its reflectance and transmittance for a Bloch momentum $k_y = 0$.

In the next section we study this structure using an effective medium theory, which will show its limits to describe such systems.

5.2 Effective medium theory

For a uniaxial multilayer using effective medium theory, Equation 2.28 describes the dispersion relation for TM waves (transverse magnetic, magnetic field along z direction), that is [46, 91]:

$$\frac{k_\parallel^2}{\varepsilon_\perp} + \frac{k_\perp^2}{\varepsilon_\parallel} = k_0^2 \tag{5.2}$$

where $k_\parallel$ ($k_\perp$) is the wavevector in the direction parallel (perpendicular) to the layers and k_0 the wavevector in free-space. The permittivity in the parallel and normal directions depends only on the permittivity of the constitutive materials and their filling fraction, as we have seen from Equations 2.16 and 2.19, that we recall here for convenience:

$$\varepsilon_\parallel = f\varepsilon_m + (1-f)\varepsilon_d, \tag{5.3}$$

$$\varepsilon_\perp = \frac{\varepsilon_m \varepsilon_d}{f\varepsilon_d + (1-f)\varepsilon_m} \tag{5.4}$$

where $\varepsilon_\parallel$ and $\varepsilon_\perp$ are the components of the permittivity in the parallel and perpendicular directions, ε_m and ε_d are the permittivity of the metal and the dielectric, respectively, and f is the metal filling fraction.

For the used wavelength regime, these materials turn out to be hyperbolic, and Equation 5.2 is thus the equation of a hyperbola. Consequently, the HMM can support propagating modes with extremely large wavevectors. We note, however, that this equation also has other solutions. There is an evanescent mode (imaginary parallel momentum and real perpendicular momentum), and a mode with real parallel momentum and imaginary perpendicular momentum. These modes are often overlooked, because they are accessible only in certain conditions. We show later on that we fulfill the conditions to excite the evanescent mode, and it will play an important role for the cavity mechanism in the next section.

The geometry explained in the previous section can be divided in three different parts (Figure 5.1). The left and right parts are 'standard' HMMs and are governed by Equation 5.2 with $\varepsilon_\perp = \varepsilon_y$, $\varepsilon_\parallel = \varepsilon_x$ and $k_\parallel = k_x$, $k_\perp = k_y$.

The central part however is a hyperbolic medium with the optical axis tilted with respect to the x direction. In the literature these HMMs with tilted optical axis are sometimes referred to as asymmetric hyperbolic metamaterials (AHMs) [92, 93].

The AHM part of Figure 5.1 is also governed by Equation 5.2, but with $\varepsilon_\perp = \varepsilon_{y'}$, $\varepsilon_\parallel = \varepsilon_{x'}$ and $k_\parallel = k'_x$, $k_\perp = k'_y$. Even if the thicknesses of the Ag and TiO_2 layers in the central part change ($d'_m = d_m \cos\theta$ and $d'_d = d_d \cos\theta$), we still have the same $\varepsilon_x = \varepsilon_{x'}$ and $\varepsilon_y = \varepsilon_{y'}$, because Equations 5.3 and 5.4 only depend on the filling fraction f, which remains the same.

Using a coordinate transformation, Equation 5.2 in the AHM becomes, in the main coordinates:

$$k_x^{(1,2)} = \frac{k_y \varepsilon_{xy} \pm \sqrt{(\varepsilon_{xy}^2 - \varepsilon_{xx}\varepsilon_{yy})(k_y^2 - k_0^2 \varepsilon_{xx})}}{\varepsilon_{xx}} \tag{5.5}$$

with the the solution $k_x^{(1)}$ corresponds to the sign "+" in the formula for mode propagating towards smaller x and $k_x^{(2)}$ to the sign "-" for waves propagating towards larger x. Note that in our case of normal incidence, $k_x^{(1)}$ and $k_x^{(2)}$ are equal in magnitude. ε_{xx}, ε_{xy} and ε_{yy} are the permittivity components of the AHM in the main coordinates, which are obtained by applying a rotation matrix to the diagonal permittivity tensor in the tilted coordinates:

$$\overline{\overline{\varepsilon}} = \mathcal{R}(\theta)\, \overline{\overline{\varepsilon'}}\, \mathcal{R}(\theta)^T = \begin{pmatrix} \varepsilon_{xx} & \varepsilon_{xy} \\ \varepsilon_{xy} & \varepsilon_{yy} \end{pmatrix} \tag{5.6}$$

with $\mathcal{R}(\theta)$ the matrix of rotation around the z axis and $\overline{\overline{\varepsilon'}} = \begin{pmatrix} \varepsilon'_x & 0 \\ 0 & \varepsilon'_y \end{pmatrix}$ the permittivity tensor in the tilted coordinates. This leads to

$$\varepsilon_{xx} = \varepsilon_{x'} \cos^2\theta + \varepsilon_{y'} \sin^2\theta \tag{5.7}$$

$$\varepsilon_{xy} = (\varepsilon_{x'} - \varepsilon_{y'}) \cos\theta \sin\theta \tag{5.8}$$

$$\varepsilon_{yy} = \varepsilon_{x'} \sin^2\theta + \varepsilon_{y'} \cos^2\theta \tag{5.9}$$

For zero momentum in the y direction (i.e. $k_y = 0$), we can easily calculate the momentum in the x direction in the HMMs and in the AHM. We find for the HMMs, $k_{x,HMM} = \sqrt{\varepsilon_y}\, k_0$, and for the AHM, $k_{x,AHM} = \sqrt{(\varepsilon_{xy}^2 - \varepsilon_{xx}\varepsilon_{yy})(-k_0^2\varepsilon_{xx})}/\varepsilon_{xx}$. The difference in the momentum leads to reflection at the interfaces and the introduced design functions thus as a cavity structure of width B.

Now that we have defined the effective permittivity components in the HMM and AHM parts, we can easily calculate numerically the scattering characteristics of the structure with the different parts replaced by homogeneous blocks with these effective parameters. The reflectance of light as a function of the tilt angle θ and the length L at a wavelength $\lambda_0 = 700$ nm is shown in Figure 5.2.

We observe two distinct behaviours above and below a transition tilt angle of about $\theta_t \approx 21°$. This phenomenon can be understood by looking at the isofrequency contours of the HMM and AHM sections, respectively (Figure 5.3).

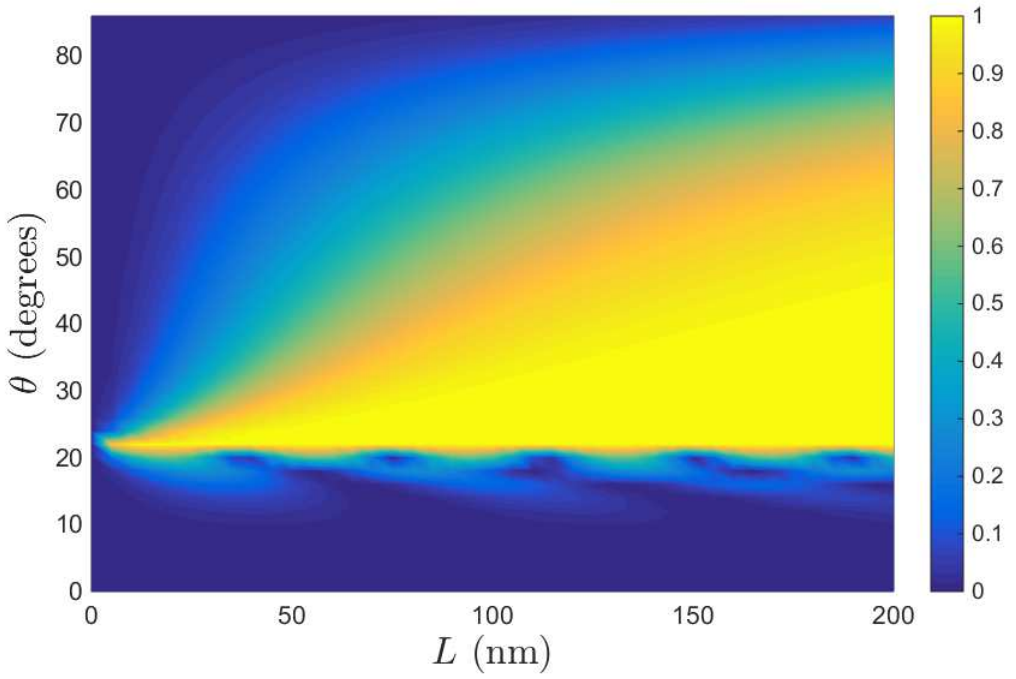

Figure 5.2: Reflectance versus tilt length L and angle θ using effective medium theory.

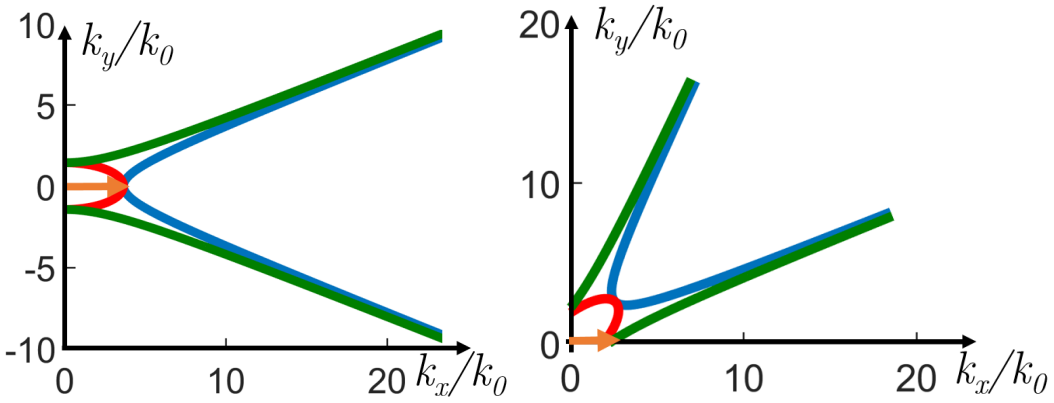

(a) HMM (b) AHM

Figure 5.3: Isofrequency contours (a) in the HMM, and (b) in the AHM for a tilt angle of 45° with EMT, for $\lambda_0 = 700$ nm. Blue curve corresponds to propagating waves, green curve corresponds to evanescent waves and red curve corresponds to propagating wave in the x direction and evanescent in the y direction. The orange arrow in (a) indicates the input wavevector, in (b) the dominant (green) mode in the AHM.

Blue curves correspond to the isofrequency contour of propagating modes, thus with real components for the x and y momenta (therefore, real part of momenta is plotted). Green curves correspond to evanescent modes with imaginary momentum components in both directions (therefore, imaginary part of momenta is plotted). Red curves correspond to modes with real x-momentum and imaginary y-

momentum (therefore, the real part of the momentum is plotted on the abscissa and the imaginary part is plotted on the ordinate). Note that the isofrequency contours of Figure 5.3b are just the isofrequency contours of Figure 5.3a rotated by 45°.

The conservation of the momentum in the transverse direction ($k_y = 0$) imposes in the tilted coordinates (x', y'):

$$k_y = k'_x \sin\theta + k'_y \cos\theta = 0 \tag{5.10}$$

so

$$k'_x \sin\theta = -k'_y \cos\theta \tag{5.11}$$

and thus, the mode evanescent in the y' direction and propagating in the x' direction (red curves in Figure 5.3) inside the AHM cannot be excited because Equation 5.11 cannot be fulfilled. The mode evanescent in all directions (green curves in Figure 5.3) and the propagating one (blue curves in Figure 5.3) however can fulfill Equation 5.11, and can be excited for normal incidence (k_y=0).

The orange arrow in Figure 5.3a shows the incident momentum inside the HMM. From Figure 5.3b we see that transverse momentum conservation (the orange arrow in Figure 5.3b needs to be horizontal) requires that only one mode at a time is excited inside the AHM. The latter mode is either propagating (blue) or evanescent (green), in function of the tilt angle.

The transition angle θ_t between the two regimes is determined by the asymptote of the hyperbolic contours (the same asymptote for both blue or green contours), this angle equals

$$\theta_t = \operatorname{atan}\left(\sqrt{\frac{\varepsilon_x}{\varepsilon_y}}\right) \approx 21.6° \tag{5.12}$$

at $\lambda_0 = 700$ nm.

Thus, below θ_t only a propagating mode (orange arrow touches blue curve) is excited inside the AHM, so the lobes in the lower part of Figure 5.2 are Fabry-Perot resonances of the cavity. The fairly weak reflectance of the lobes is typical of Fabry-Perot cavities with low reflection at each interface, which is the case for small tilt angles.

Above θ_t only the evanescent mode (orange arrow touches green curve) is excited in the AHM, leading to the absence of Fabry-Perot fringes. Furthermore, the reflectance increases monotonously with B ($= L\cos\theta$), because the mode amplitude decreases exponentially with the length of propagation.

In the next section, we show that this EMT description is actually incomplete, and only provides for qualitative trends compared to the exact simulations.

5.3 Rigorous calculations and analysis

We employ the commercial finite-element software COMSOL Multiphysics 5.2 [72] (described in Section 3.2.2) to calculate the exact propagation through the structure (Figure 5.1), with slightly rounded corners to avoid hotspots. The reflectance in function of the tilt angle θ and the parallel propagation length L is shown in Figure 5.4. The same lobe-like behaviour as with EMT below θ_t is present, but the behaviour above θ_t is completely different.

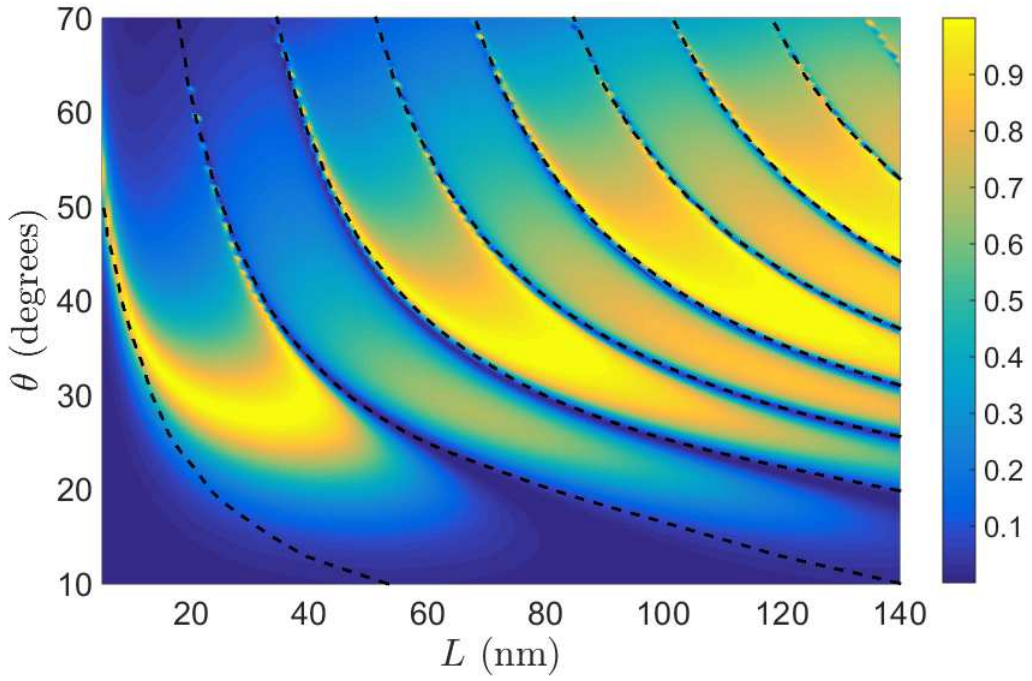

Figure 5.4: Exact reflectance in function of θ and L. Black dashed line corresponds to the eight first orders of the Fabry-Perot constructive interferences. The wavelength is 700 nm.

In order to understand this difference, we need to take into account the exact dispersion relation, derived in Section 2.4.1 (Equation 2.31) by solving Maxwell's equations and applying Bloch's theorem [50, 51]

$$\begin{aligned}\cos\left(k_y D\right) = \; & \frac{\left(\kappa_d \varepsilon_m + \kappa_m \varepsilon_d\right)^2}{4\kappa_d \kappa_m \varepsilon_d \varepsilon_m} \cosh\left(\kappa_d d_d + \kappa_m d_m\right) \\ & - \frac{\left(\kappa_d \varepsilon_m - \kappa_m \varepsilon_d\right)^2}{4\kappa_d \kappa_m \varepsilon_d \varepsilon_m} \cosh\left(\kappa_d d_d - \kappa_m d_m\right)\end{aligned} \tag{5.13}$$

with $D = d_m + d_d$ the period of the multilayer, $\kappa_{d,m} = \sqrt{k_x^2 - k_0^2 \varepsilon_{d,m}}$ the decay coefficients in the dielectric and metallic layers, respectively. This dispersion relation is also valid in the AHM, by replacing (k_x, k_y) with (k'_x, k'_y), $d_{d,m}$ with $d'_{d,m} = d_{d,m} \cos\theta$ and D with $D' = D\cos\theta$. Combining Equation 5.13 with the transverse momentum conservation condition (Equation 5.11) in the AHM, we finally arrive at

$$\begin{aligned}\cos\left(k'_x D' \tan\theta\right) = \; & \frac{\left(\kappa'_d \varepsilon_m + \kappa'_m \varepsilon_d\right)^2}{4\kappa'_d \kappa'_m \varepsilon_d \varepsilon_m} \cosh\left(\kappa'_d d'_d + \kappa'_m d'_m\right) \\ & - \frac{\left(\kappa'_d \varepsilon_m - \kappa'_m \varepsilon_d\right)^2}{4\kappa'_d \kappa'_m \varepsilon_d \varepsilon_m} \cosh\left(\kappa'_d d'_d - \kappa'_m d'_m\right)\end{aligned} \tag{5.14}$$

The main conclusion is that two modes satisfy this equation *at the same time* for all tilt angles θ: an evanescent one and a propagating one. This result is consistent with the rigorously simulated isofrequency contours (Figure 5.5), where the blue curve represents the propagating mode and the green curve the evanescent mode.

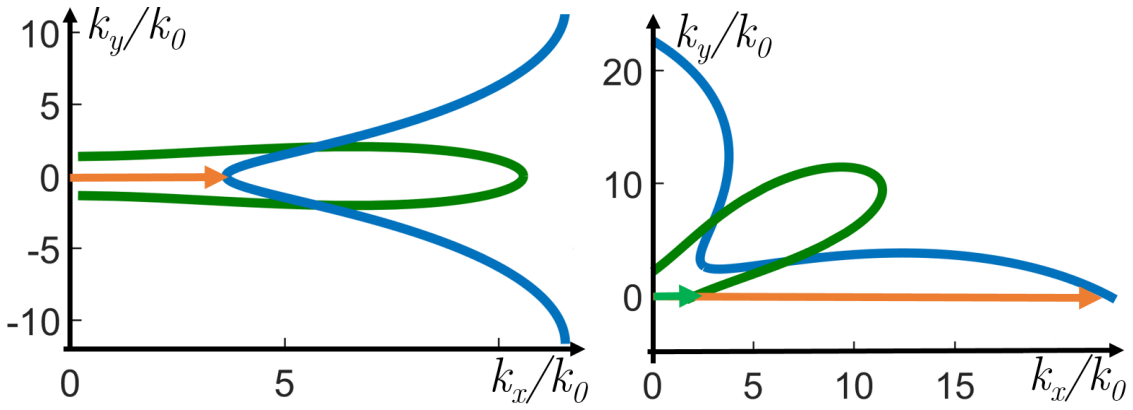

(a) HMM (b) AHM

Figure 5.5: Exact isofrequency contours (a) in the HMM and (b) in the AHM for a tilt angle of 45° in the first Brillouin zone for $\lambda_0 = 700$ nm. Blue curves correspond to propagating waves, green curves correspond to evanescent waves. Conservation of the transverse wavevector is illustrated by the orange and green arrows.

The orange arrow in Figure 5.5a shows the incident momentum inside the HMM. In Figure 5.5b, two horizontal arrows are needed to represent the momentum of the two excited modes inside the AHM. The orange arrow represents the momentum of the propagating mode and the green arrow represents the momentum of the evanescent mode.

The first important difference with the EMT contours of Figure 5.3 is that the evanescent wave contour (green contours) that was an open curve is now a closed curve for the exact calculations of Figure 5.5. Secondly, because the structure is periodic, all the information is encoded in the first Brillouin zone, thus the isofrequency contour of the propagating wave (blue curves) is also periodic and is not limited by asymptotes, in contrast with the EMT contours.

For these reasons, inside the AHM, an evanescent and a propagating mode are always excited together. The interferences between these two modes inside the AHM cavity are responsible for the Fano resonances appearing in Figure 5.4. Indeed, Fano resonances can be described as arising from the interference between a slowly varying background (here: the evanescent wave) and a resonant process (here: the Fabry-Perot oscillations of the propagating mode).

The Fano nature is more visible in Figure 5.6 (blue curve), which shows the reflectance for an angle $\theta = 45°$ as a function of the width B of the cavity. Figure 5.6 further illustrates the cavity principle in detail: the Fabry-Perot oscillations of the propagating mode (red dashed curve) and the slowly increasing evanescent background (green curve) are shown separately. Both reflectance curves are obtained using a transfer matrix method under the hypothesis of an isotropic medium (a good approximation for normal incidence) as (from Equation 3.10):

$$R = |r|^2 = \left| r_{HA} + \frac{t_{HA} t_{AH} r_{AH} e^{i(2k_x B + \varphi)}}{1 - r_{AH}^2 e^{i(2k_x B + \varphi)}} \right|^2 \tag{5.15}$$

with r_{HA} and r_{AH} the Fresnel coefficients of reflection of the propagating (resp.

evanescent) mode for the HMM-AHM and AHM-HMM interfaces, t_{HA} and t_{AH} the Fresncel coefficient of transmission, k_x the wavevector in the x direction of the propagating (resp. evanescent) mode and φ a fitted phase term.

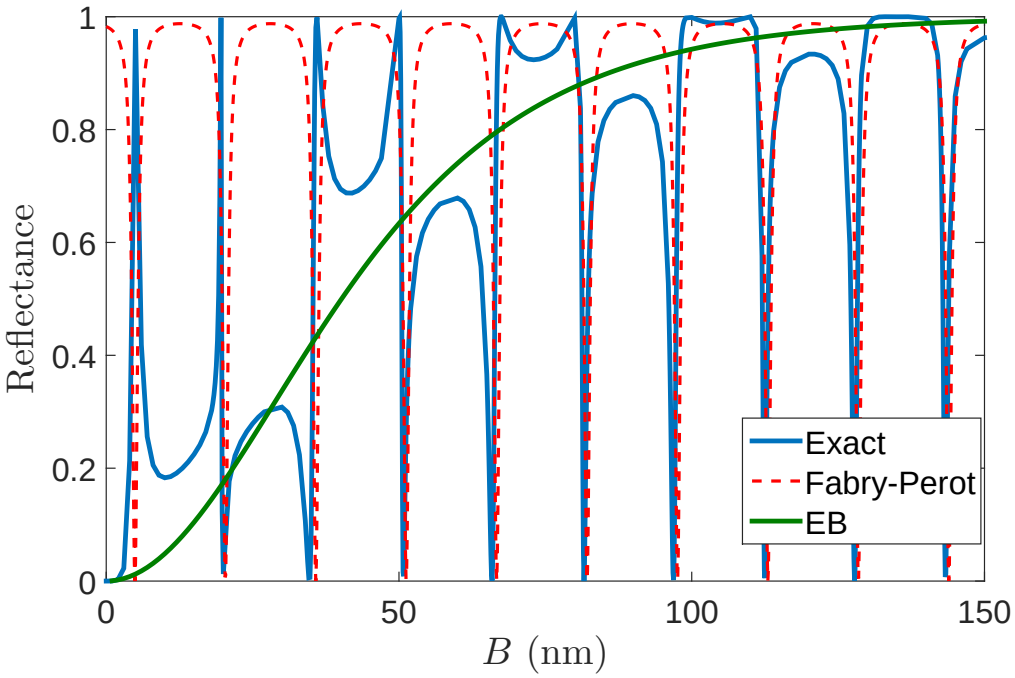

Figure 5.6: Comparison between the exact calculation of the reflectance (blue solid curve) and the slowly varying background of the evanescent mode (green solid curve) and the Fabry-Perot oscillations of the propagating mode (red dashed curve) for $\theta = 45°$ at $\lambda_0 = 700$ nm.

The exact reflectance thus arises from the interference of these two phenomena (leading to the blue curve). When the cavity length B becomes larger, the effect of the evanescent mode disappears, as its resulting reflectance (green curve) tends to 1, as the mode decays and does not manage to transmit. Then the characteristic only consists of typical Fabry-Perot oscillations from the propagating mode. For smaller lengths we obtain the typical asymmetric double-peak (maximum-minimum or vice-versa) Fano characteristics.

Black dashed lines in Figure 5.4 show the good correspondance between the Fano resonances and the Fabry-Perot peaks of the propagating mode; the latter are plotted using Equation 3.11, the typical phase-matching round-trip relation we have derived in Section 3.1.1:

$$2k_x(\theta)B + 2\varphi_r(\theta) = 2\pi m \tag{5.16}$$

with m an integer indicating the order, $\varphi_r(\theta)$ the phase change at each interface obtained by fitting, and $k_x(\theta)$ the wavevector in the x direction for $k_y = 0$ obtained from Equation 5.14 (and using $k_x = k'_x \cos\theta - k'_y \sin\theta$). The momentum in the x direction for the evanescent and propagating modes is shown in Figure 5.7.

The very high value of the mode index inside the cavity leads to the possibility to create very compact cavities, on the order of 5 nm width for $\theta = 45°$ (first peak

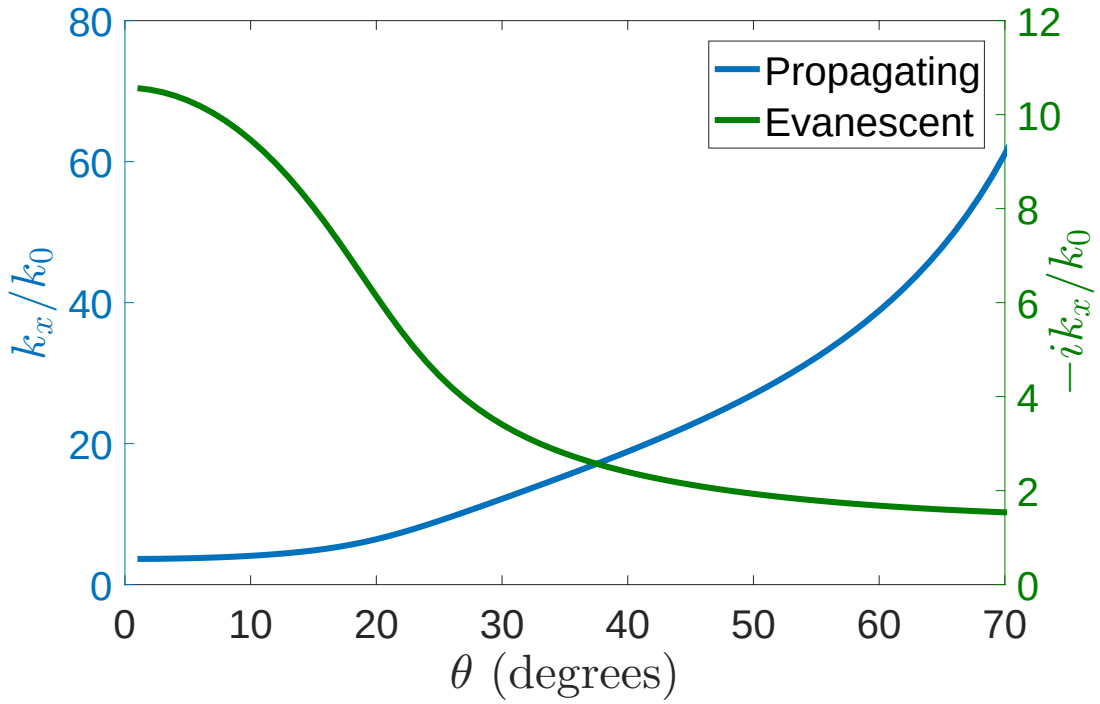

Figure 5.7: Momentum in the x direction k_x inside the AHM in function of the tilt angle for $k_y = 0$. Blue curve and axis represent the propagating mode, green curve and axis represent the evanescent mode.

in Figure 5.6). For the first order ($m = 1$) the reflectance shows a single peak, so no asymmetric double-peak characteristic, which is similar to other contexts, such as a cavity placed on the side of a waveguide [94]. The latter effect is intuitively acceptable as the evanescent mode background (the 'direct' channel) has a very large transmission for very thin cavities.

The shapes of the resonances are also present in the spectra of the structure. We show these spectra in two cases for $\theta = 45°$, with a reflectance peak for $A = 5$ nm, $B = 5$ nm (first order resonance, Figure 5.8a), and with asymmetric Fano shapes for $A = 35$ nm, $B = 35$ nm (third order resonance for $\lambda_0 = 700$ nm, second order for $\lambda_0 = 885$ nm , Figure 5.8b).

The insets of Figure 5.8 present the magnitude of the electric field at the first order resonance (inset of Figure 5.8a) and third order resonance (inset of Figure 5.8b) for the wavelength $\lambda_0 = 700$ nm. As we can expect, the first order resonance does not present a node in the cavity and the third order profile indicates two nodes. The field inside the cavity for the first order resonance is quite large, so one needs to pay attention to losses, this is discussed in the next section.

The reflectance for two specific tilt angles is presented in Figure 5.9, showing that cavity engineering is possible in the regime where hyperbolic modes are supported. For an angle $\theta = 30°$ and $\lambda_0 = 700$ nm (Figure 5.9a), the green curve of the isofrequency contour of Figure 5.5b indicates that the imaginary part of the momentum of the evanescent mode is fairly high, which is true for small θ (see also Figure 5.7). This explains why the asymmetric Fano resonances disappear rapidly,

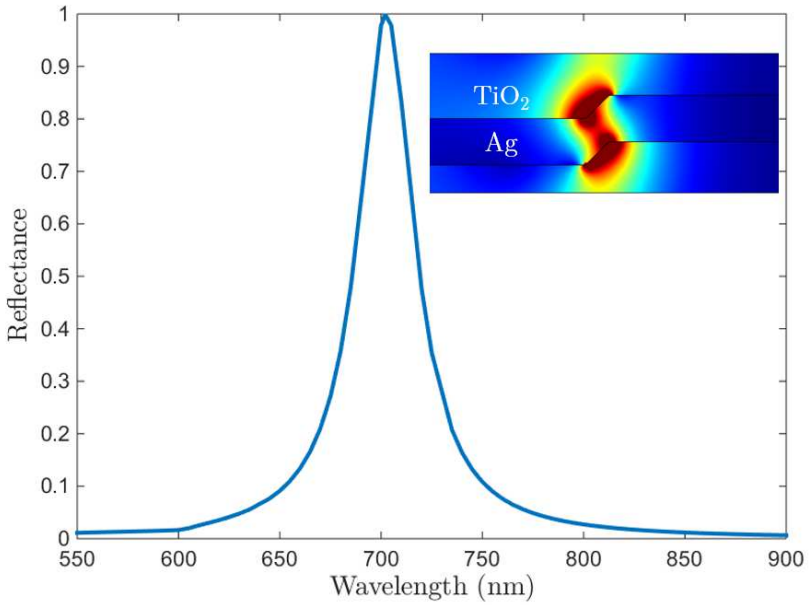

(a) $A = 5$ nm, $B = 5$ nm

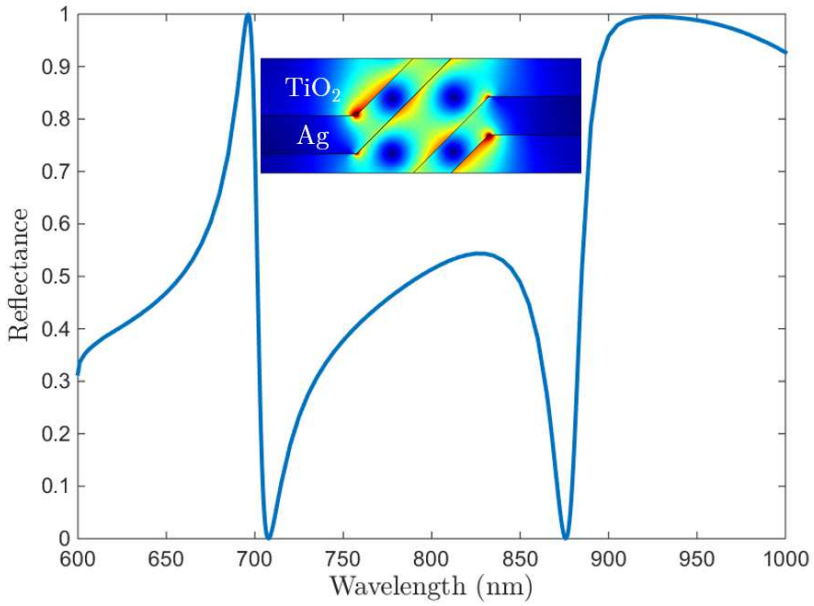

(b) $A = 35$ nm, $B = 35$ nm

Figure 5.8: Reflectance spectra with geometric parameters (a) $A = 5$ nm, $B = 5$ nm and (b) $A = 35$ nm, $B = 35$ nm. Insets show the magnitude of the electric field at the resonance wavelength $\lambda_0 = 700$ nm for a single unit cell of the periodic stacks.

and quickly lead to standard Fabry-Perot features.

For $\theta = 60°$ and $\lambda_0 = 700$ nm (Figure 5.9b) the imaginary part for the evanescent mode is low enough to allow for the existence of Fano resonances over a large range of cavity widths (see also Figure 5.7). Moreover, as the reflection of the propagating mode at each HMM-AHM interface is larger (because of the larger effective index, see

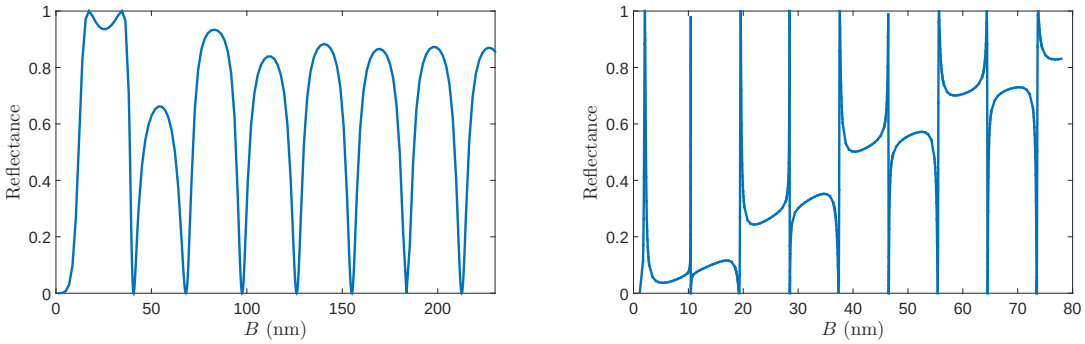

(a) $\theta = 30°$, $\lambda_0 = 700$ nm (b) $\theta = 60°$, $\lambda_0 = 700$ nm

Figure 5.9: Reflectance for specific configurations at $\lambda_0 = 700$ nm: (a) $\theta = 30°$. (b) $\theta = 60°$.

Figure 5.7), the peaks are narrower than for the smaller tilt angle (e.g. Figure 5.9a).

5.4 Graphene multilayers

In this section we describe the Fano resonances in a different system, namely graphene-based multilayers. This shows that the mechanism is more general, and can appear in various structures.

Graphene is a two-dimensional hexagonal lattice of carbon atoms whose interesting properties have been studied intensively over the last decade. This material supports surface waves in the near- to far-infrared, similar to the surface plasmons of metal-dielectric interfaces [29, 30, 95, 96]. Even if graphene is not a suitable platform for visible and near-infrared applications because of large losses, when combined with dielectrics, graphene-based multilayers offer a good opportunity for hyperbolic metamaterials in the terahertz regime [22, 97, 98]. Such graphene-based hyperbolic metamaterials offer interesting opportunities for a large variety of applications, such as negative refraction [99], total absorption [100] and enhancement of spontaneous emission of an emitter placed in the vicinity of the multilayer [21].

We search for similar phenomena as in the previous sections, by investigating the slanted multilayer as in Figure 5.10. For this structure we model the graphene layers as conductive sheets, with conductance obtained by the Kubo-Greenwood formula [101–104] from Equations 2.11 and 2.12 that we have described in Section 2.2.2

$$\sigma = \sigma_{intra} + \sigma_{inter} \tag{5.17}$$

with

$$\sigma_{intra} = \frac{2ie^2 k_B T}{\hbar^2 \pi(\omega + i\tau^{-1})} \ln\left[2\cosh\left(\frac{E_F}{2k_B T}\right)\right] \tag{5.18}$$

$$\sigma_{inter} = \frac{e^2}{4\hbar}\left[\frac{1}{2} + \frac{1}{\pi}\arctan\left(\frac{\hbar\omega - 2E_F}{2k_B T}\right)\right] - \frac{e^2}{4\hbar}\left[\frac{i}{2\pi}\ln\frac{(\hbar\omega + 2E_F)^2}{(\hbar\omega - 2E_F)^2 + (2k_B T)^2}\right] \tag{5.19}$$

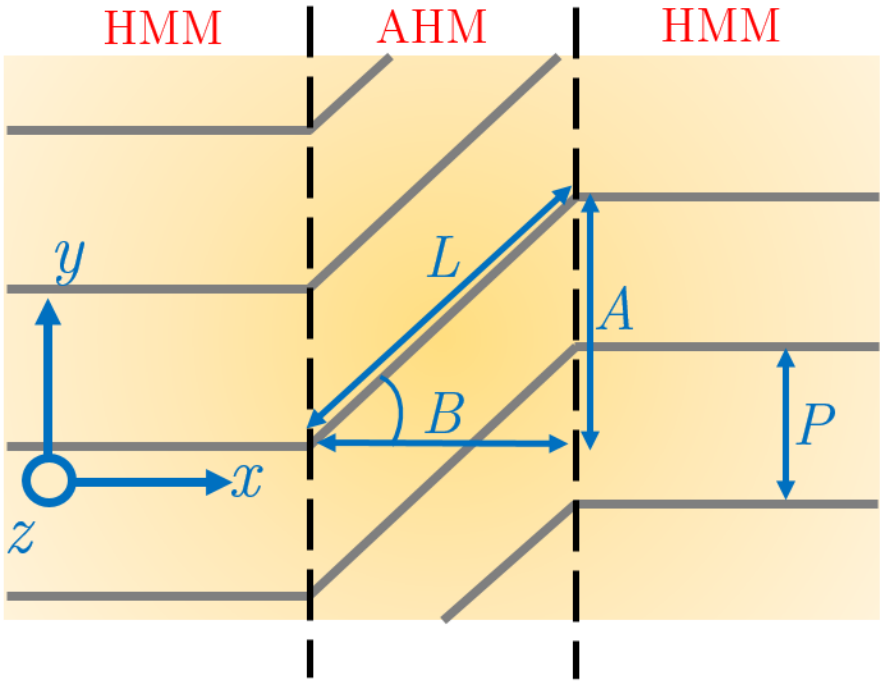

Figure 5.10: A graphene-based multilayer with a tilted section in the middle. The fundamental mode is excited from the left. The structure is divided in three parts along the x direction: Two identical HMMs on the left and right and an asymmetrical HMM (or AHM) in the center. Grey lines are the graphene sheets.

with σ_{intra} the conductivity related to the intraband electron-photon scattering processes, σ_{inter} related to the interband electron transitions, E_F the doping level, τ the electron scattering lifetime, T the temperature (we use room temperature, 300 K) and k_B the Boltzmann constant. We neglect spatial dispersion of graphene because the lattice constant is deeply subwavelength in the terahertz regime [105].

For simplicity, we model lossless graphene to compare with the previous section and so we take the imaginary part of the conductivity given by Equation 5.17. We use n_1=1.5 for the refractive index of the dielectric (permittivity $\varepsilon_1 = 2.25$) and a period $P = 1$ µm. The exact dispersion relation is obtained similarly to Equation 5.13 combining the transfer-matrix method (with surface currents) with Bloch's theorem, and one obtains [21, 88, 100]:

$$\cos(k_y P) = \cos(k_{y,1} P) - \frac{i}{2}\sigma Z_0 Z^{(p)} \sin(k_{y,1} P) \tag{5.20}$$

with Z_0 the impedance of free-space, $k_{y,1} = \sqrt{\varepsilon_1 k_0^2 - k_x^2}$ the wavevector in the dielectric, $Z^{(p)} = k_{y,1}/(k_0 \varepsilon_1)$ the impedance of the dielectric for TM-polarized waves.

With Equation 5.20 we can calculate the isofrequency contours both in the graphene-based HMM (Figure 5.11a) and the AHM (with a tilt angle $\theta = 60°$, Figure 5.11b). We can see the magnitude of the wavevectors are much larger than for the metal-dielectric case, reducing drastically the size of the cavity (compared to the wavelength).

In a similar way than in the previous sections, we have highlighted the incident

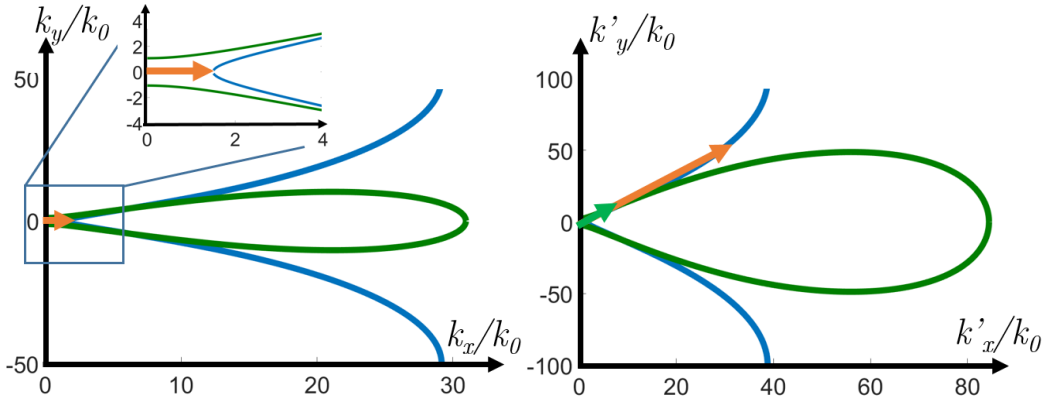

(a) HMM (b) AHM

Figure 5.11: Exact isofrequency contours (a) in the graphene-based HMM and (b) in the AHM for a tilt angle of 60° in the first Brillouin zone for $\lambda_0 = 100$ µm and a doping level $E_F = 0.1$ eV. Blue curves correspond to propagating waves, green curves correspond to evanescent waves. Conservation of the transverse wavevector is illustrated by the orange and green arrows. The inset in (a) shows a zoom on the small momentum part of the isofrequency contours of the HMM.

wavevector by the orange arrow in Figure 5.11a. Note that unlike Figure 5.5, we have rotated the wavevectors and not the axes here. The effective refractive index at normal incidence is approximatively the refractive index of the dielectric ($n = 1.5$), simplifying drastically the problem of light incoupling that can occur with a metal-dielectric multilayer. Similar to the previous metal-dielectric case, two modes are always excited in the AHM: an evanescent one and a propagating one (green and orange arrows in Figure 5.11b).

The resonances in this cavity are also Fano resonances, see the blue solid curve in Figure 5.12, which can again be explained as an interference between the smooth evanescent transmission (solid green curve in Figure 5.12) and the Fabry-Perot modes of the propagating mode (dashed red curve in Figure 5.12). Here, because of the large contrast between the refractive index in the HMMs and in the AHM, the peaks are very sharp and the quality factor of the resonances becomes large. Note that Fano resonances for cavities as small as 0.5 µm can be realized, which is drastically smaller than the wavelength in free-space (100 µm).

Interestingly, the sharpness of the resonances depends on the particular order. We observe in Figure 5.12 that odd orders are wider than even orders. By odd order we mean the first, third, fifth . . . peaks in Figure 5.12. This behaviour is caused by an interplay between the evanescent mode and the Fabry-Perot resonances, as confirmed by the fact that for large cavity widths, the evanescent background disappears and the sharpness of the peaks remains constant. The presence of the evanescent mode adds an extra amplitude to the reflection, which interferes with the symmetry of the odd and even Fabry-Perot resonances. This results in a more rapid phase change for the even Fano order and a slower one for the odd ones. This effect is much less visible in the metal-dielectric multilayer case (Figure 5.6), as the coupling with the two modes is too different there.

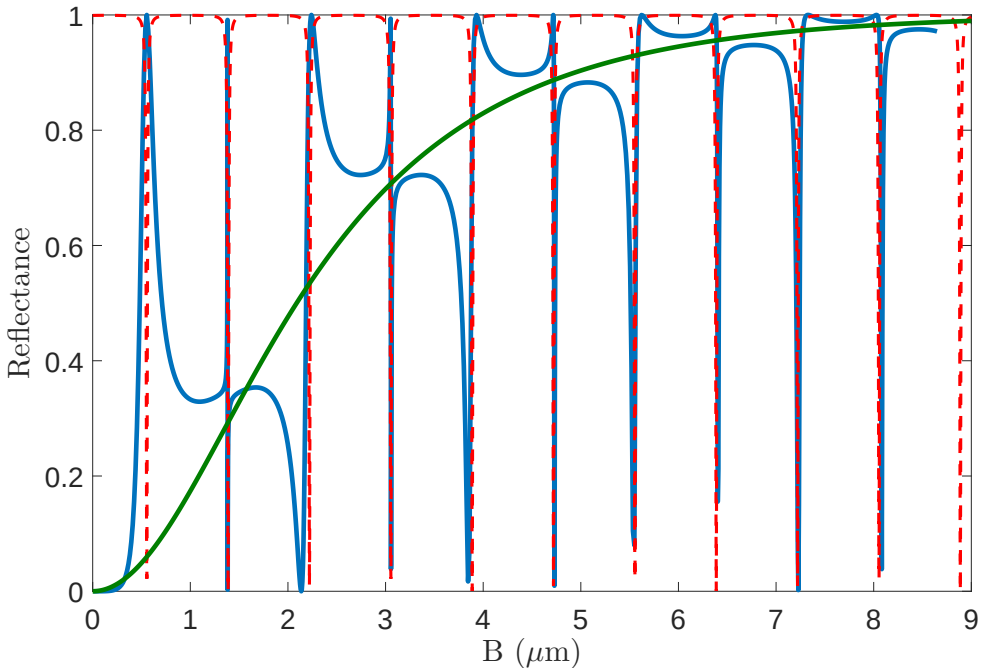

Figure 5.12: Comparison between the exact calculation of the reflectance (blue solid curve) and the slowly varying background of the evanescent mode (green solid curve) and the Fabry-Perot oscillations of the propagating mode (red dashed curve) for the graphene-based HMM with a tilt angle $\theta = 60°$ and $\lambda_0 = 100$ µm and a doping level $E_F = 0.1$ eV.

By calculating the refractive index inside the cavity, we can also demonstrate that the system is highly tunable. Combining Equation 5.20 with the transverse momentum conservation condition (Equation 5.11), we determine the refractive index for the propagating and evanescent mode (Figure 5.13). Thus, at the angle of Figure 5.12 ($\theta = 60°$), a small change of the doping level can lead to a drastic change in the wavevector of the propagating and evanescent modes.

For example, a small decrease of the doping level from 0.1 eV to 0.07 eV changes the refractive index of the propagative mode from about 60 to 100, and of the evanescent mode from about $4i$ to $2i$. This completely modifies the position and sharpness of the Fano resonances, see Figure 5.14 (blue curve compared to red curve). This tuning is not only geometric, but is also clearly visible in the dispersion spectra. Compare for example the blue curve to the red curve in Figure 5.15a ($B = 0.55$ µm), and in Figure 5.15b ($B = 1.38$ µm).

However, an increase of the doping level from 0.1 eV to 0.15 eV strongly reduces the refractive index of the propagative mode, and increases the imaginary part of the wavevector for the evanescent mode. Thus, the Fabry-Perot resonance becomes very broad (as the contrast between the HMM and AHM is low), and the evanescent background disappears for a very small cavity width. For these reasons, the Fano resonances are destroyed when increasing the doping level (Figure 5.14, yellow curve). The latter is also observed in the reflectance spectra (Figure 5.15a and 5.15b, yellow curve compared to red curve).

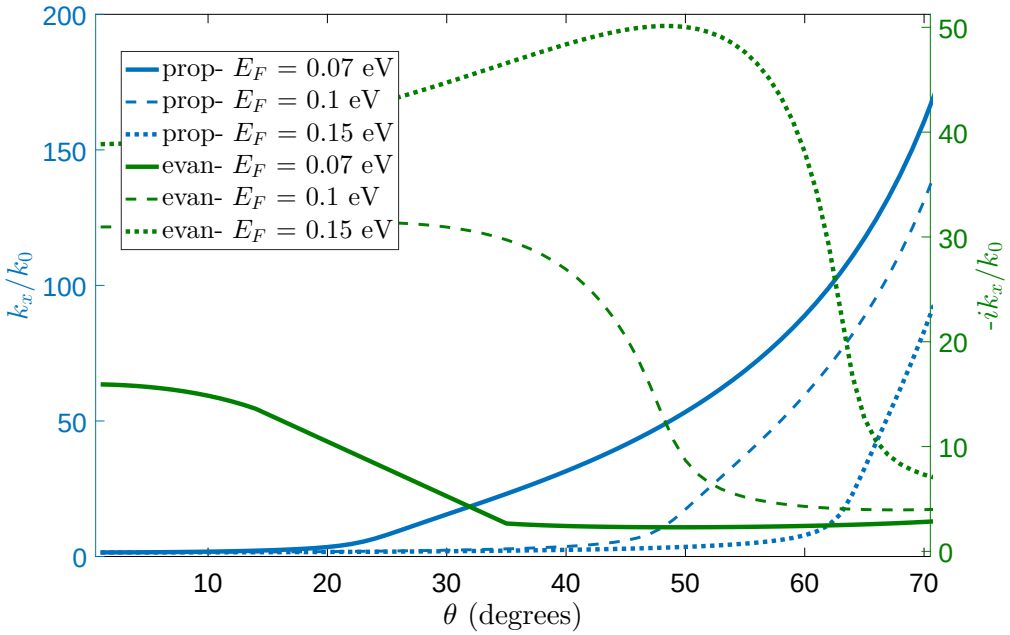

Figure 5.13: Momentum in the x direction k_x inside the graphene-based AHM in function of the tilt angle for $k_y = 0$, and various doping levels E_F. Blue curves and left axis represent the propagating mode, green curves and right axis represent the evanescent mode.

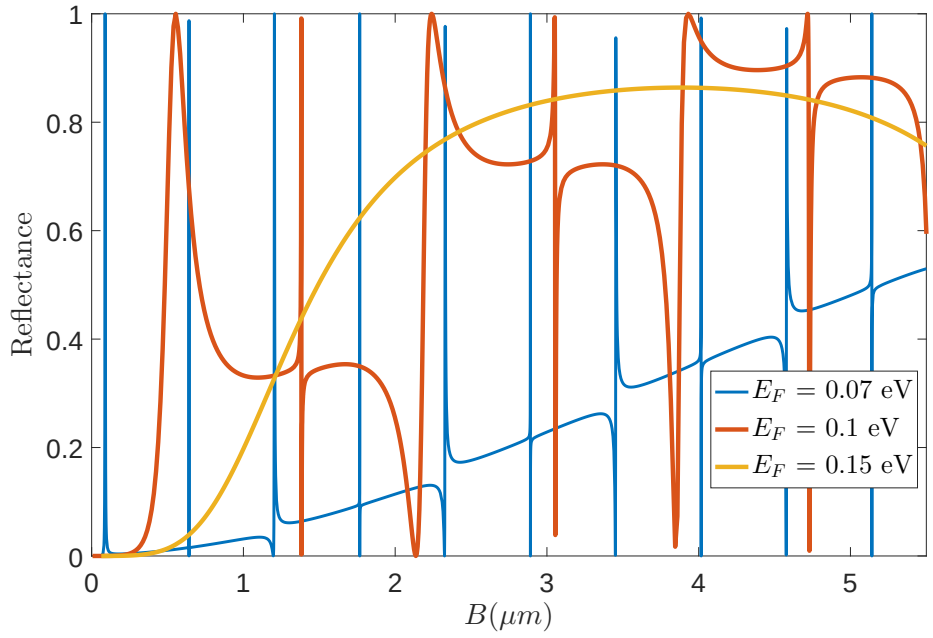

Figure 5.14: Reflectance versus the cavity width B for various doping levels. Blue curve corresponds to $E_F = 0.07$ eV, red curve to $E_F = 0.1$ eV, and yellow curve to $E_F = 0.15$ eV.

5.5 Loss effect

In this section, we return to the metal-dielectric structure, and study the influence of loss on the Fano resonances. Therefore, we use a Drude model with loss for the

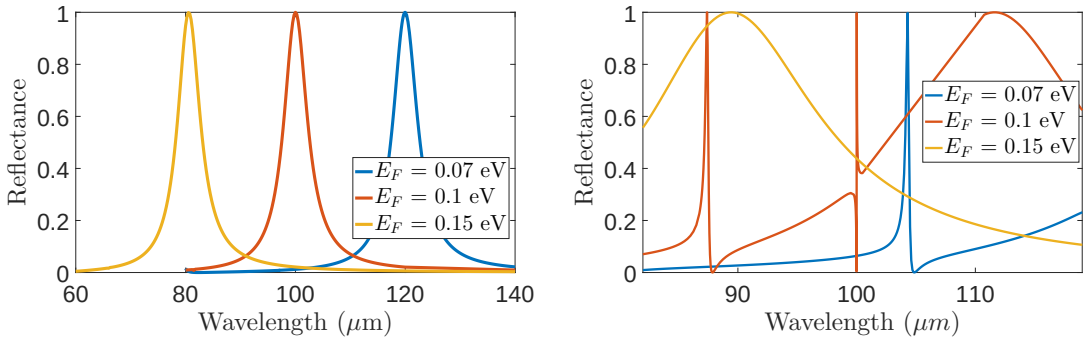

(a) $A = 0.96$ µm, $B = 0.55$ µm (b) $A = 2.39$ µm, $B = 1.38$ µm

Figure 5.15: Reflectance spectra of the graphene-based multilayer for various doping levels: (a) $A = 0.96$ µm, $B = 0.55$ µm, (b) $A = 2.39$ µm, $B = 1.38$ µm.

metal. The collision frequency in Equation 5.1 is now $\gamma = 0.5 \times 10^{14}$ rad/s, which fits well with experimental measurements [76, 106].

Unlike the lossless model, modes with purely real or purely imaginary propagation constant do no longer exist. However, the mainly evanescent and propagating modes still exist (if losses are not too large) and are excited with the provision of momentum conversation. Furthermore, in order to show the same Fano mechanism as in the previous section, the modal parameters should obey certain conditions. Specifically, the propagating mode should have a large real part and small imaginary part of the modal refractive index in the x direction, whereas the evanescent mode should have an imaginary part of the mode index in the x direction in the range between around 1 and 2 (above 2 the Fano resonances disappear quickly, below 1 the slowly varying background is not effective).

We focus on structures with metal filling fraction $f = \frac{1}{3}$ as in the previous sections. Equation 5.14 is still valid, so we can calculate the refractive index of the modes inside the AHM. Figures. 5.16 and 5.17 show the ratio between the real and imaginary parts of the propagating mode, and the imaginary part of the evanescent mode, respectively. The structure with period of 30 nm and tilt angle of 65° respects the conditions cited above, so we use these parameters for the simulations.

From the field profiles (insets of Figure 5.8) we can see hotspots created by sharp corners. These hotspots are critical in the presence of loss and can kill the resonance effect, therefore we limit their influence by replacing sharp corners with sections of 10 nm radius circles.

The reflectance and transmittance in function of the cavity width B is shown in Figure 5.18. We still observe the Fano resonances and the extreme sensitivity to small changes in the cavity width. The cavity principle thus remains operational, as the spectrum in Figure 5.19 also illustrates. Note that the decrease in transmittance corresponds to an increase in reflectance, so it is an interference effect, and not only due to metal absorption.

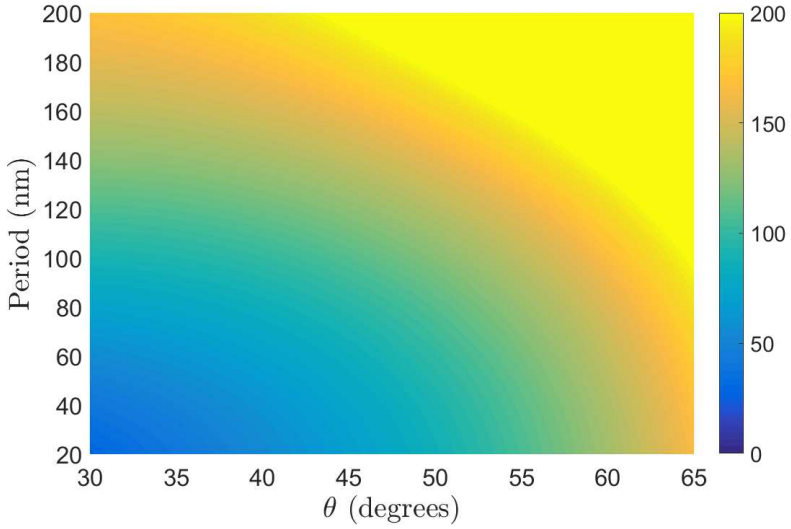

Figure 5.16: Ratio between the real and imaginary parts of the refractive index of the propagating mode inside the AHM.

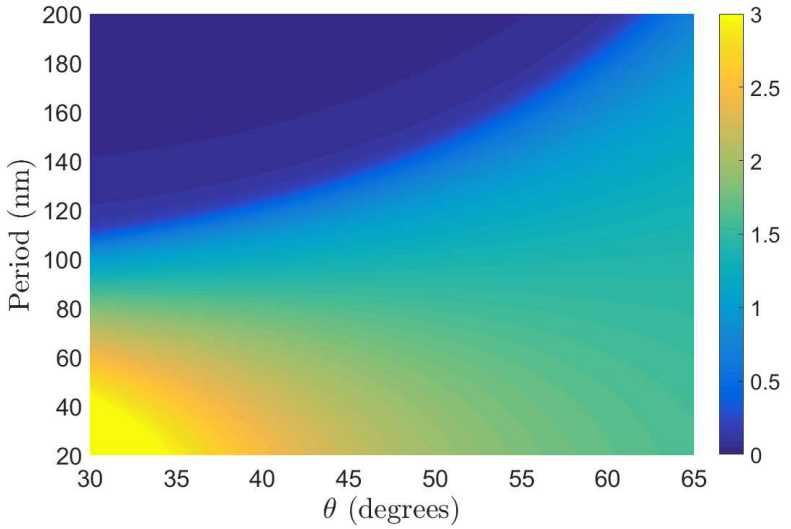

Figure 5.17: Imaginary part of the refractive index of the evanescent mode inside the AHM.

5.6 Summary

We show in this chapter the possibility to excite Fano resonances in multilayers with a central tilted section that functions as a cavity. Inside this cavity, for normal incidence ($k_y = 0$), momentum conservation allows a propagating mode and an evanescent mode to always be excited, the propagating mode being responsible for Fabry-Perot oscillations, while the evanescent mode 'direct' channel leads to a slowly varying background.

Furthermore, we have clearly shown that the effective medium theory breaks down and cannot explain the existence of these resonances, as it only predicts a

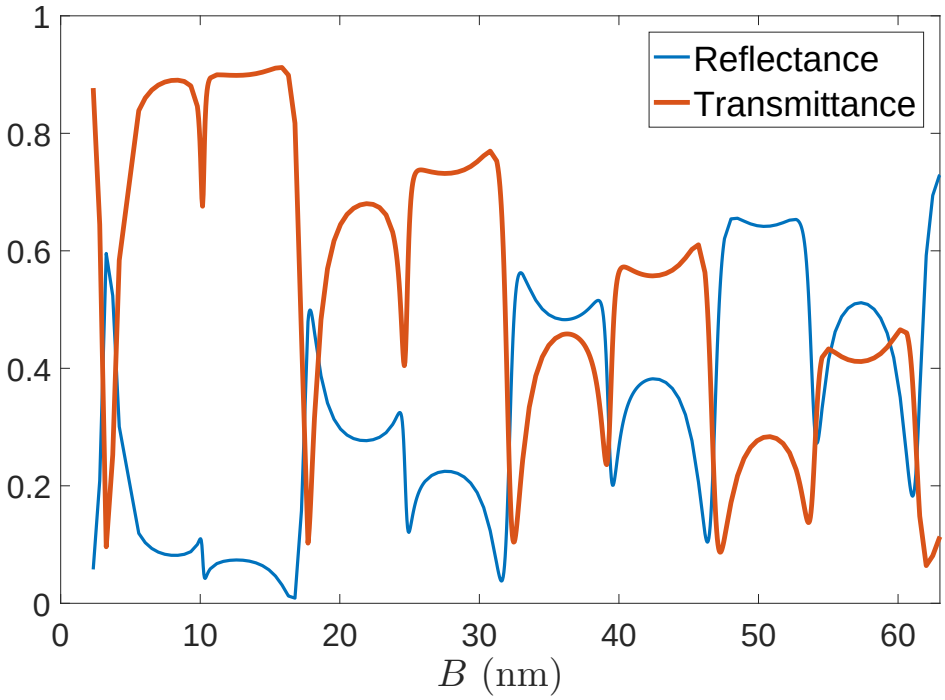

Figure 5.18: Reflectance and transmittance with period 30 nm and tilt angle 65° with losses. Blue curve corresponds to the reflectance, red curve to transmittance.

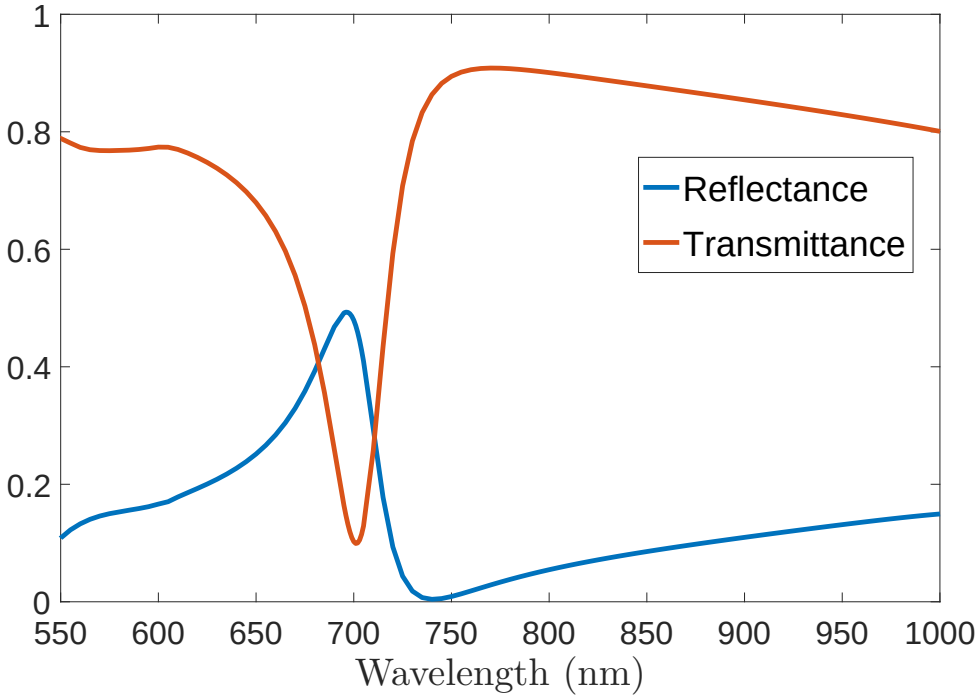

Figure 5.19: Reflectance and transmittance spectrum with period 30 nm, tilt angle of 65° and cavity width $B = 17.7$ nm with losses. Blue curve corresponds to the reflectance, red curve to transmittance.

single mode at a time, either propagating or evanescent.

Thanks to the hyperbolicity of the multilayer, relatively large effective indices inside the cavity offer the possibility to create very compact subwavelength cavities, as small as 5 nm in the visible regime with metal-dielectric multilayers, and 0.5 μm in the terahertz regime with graphene-based multilayers. In addition, the specific characteristics can be tailored, either presenting total transmittance or total reflectance at resonance, or exhibiting an asymmetric spectrum.

For the graphene-based multilayers, the doping level is another parameter to control the position and sharpness of the Fano resonances, with a variation as small as 0.03 eV changing completely the reflectance spectrum. Moreover, compared to the metal-dielectric devices, light incoupling can be easier because the mode index is approximatively equal to the index of the dielectric at normal incidence, avoiding the necessity to rely on incoupling techniques such as gratings or prisms.

Finally, we have taken metal losses into account and we have shown that these Fano resonances still exist. This bimodal interference mechanism in slanted cavities is therefore quite general and offers new practical possibilities, in particular in the domain of sensing applications thanks to their sharpness.

Most of the work of this chapter on the metal-dielectric multilayers was presented in [107] and [108].

6

Strong coupling and exceptional points in active HMM

Like many metamaterials based on metal-dielectric structures, hyperbolic metamaterials suffer from high ohmic losses [92, 109, 110]. For example, their usefulness for spontaneous emission enhancement is limited by emission in dissipative channels through quenching in the metallic constituents [35]. The inclusion of gain media in the dielectric material offers a pathway to mitigate these losses [111–117], and gives rise to the new class of active HMMs, where light strongly interacts with quantum transitions of the active medium [18, 20, 118, 119].

In this chapter we investigate a multilayer HMM structure infiltrated with dye molecules inside the dielectric layers, which can conveniently be modelled on the basis of a four-level (quantum) system. While the weak coupling regime was studied for loss-compensation [91], we consider strong coupling with large oscillator strengths, where light enters a dressed state with electronic transitions associated with both the absorption and the emission line of the dye [58, 120, 121]. Previously, Shekhar and Jacob [122] theoretically investigated strong coupling between the intersubband absorption line of a multiple quantum-well gain medium and the bulk polariton of a finite HMM. However, the simultaneous interaction of light with an absorption and an emission line, as present in optically pumped gain media such as dyes, has to the best of our knowledge not been studied yet.

The proposed HMM is fundamentally simple to fabricate and features a band-structure optimized for efficient incoupling from within the light cone. It also exhibits rich physics that ties multiple concepts together, as exposed by detailed analytical and numerical modeling. The absorption line of the dye leads to strong coupling features, with large momentum modes exhibiting the typical avoided crossings via Rabi splitting. On the other hand, the gain provided gives rise to exceptional points (EPs) close to the emission line, which are actively examined in parity-time ($\mathcal{PT}$) symmetry studies [123, 124]. We show that these EPs lead to group velocity singularities and arise naturally when the band edges intersect with the inversion line, i.e., where the losses are precisely compensated by gain. Thus the four-level dye brings various related features together in a judiciously tailorable fashion. Both finite and infinite multilayers are discussed, each time showing the same class of effects, but in a particularly distinctive way. An important result is our semi-analytical theory, which faithfully models and explains the behaviours of the modes at play, and matches very well with exact transfer-matrix calculations.

In Section 6.1 we detail the structure, together with the dye parameters, and analyze the passive dispersion diagram. The theory for passive and optically pumped active HMMs is presented in Section 6.2, including a semi-analytical model for coupling with the electronic dye transitions. In the results Section 6.3 we first discuss the interaction of finite and infinite HMMs with absorption or emission lines in isolation, and then with the full four-level dye model.

6.1 Design

As a practical realization of an optically pumped HMM we propose a multilayer structure where dye-infiltrated epoxy is spin-coated on silver layers [27], represented in Figure 6.1a (period delimited by the orange dashed lines). The dye that provides gain is represented by a four-level model, with energy levels as sketched in Figure 6.1b. Pumping of the dye and population inversion involves the excitation of electrons from the fundamental level with energy E_1 to the excited state E_2 (blue arrow in Figure 6.1b). The electrons relax through fast non-radiative processes (green arrows in Figure 6.1b) and spontaneous and stimulated light emission occurs via the optically active transition from E_3 to E_4 providing gain (red arrow in Figure 6.1b).

Further, to accommodate for optical pumping and solve the problem of light-injection into hyperbolic modes literally on the fly, we propose a structure where high-energy pump light can propagate inside the structure to excite the dye, providing gain at the lower emission frequency. A typical dispersion of a hyperbolic multilayer is depicted in Figure 6.2, where the orange curves are the dispersions at the center of the Brillouin zone and the purple curves at the edge of the Brillouin zone (see below for more details).

The multilayer presents thus two distinct plasmonic bands, the lower one providing the propagation of extremely high momentum waves (red shaded zone in Figure 6.2), and the upper one lying partially inside the light cone (grey shaded zone in Figure 6.2). For this reason it is crucial that the absorption line of the dye falls within the upper band inside the light cone, while the emission line resides in the lower band (horizontal dashed lines in Figure 6.2). This particular arrangement

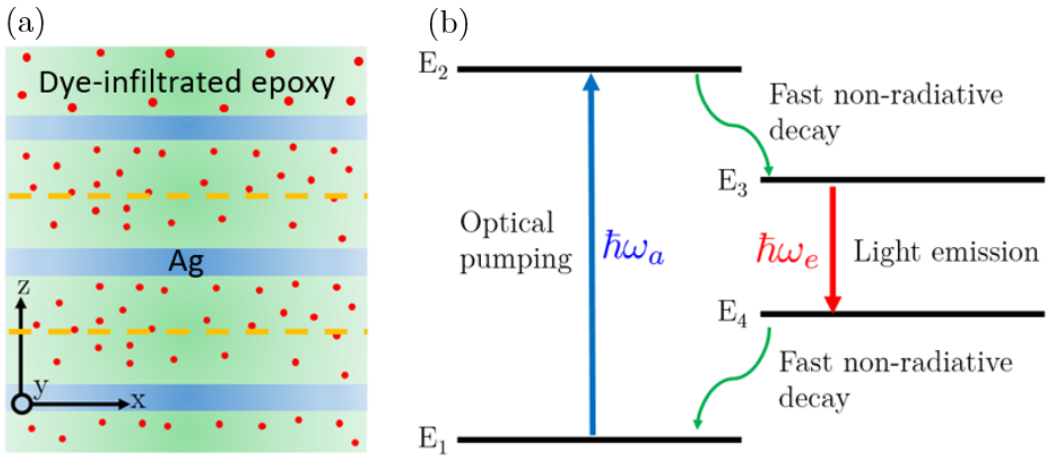

Figure 6.1: (a) Schematic of the active HMM, consisting of silver (blue) and dye infiltrated (red dots) epoxy layers (green), with a unit cell marked by orange dashed lines. (b) Energy diagram of a four-level dye molecule, with an absorption (blue) and emission line (red).

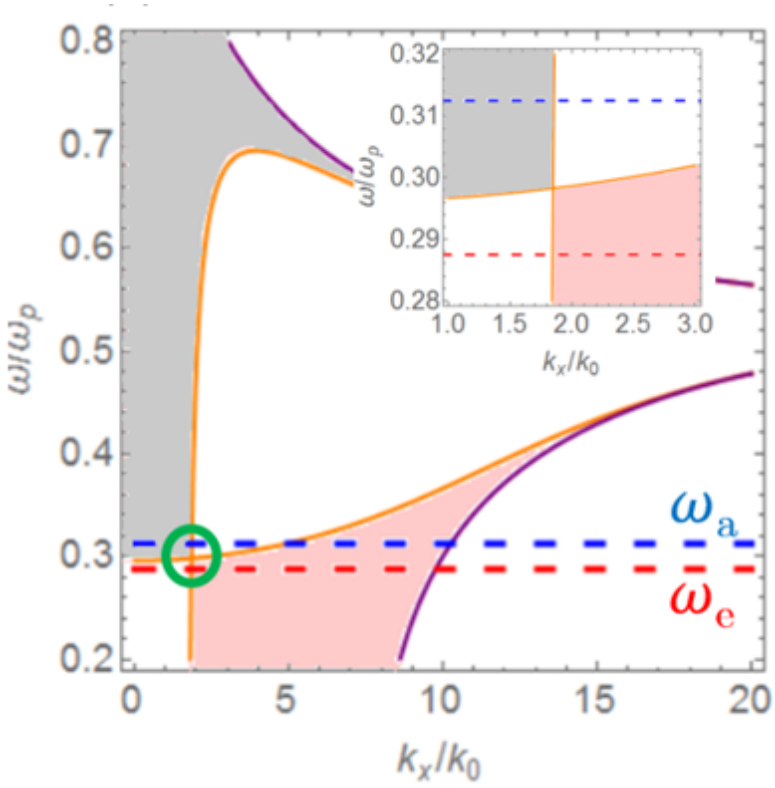

Figure 6.2: Illustration of the plasmonic bands of the passive HMM with the dye absorption line at frequency ω_a (blue dashed line) above and the emission line at frequency ω_e (red dashed line) below the intersection point, highlighted by the green circle, where the upper (grey shaded) and lower band (red shaded) connect. Inset shows a zoom on this intersection point.

allows for light emission into the hyperbolic modes, benefiting simultaneously from both a strong field enhancement and large wavevectors.

6.2 Theory

In this section we start with a standard theory of passive HMMs, then we motivate our choice of parameters for the dye-infiltrated structure, and subsequently we develop a semi-analytical model that describes optical mode coupling with the dye transitions.

6.2.1 Passive HMMs

Effective medium theory is often used to approximately describe the optical properties of hyperbolic multilayers [78, 79, 125]. However, as we pointed out in Chapters 2 and 5, the effective medium model becomes increasingly inaccurate for larger wavevectors and frequencies, as the quasi-static approximation breaks down [8, 50, 126].

Rather than relying on the effective medium approximation, we use the exact dispersion relation (for TM polarization), which is found directly by solving Bloch's eigenvalue equation $M\mathbf{b} = \lambda_{\pm}\mathbf{b}$, where M is the transfer matrix of the unit cell, and $\mathbf{b}$ the Bloch eigenvectors (see Section 2.4.1). The Bloch eigenvalues can be represented as $\lambda_{\pm} = e^{\pm ik_z D}$ where $D = d_m + d_d$ is the thickness of the unit cell, and k_z the Bloch wavevector. The exact dispersion for a two-layer metal-dielectric HMM is [49, 51]

$$\begin{aligned}\Lambda = \cos(k_z D) = &\frac{(\kappa_d\varepsilon_m + \kappa_m\varepsilon_d)^2}{4\kappa_d\kappa_m\varepsilon_d\varepsilon_m}\cosh(\kappa_d d_d + \kappa_m d_m) \\ &- \frac{(\kappa_d\varepsilon_m - \kappa_m\varepsilon_d)^2}{4\kappa_d\kappa_m\varepsilon_d\varepsilon_m}\cosh(\kappa_d d_d - \kappa_m d_m)\end{aligned} \tag{6.1}$$

with decay coefficients $\kappa_{d,m} = (k_x^2 - k_0^2\varepsilon_{d,m})^{1/2}$ in the dielectric and metallic layers, respectively. In this work a simple Drude model (Equation 2.8), $\varepsilon_m = 1 - \omega_p^2/(\omega^2 + i\omega\gamma_p)$, with plasma frequency $\omega_p = 1.26 \times 10^{16}\,\mathrm{rad/s}$ and damping rate $\gamma_p = 5 \times 10^{13}\,\mathrm{s}^{-1}$ is used to model the silver layers in the visible regime [89, 90, 106]. Using Eq. 6.1 we can express the Bloch eigenvalues as

$$\lambda_{\pm} = \cos(k_z D) \pm i\sin(k_z D) = \Lambda \pm i\sqrt{1 - \Lambda^2}\,. \tag{6.2}$$

Thus, the eigenvalues become degenerate when $\Lambda = \pm 1$, which implies $\mathrm{Re}(\Lambda) = \pm 1$ and $\mathrm{Im}(\Lambda) = 0$, i.e., when $k_z D$ is purely real and the Bloch wavector is at the center or edges of the Brillouin zone (where $k_z = 0$ or $k_z = \pi/D$ so $\cos(k_z D) = \pm 1$). This statement remains valid for active multilayer structures and implies the existence of exceptional points at the intersection of the loss-compensation curves (defined by the $\mathrm{Im}(\Lambda) = 0$ condition) and the edges of the plasmonic bands (more details later in the Results Section 6.3).

As explained in the previous section, the intersection point between the upper and lower bands of the HMM (highlighted by the green circle in Figure 6.2) is of

particular interest for the design of the active, optically pumped HMM, and the geometric and dye parameters should be selected carefully. As we have derived in Section 2.4.2, this intersection point has the frequency (Equation 2.37):

$$\omega_i = \frac{\omega_p}{\sqrt{1 + \varepsilon_d(d_d/d_m)}}. \tag{6.3}$$

To facilitate pumping into the upper band and emission into the lower band (horizontal lines in Figure 6.2), the layer thicknesses need to be chosen such that for the given dye the peaks of absorption and emission lines fall above and below the intersection point, respectively.

6.2.2 Dye-Infiltrated Multilayer

To demonstrate the feasibility of optical pumping in the structure, we consider realistic material parameters for the dye model. Rhodamine 6G, frequently used for loss-compensation in optical metamaterials [127, 128], has peak emission and absorption wavelengths at 520 nm and 480 nm, which translates into angular frequencies $\omega_e = 0.288\,\omega_p$ and $\omega_a = 0.313\,\omega_p$. The respective linewidths are approximately $\gamma_{e,a} = 0.005\,\omega_p$. With the dye embedded in epoxy ($\varepsilon_{\text{epoxy}} = 2.56$) the permittivity of the active dielectric layers is modeled by Lorentzians (see Appendix A for more details)

$$\varepsilon_d = 2.56 + g_a L(\omega_a, \gamma_a) + g_e L(\omega_e, \gamma_e) \tag{6.4}$$

where

$$L(\omega_j, \gamma_j) = -\frac{2}{\pi}\frac{\omega_j}{(\omega^2 - \omega_j^2 - \gamma_j^2) + 2i\gamma_j * \omega} \tag{6.5}$$

is the normalized second-order Lorentzian line-shape function of the excitonic transitions. The coupling strengths g_a and g_e determine the oscillator strength of the absorption and emission lines, respectively. While they generally depend on the population of the various levels (Figure 6.1b), we here assume an inverted system with equal coupling strengths but opposite signs, $g_e = -g_a$ (where $g_a > 0$), for the emission and absorption lines.

To push the absorption line into the upper and the emission line into the lower band (Figure 6.2) we align the intersection point (green circle in Figure 6.2) between the two transitions at $\omega = 0.3\,\omega_p$. From Eq. 6.3 we thus find the required ratio of layer thicknesses $d_d \approx 4\,d_m$. In addition, to allow for large wavevectors, which are useful for instance for imaging applications, we aim for a large bandwidth of the lower band. The period therefore needs to be as small as possible, as the wavevector along z is limited by the Brillouin zone edge ($|k_{z,max}| = \pi/D$). Considering fabrication constraints we choose $d_m = 5\,\text{nm}$, as vapor deposited silver layers of this thickness are sufficiently smooth when a 1 nm thick germanium layer is used as a wetting layer [27, 129], and $d_d = 20\,\text{nm}$, which is readily achievable by spin-coating.

To determine the effectiveness of the optical pump scheme, we first calculate the light transmittance of the passive multilayer for a finite structure of 10 periods. Figure 6.3a shows that transmission of incident waves above $\omega = 0.3\,\omega_p$ from inside the light cone is almost perfect (white region). Note that, for finite multilayers the plasmonic bands are replaced by discrete modes, as opposed to the continuous

bands observed for infinite structures. A typical eigenmode profile is presented in Figure 6.3b, showing the magnetic field profile of the third discrete eigenmode of the lower band at $\omega = 0.25\,\omega_p$ (marked by a black star in Figure 6.3a). This mode is symmetric and presents three maxima and two nodes. When the order of the mode increases, the number of nodes increases and the interaction with the gain medium is then reduced.

As the passive structure is almost transparent to the pump, absorption of light by the dyes should be effective. To confirm this we calculate (with the commercial finite-element software COMSOL Multiphysics 5.2) the absorbance within the various layers with dyes for normal incidence ($k_x = 0$), by taking into account the absorption line only (emission switched off), see Figure 6.3c. The total absorbance by the dyes (blue curve) at the central absorption frequency is almost 90%, with about 25% of the light absorbed in the first period (brown curve), and 10% in the fifth period (yellow curve). For the last period (purple curve) the absorbance is small as most of the light has already been absorbed. We note that with the population numbers fixed, this analysis neglects saturation effects, which render the dielectric layers transparent with increasing pump strength, until all layers are equally pumped into inversion.

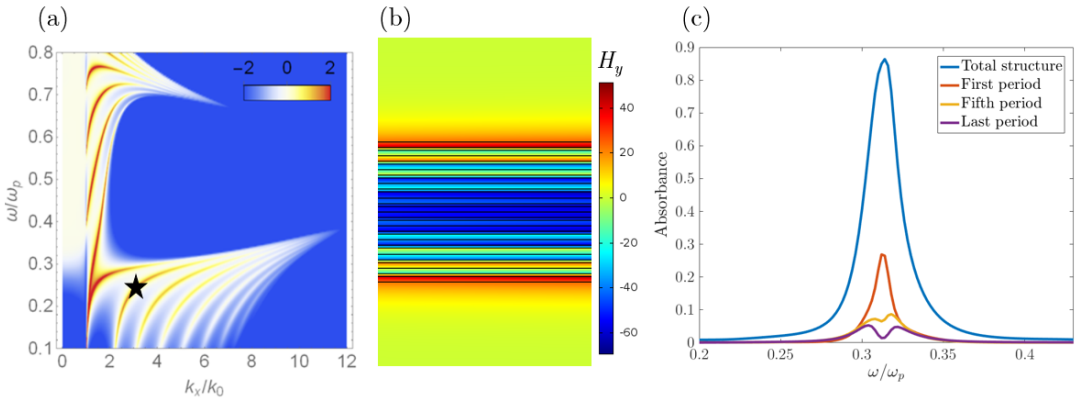

Figure 6.3: (a) Transmittance of a finite HMM of 10 periods with thickness $d_m = 5\,\text{nm}$ (logarithmic scale). (b) Magnetic field profile H_y of the third eigenmode of the lower band at $\omega = 0.25\,\omega_p$, marked by a black star in Figure 6.3a. (c) Absorbance at normal incidence ($\omega_a = 0.313\,\omega_p$) of the dyes for the whole structure (blue curve), the first period (brown curve), the fifth period (yellow curve) and the last period (purple curve), respectively.

6.2.3 Semi-Classical Model

To understand the coupling of the modes with the dyes, we develop a model that describes the behaviour of the oscillators. As the four-level dye presents an absorption and an emission line, with opposite signs for the coupling strength, we expect to have two distinct interactions at these frequencies.

For finite structures (Figure 6.3a) the continuous bands are replaced by discrete resonant modes, with the number of these modes per band equal to the number of periods (there are 10 modes for a 10-period stack, note that some of the modes are

invisible with the scale of Figure 6.3a). When infiltrated with dyes, coupling between these discrete modes and the excitonic lines occurs. For simplicity, we first examine coupling with only one excitonic line (either the emission or absorption line) before showing the full model. From the Maxwell-Bloch equations and the wave equation we derive a semi-classical model for this system, which results in coupled oscillator equations for the modal field amplitude E and the polarization of the respective transition P (see details in Appendix A):

$$\partial_t \begin{pmatrix} E \\ P/\varepsilon_0 \end{pmatrix} = -i\Omega_\pm \begin{pmatrix} E \\ P/\varepsilon_0 \end{pmatrix} = \begin{pmatrix} -i\Omega_m & iA_m \\ iK_{12} & -i\Omega_{12} \end{pmatrix} \begin{pmatrix} E \\ P/\varepsilon_0 \end{pmatrix}, \tag{6.6}$$

where Ω_m and Ω_{12} are the complex frequencies of the selected optical mode and the excitonic transition (absorption or emission), whose negative imaginary parts are the modal damping rate γ_m and the linewidth of the transition (γ_a or γ_e), respectively. The off-diagonal coupling terms are determined as $A_m = \Omega_m\Gamma/2$ and $K_{12} = \sigma_{12}/\varepsilon_0$, introducing the spatial overlap factor Γ of the plasmonic mode with the dielectric medium, and the cross-section σ_{12} of the excitonic transition under consideration. The latter relates to the coupling strength of the oscillator via $g = \pi\sigma_{12}/\varepsilon_0$.

Solving for the eigenfrequencies $\Omega_\pm$ of the coupled system we find

$$\Omega_\pm = \frac{1}{2}(\Omega_m + \Omega_{12}) \pm \frac{1}{2}\sqrt{4K_{12}A_m + (\Omega_m - \Omega_{12})^2}, \tag{6.7}$$

which defines the mode splitting within the semi-classical coupling model for two oscillators. Note that, with all other parameters determined, the only remaining parameters to fit are the frequency of the selected optical mode Ω_m, and its spatial overlap factor Γ with the gain layers. Both parameters only depend on properties of the passive structure and are independent of the dye characteristics. For the given structure we determine $\gamma_m \approx 0.004\,\omega_p$ for the decay rate of the modes (γ_m does not change much for the various modes of the lower band) and an overlap factor of $\Gamma \approx 1/3$ as best fits to the modes shown in Figure 6.3a. Both parameters prove to be relatively frequency insensitive within the range under consideration (between 0.2 and 0.4 ω_p).

Unlike the standard classical oscillator model, the semi-classical model predicts different behaviours for the absorption and emission cases. Indeed, the cross-section σ_{12} is related to the population levels via

$$\sigma_{12} = -\frac{\boldsymbol{\mu}_{12}^2(N_2 - N_1)}{3\hbar} \tag{6.8}$$

where μ_{12} is the dipole matrix element, N_1 and N_2 the density of atoms in the ground state and excited states, respectively. For absorption transitions (where $N_2 < N_1$) Eq. 6.7 describes the usual transition from weak coupling to strong coupling, manifesting itself as vacuum Rabi splitting within the semi-classical framework. As the cross-section becomes negative for emission processes ($N_2 > N_1$), the term $4K_{12}A_m$ in the discriminant of Eq. 6.7 becomes negative too. For sufficiently large coupling strength g_e the sign flip for an emission line produces a splitting behaviour similar to the fork observed in $\mathcal{PT}$-symmetry breaking scenarios. These two distinct behaviours will be described in detail in Section 6.3 where we discuss the results.

In the complete case of four-level dyes, coupling occurs simultaneously to both emission and absorption lines. Each line provides its own polarization P_e and P_a that interacts with the amplitude E of the optical mode. This results in a modified coupling model:

$$\partial_t \begin{pmatrix} E \\ P_a/\varepsilon_0 \\ P_e/\varepsilon_0 \end{pmatrix} = -i\tilde{\Omega} \begin{pmatrix} E \\ P_a/\varepsilon_0 \\ P_e/\varepsilon_0 \end{pmatrix} = \begin{pmatrix} -i\Omega_m & iA_m & iA_m \\ iK_a & -i\Omega_a & 0 \\ iK_e & 0 & -i\Omega_e \end{pmatrix} \begin{pmatrix} E \\ P_a/\varepsilon_0 \\ P_e/\varepsilon_0 \end{pmatrix} \quad (6.9)$$

where Ω_a and Ω_e denote the complex frequencies of absorption and emission lines, respectively. The matrix elements $K_{a,e} = \sigma_{a,e}/\varepsilon_0$ are expressed in terms of the cross-sections σ_a and σ_e, which in turn are proportional to the coupling strengths g_a and g_e, respectively. It follows that solving the eigenvalue equation determines the three eigenfrequencies $\tilde{\Omega}$. As $K_a > 0$ and $K_e < 0$, a mixed behaviour of Rabi splitting and $\mathcal{PT}$-symmetry breaking is expected for sufficiently large coupling strengths, as discussed next.

6.3 Results

Having introduced the structure and the semi-analytical theory, we proceed to investigate the active HMM dispersion. Again we first consider the absorption and emission lines in isolation, and later we employ the full four-level dye system. In each part we compare the discrete mode behaviour in finite structures with the resulting deformation of bands in infinite structures. The semi-classical model is applied to a specific discrete mode, and provides a good description of the behaviour for finite devices in all cases (loss, gain and both). As we will see, the absorption line produces the classical strong coupling behaviour (Rabi splitting), whereas the emission line leads to a fork-like splitting and the appearance of exceptional points.

6.3.1 Absorption line: weak and strong coupling

We focus on the effect of an absorption line on the dispersion, ignoring the emission for the moment. Qualitatively we can distinguish two regimes, a weak coupling regime characterized by small distortions of the dispersion, and a strong coupling regime leading to Rabi splitting of modes.

Figure 6.4a shows the reflectance map of a 10-period finite structure via transfer-matrix calculations, with each reflectance maximum indicating a discrete plasmonic mode. For a small value of the oscillator coupling strength ($g_a = 3 \times 10^{12}$) a slight perturbation and smearing of the optical modes is observed around $\omega_a = 0.313\,\omega_p$ when compared with the passive case (Figure 6.3a).

When applying the semi-classical model to two particular modes (green and magenta curves in Figure 6.4a), one obtains an excellent fit to the exact transfer-matrix results. A slight deviation from the passive case around ω_a is visible for the green curve e.g., indicating the coupling with the dye. We can understand the weak coupling from the model equations 6.7, as in this regime $|4K_aA_m| \ll |\Omega_m - \Omega_a|^2$, so $\Omega_+ \approx \Omega_m$ and $\Omega_- \approx \Omega_a$. This means that one mode retains the character of the optical mode, and the other that of the excitonic line.

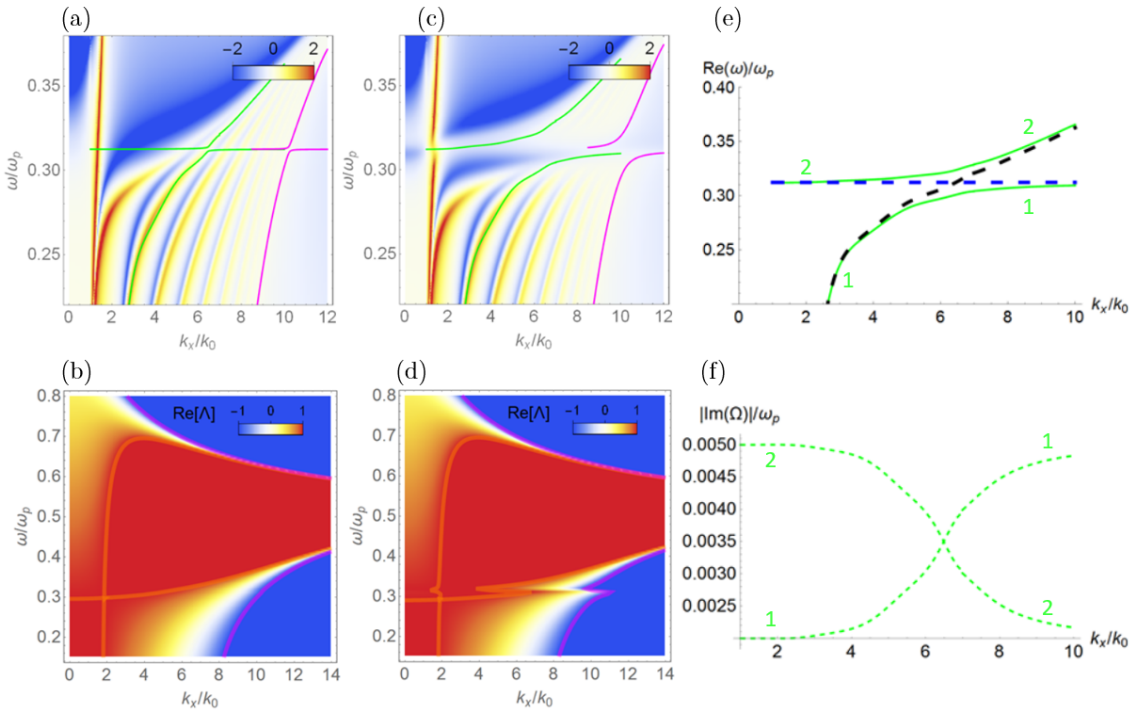

Figure 6.4: (a) Reflectance with an absorption line in the weak coupling regime ($g_a = 3\times10^{12}$) and (c) strong coupling regime ($g_a = 10^{14}$) for the finite structure (logarithmic scale). The green and magenta curves are obtained via our semi-classical model for two different modes. (b) Dispersion diagram of the infinite structure with an absorption line in the weak coupling regime and (d) strong coupling regime. Orange curves are the edges of the plasmonic band at the center of the Brillouin zone ($\mathrm{Re}(\Lambda) = 1$) and magenta curves at the edge of the Brillouin zone ($\mathrm{Re}(\Lambda) = -1$). (e) and (f) real and imaginary parts of the complex eigenfrequencies $\Omega_\pm$ obtained with the model (green curves) in the strong coupling regime. Blue dashed curve is the excitonic absorption line and black dashed curve is the unperturbed optical mode. The two polaritons resulting from the coupling of the optical mode with the excitonic line are identified by the numbers 1 and 2 (Ω_- and Ω_+, respectively).

A similar small perturbation around ω_a is observable at the band edge of the infinite multilayer (Figure 6.4b) showing the real part of Λ (analytically calculated with Eq. 6.1). The orange curves correspond to the plasmonic band edge at the center of the Brillouin zone ($\mathrm{Re}(\Lambda) = 1$), while the magenta curve is the plasmonic band edge at the edge of the Brillouin zone ($\mathrm{Re}(\Lambda) = -1$). Comparing the band edges in the active case of Figure 6.4b (orange and magenta curves) with the band edges in the passive case of Figure 6.2 (orange and purple curves), one can see that the absorption line causes only a very small deviation.

However, the dispersion qualitatively changes in the strong coupling regime for a larger coupling strength ($g_a = 10^{14}$, Figure 6.4c), where anti-crossings appear and a gap opens in the reflectance map. This effect is particularly visible for the discrete modes of finite structures, and we plot the same two modes as before using the model with green and magenta curves. Again, the model fits well with the exact results, even in this strongly coupled case. We can understand the behaviour

by inspection of Eq. 6.7: close to the crossing point of the optical mode and the excitonic line ($\omega_m = \omega_a$) the first term in the square root dominates and one obtains $(\Omega_m - \Omega_a)^2 \approx (\gamma_m - \gamma_a)^2$. If $\mathrm{Re}(4K_aA_m) \gg (\gamma_m - \gamma_a)^2$ and $\mathrm{Re}(4K_aA_m) \gg \gamma_m, \gamma_a$ (the resonance linewidth of the optical mode and the exciton needs to be smaller than the splitting to be in the strong coupling regime), the square root becomes real and a gap opens. The width of this gap is the Rabi splitting energy $\hbar\Omega_{Rabi} = \sqrt{2K_aA_m}$, with A_m containing the overlap factor Γ. When the order of the optical mode increases, the number of nodes of the mode profile also increases, reducing slightly Γ and thus the Rabi splitting. An analogous situation was reported by Shekhar and Jacob [122], where they studied the interaction between intersubband transitions of multiple quantum well layers and optical modes in a HMM.

Interestingly, our model allows to directly determine the Rabi splitting with only prior knowledge of the dispersion characteristics of the unperturbed optical mode and the absorption line (Figure 6.4e). Figure 6.4e shows the dispersion of the polaritons calculated with our model (green curves) using parameters of the excitonic line (blue dashed curve) and the unperturbed optical mode (black dashed curve). Away from the crossing, the polaritons simply follow the two components, with one polariton being dominantly plasmonic (polariton 1) while the other is dominantly excitonic (polariton 2) for small wavevector k_x (and vice versa for large k_x). At the crossing point a gap opens and the two polaritons are a mixed state between an excitonic and a plasmonic mode.

Another advantage of our model is that we can not only retrieve the real parts of the polaritonic eigenfrequencies, but also their imaginary parts (Figure 6.4f), thus providing the essential mode characteristics, while most other models convey only the real parts. For example, the imaginary parts of $\Omega_\pm$ are small in the region where we can see the modes in Figure 6.4c, and large in the more blurry parts where the modes become overdamped. This is the reason why only polariton 1 is visible for small wavevectors k_x (as the imaginary part of the eigenfrequency of polariton 1 increases in magnitude with k_x) and only polariton 2 for large k_x (as the imaginary part of the eigenfrequency of polariton 2 decreases in magnitude with k_x).

The strong coupling effect is also observed in the infinite structure (Figure 6.4d), where bands arise from the continuum of resonances. In the absence of discrete resonances the impact of strong coupling is less obvious, as the gap effectively closes due to the superposition of an infinite number of dispersive modes. At the band edges however, a strong distortion is observed (analytical calculation of Λ in Figure 6.4d) around ω_a, which corresponds with the anti-crossings of the finite stack. Indeed, the band edges tend to larger or smaller values of k_x, below or above the absorption line, respectively.

6.3.2 Emission line: exceptional points

We next consider the emission line in isolation, ignoring the absorption line. For emission processes K_e (via σ_e) changes sign in Eq. 6.8, and the first term in the square root of Eq. 6.7 also changes sign. However, for a small coupling strength (such as $g_e = 3 \times 10^{12}$) one has $|4K_eA_m| \ll |\Omega_m - \Omega_e|^2$, so the situation is similar to a weakly coupled absorption line, where modes become only slightly perturbed

(not shown), just as in Figure 6.4a and 6.4b.

The situation becomes more interesting for larger coupling strength ($g_e = 10^{14}$) when the linewidths of the optical mode and emission line are similar and small compared to the frequencies, which is true for our parameters ($\gamma_m = 0.004\,\omega_p \approx \gamma_e = 0.005\,\omega_p$). Again we notice from the reflectance map of the finite structure (Figure 6.5a) that a gap opens for the plasmonic modes around the emission frequency ($\omega_e = 0.288\,\omega_p$). The modes bend towards smaller k_x below the emission line and towards larger k_x above. This behaviour is opposite to the previous case where we only took the absorption line into account. With the semi-classical model applied to two particular mode couples (green and magenta lines in Figure 6.5a), we again obtain a very good agreement with the exact results.

To understand the behaviour with the model equations, we examine the argument of the square root of Eq. 6.7: $\sqrt{4K_eA_m + (\omega_m - \omega_e)^2}$. As the first term becomes large and negative when the coupling strength increases, the square root becomes almost purely complex in the regime where $|4K_eA_m| > [\omega_m(k_x) - \omega_e]^2$, which means that both eigenfrequencies $\Omega_\pm$ have the same real parts but imaginary parts with opposite signs. In other words, this regime is similar to the broken-symmetry phase of $\mathcal{PT}$ systems that produce fork-like bifurcations and give rise to exceptional points when the two modes merge (similar to the splitting of the directional coupler modes, Figure 3.3). As a side note we point out that $\mathcal{PT}$-symmetric hypercrystals made of HMMs were studied in [130], but the gain was introduced in the dielectric surrounding the HMM, and not directly into the HMM as proposed here.

To analyze the coupling behaviour in more detail we show the uncoupled and coupled modes in Figure 6.5c for a particular optical mode (corresponding the the green curve in Figure 6.5a). The two branches of the fork correspond to the polaritons 1 and 2 in Figure 6.5c. However, only polariton 2 appears in the reflectance map of Figure 6.5a. The imaginary part of polariton 1 (not visible in Figure 6.5a) has a large imaginary part of the eigenfrequency (Figure 6.5d) and is therefore strongly damped (broadened line), while the polariton 2 has a smaller imaginary part and can thus be observed in Figure 6.5a as a sharp resonance, except in the gap region where its imaginary part is positive and large (gain).

The 'lines of points' appearing in the large gain case around $\omega = 0.27\,\omega_p$ and $\omega = 0.31\,\omega_p$ (highlighted by the blue arrows in Figure 6.5a) are not true exceptional points. Indeed, they would be 'pure' exceptional points if the square root in equation 6.7 would be zero (so that the eigenvalues are degenerate), which is not exactly the case here. However, these high-reflection points are regions where the imaginary part of the eigenfrequency of polariton 2 is close to zero (see Figure 6.5d), and thus the resonances becomes very sharp.

Just as for the absorption case, remnants of the fork-like splitting can be observed only at the edges of the plasmonic band of the infinite multilayer structure (Figure 6.5b, showing the real part of Λ). An important distortion is observed around $\omega_e = 0.288\,\omega_p$ where the band edges ($\mathrm{Re}(\Lambda) = +1$, orange curves, and $\mathrm{Re}(\Lambda) = -1$, magenta curves) undergo a distortion similar to the one of the resonances of the finite stack. Indeed, the band edges tend to smaller (larger) k_x below (above) the emission line. The cyan curves in Figure 6.5b are the loss-gain compensation boundaries ($\mathrm{Im}(\Lambda) = 0$), which intersect the band edges. From equation 6.2 we know that

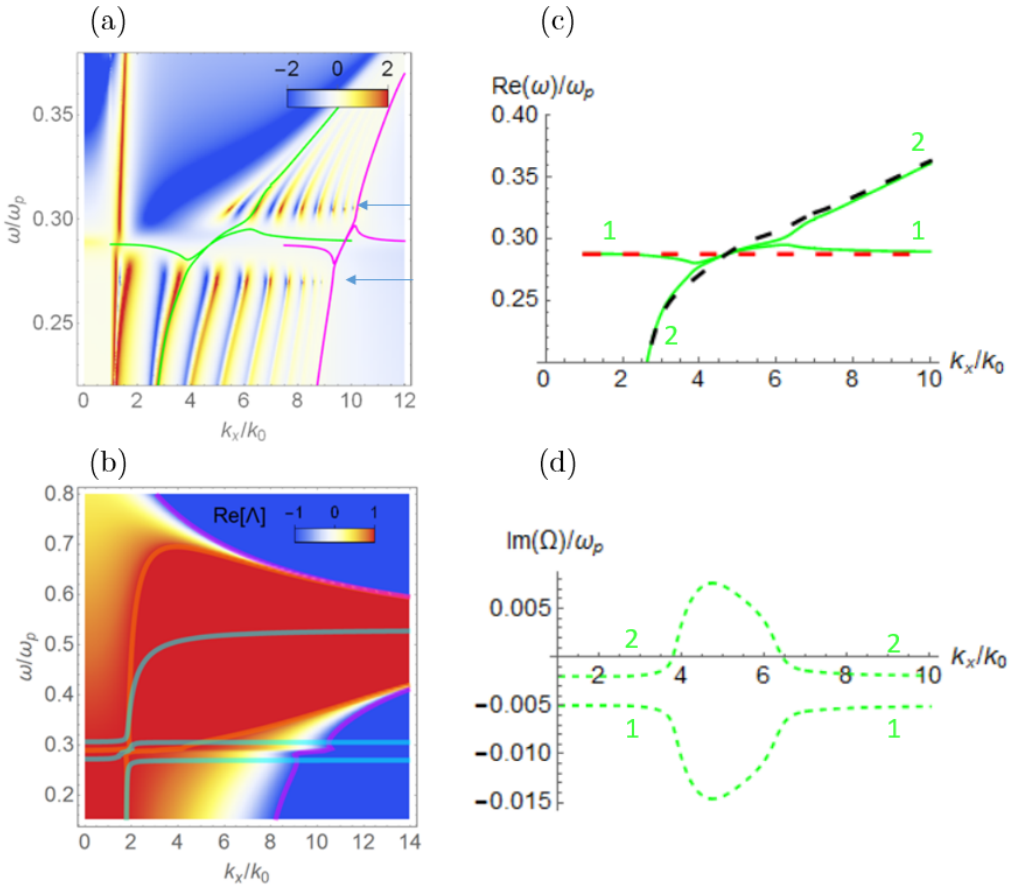

Figure 6.5: (a) Reflectance with an emission line in the large coupling strength regime ($g_e = 10^{14}$) for the finite structure (logarithmic scale). The green and magenta curves obtained via our semi-classical model on two different modes. (b) Dispersion diagram of the infinite structure with an emission line in the large coupling strength regime. Orange curves are the edges of the plasmonic band at the center of the Brillouin zone ($\mathrm{Re}(\Lambda) = 1$), magenta curves at the edge of the Brillouin zone ($\mathrm{Re}(\Lambda) = -1$) and cyan curves are the loss-compensation boundary ($\mathrm{Im}(\Lambda) = 0$). (c) Real (green solid curves) and (d) imaginary (green dashed curves) parts of the complex eigenfrequencies $\Omega_\pm$ obtained with our semi-classical model. In (c) the red dashed curve is the excitonic emission line and the black dashed curve is the unperturbed optical mode. The two polaritons resulting from the coupling of the optical mode with the excitonic line are identified by the green numbers 1 and 2 (Ω_+ and $\Omega-$, respectively.

here the condition for the generation of exceptional points is met. True exceptional points thus appear in the case of an infinite multilayer, as discussed in more detail in the next section.

6.3.3 Four-level dyes: strong gain-loss interaction

We introduce the full four-level dispersion of pumped dye molecules, including both the absorption and emission line. We will see that loss compensation and the ap-

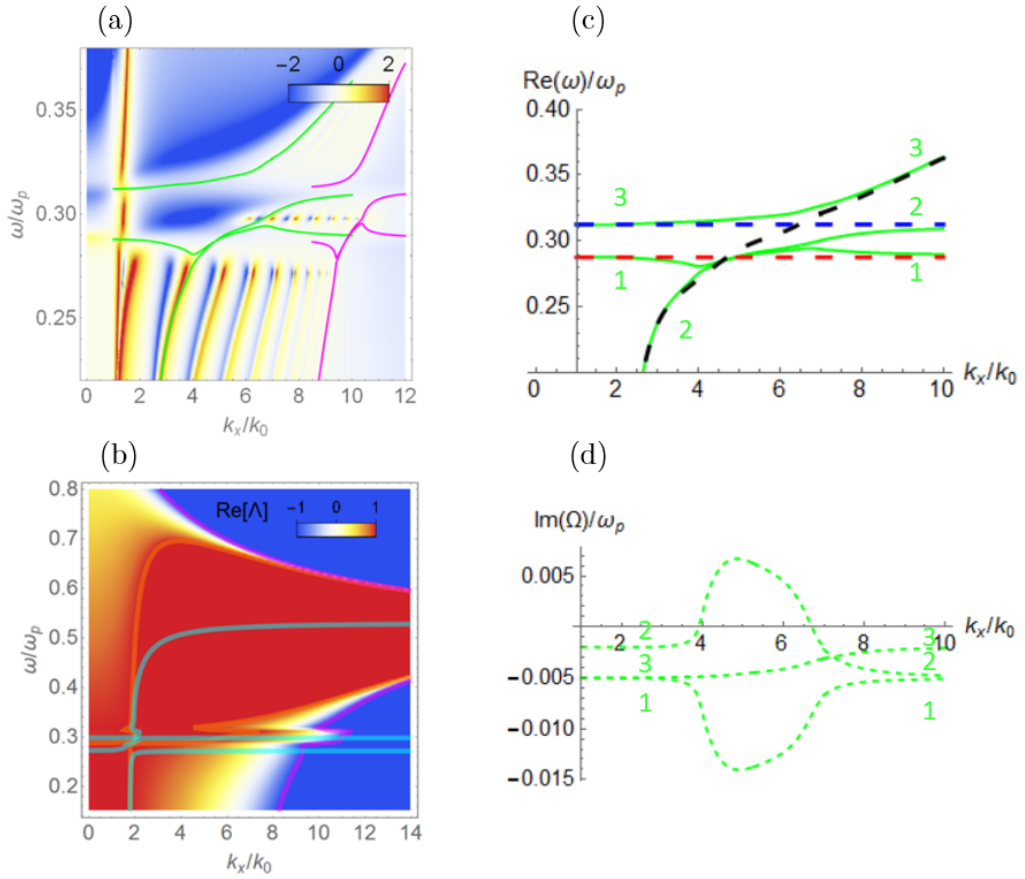

Figure 6.6: (a) Reflectance with both absorption and emission in the large coupling strength regime ($g = 10^{14}$) for the finite structure (logarithmic scale). The green and magenta curves are obtained via our semi-classical model on two different modes. (b) Dispersion diagram of the infinite structure with both absorption and emission lines in the large coupling strength regime. Orange curves are the edges of the plasmonic band at the center of the Brillouin zone ($\mathrm{Re}(\Lambda) = 1$), magenta curves at the edge of the Brillouin zone ($\mathrm{Re}(\Lambda) = -1$) and cyan curves are the loss-compensation boundary ($\mathrm{Im}(\Lambda) = 0$). (c) Real (green solid curves) and (d) imaginary (green dashed curves) parts of the complex eigenfrequencies $\tilde{\Omega}$ obtained with our semi-classical model. In (c) the red dashed curve is the excitonic emission line, the blue dashed curve is the excitonic absorption line and the black dashed curve is the unperturbed optical mode. The three polaritons resulting from the coupling of the optical mode with the two excitonic lines are identified by the green numbers 1, 2 and 3.

pearance of exceptional points are directly connected.

Figure 6.6a shows the reflectance map obtained with the transfer-matrix method of the finite structure for large coupling strengths $g = g_a = g_e = 10^{14}$. As before, the maxima of reflectance are discrete modes, and we apply the full semi-classical model Eq. 6.9 for two optical modes (green and magenta) to obtain the polaritons. Zoom-ins on the splitting behaviour with the model are provided by Figures 6.6c and 6.6d.

The blurry regions (around 0.28-0.29 ω_p and 0.31-0.32 ω_p) occur when the mag-

nitude of the imaginary part of the eigenfrequencies becomes large, while regions where discrete modes are visible have very small imaginary parts (Figure 6.6d). At the absorption line (blue curve in Figure 6.6c) the typical mode-splitting occurs, while at the emission line (red curve in Figure 6.6c) the fork-like features of $\mathcal{PT}$ systems are present (Figure 6.6c). In the region between the two excitonic lines (between ω_e and ω_a) the modes tend towards large k_x and can reach extremely high values of the effective index (for example, the bifurcation point of the green mode around $\omega = 0.3\,\omega_p$ in Figure 6.6c has an effective index of 7, while at this frequency the effective index was 4 in the passive HMM). Only the dispersion of polaritons 3 and 2 (for small k_x and in the vicinity of the gain/loss compensation points) can be observed in Figure 6.6a, because of their small (in magnitude) imaginary parts of their eigenfrequencies. Polariton 1 cannot be observed as it is always overdamped (Figure 6.6d).

As discussed previously, the emission and absorption lines exert a similar effect on the band edges of the infinite HMM. In this case the forks at the edges provide real EPs, unlike the points in the dispersion diagram of the finite structure where a vanishing imaginary part produces just lines of sharp resonances. In Figure 6.6b (the real part of Λ of the infinite HMM) an important distortion is observed around ω_e and ω_a, where the band edges ($\mathrm{Re}(\Lambda) = +1$, orange curves, and $\mathrm{Re}(\Lambda) = -1$, magenta curves) undergo a distortion similar to the resonances of the finite stack. The cyan curves in Figure 6.6b are the loss-gain compensation boundaries, which intersect the band edges. At these intersections $\Lambda = \pm 1$, so from equation 6.2 one concludes that the eigenvalues are degenerate, and that these points are thus EPs.

The presence of EPs has significant implications in the infinite structure, e.g. on the group index (along z) $n_{g,z}$ (calculated using the implicit function theorem [131]), see Figure 6.7.

Five EPs exist with the chosen parameters. Zoom-ins on two EPs (EP1 and EP2, one on each band edge) are also shown in Figures 6.8a and 6.8b, providing evidence that $n_{g,z}$ diverges, which is a signature of the existence of exceptional points, connecting with recent results in [70]. These singularities were also studied recently by Pick *et al.* [67].

Note that there is a very direct connection in position (in the (k_x, ω) dispersion coordinates) between the EPs of the infinite and the finite multilayer. For the finite structure one compares with the two 'lines of points' in Figure 6.6a ($\omega = 0.275\,\omega_p$ and $\omega = 0.3\,\omega_p$), but only with the points at the smallest and largest k_x for each line. For instance, EP1 is visible in both Figure 6.7 and Figure 6.6a at $\omega = 0.275\,\omega_p$ and $k_x/k_0 = 9$. Similarly, EP3 is both times visible at $\omega = 0.3\,\omega_p$ and $k_x/k_0 = 6$. This correspondence shows that in both cases the exceptional points arise effectively from a mechanism similar to $\mathcal{PT}$-symmetry.

6.4 Summary

In this chapter we have studied the consequence of loss compensation by the dispersive gain provided by the infiltration of emitters such as four-level organic dyes in the dielectric layer of a HMM multilayer. We developed a semi-analytical model to describe the interaction of the excitonic lines with the optical mode of the HMM

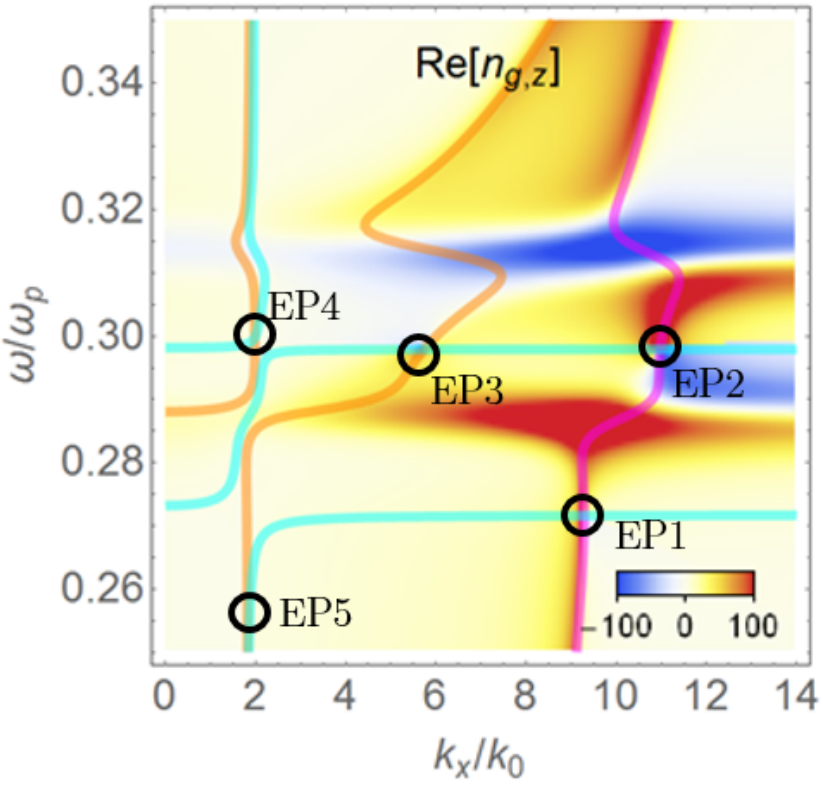

Figure 6.7: Group index in z direction $n_{g,z}$ of the dye infiltrated multilayer. Orange curves correspond to the band edges at the Brillouin zone center $k_z D = 0$, magenta curves correspond to the band edges at the Brillouin zone edge $k_z D = \pi$, and cyan curves correspond to the gain-loss compensation line where $\mathrm{Im}(\Lambda) = 0$.

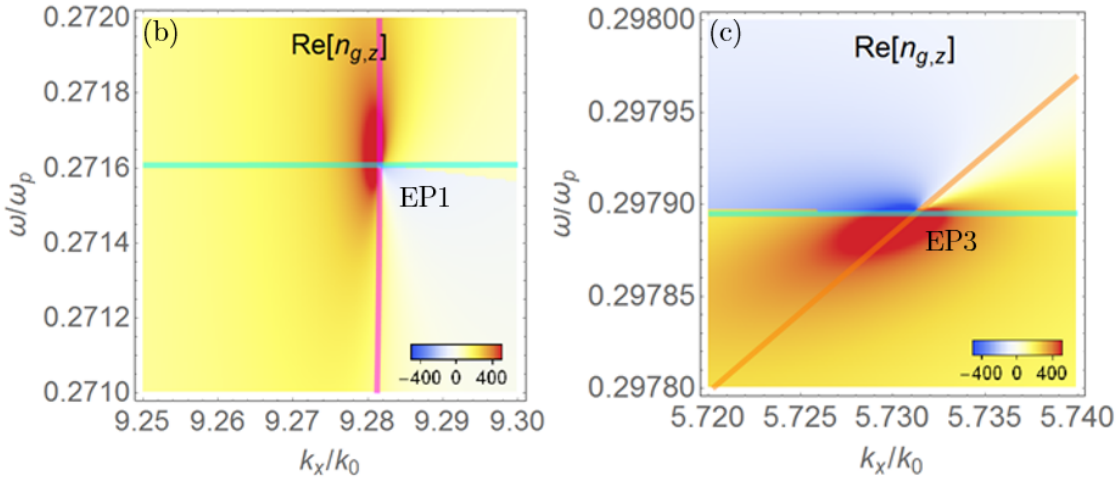

Figure 6.8: (a) Zoom on EP1 and (b) EP3 of Figure 6.7. Orange curves correspond to the band edges at the Brillouin zone center $k_z D = 0$, magenta curves correspond to the band edges at the Brillouin zone edge $k_z D = \pi$, and cyan curves correspond to the gain-loss compensation line where $\mathrm{Im}(\Lambda) = 0$.

and demonstrated that the model fits very well with the exact results obtained by the well-known transfer-matrix method.

We considered both the weak and strong coupling strength case of interaction with the emission and absorption lines, respectively. We have shown that for weak coupling strength ($|4K_aA_m| \ll |\Omega_m - \Omega_a|^2$), the interaction of both the emission and absorption line results only in a small perturbation of the optical mode and the polaritons remains either purely excitonic or either photonic.

For strong coupling strength ($|4K_aA_m| \gg |\Omega_m - \Omega_a|^2$), however, emission and absorption lines produce two different extreme distortions of the plasmonic band. For absorption, the interaction of the excitons with the optical mode leads to the typical Rabi splitting, with Rabi energy obtained directly from our semi-analytical model as $\hbar\Omega_{Rabi} = \sqrt{2K_aA_m}$.

At the emission line, a transition similar to the transition from the $\mathcal{PT}$-symmetry broken phase to the $\mathcal{PT}$-symmetry unbroken phase appears, with generation of true exceptional points at the loss-gain compensation frequencies.

Moreover, the design we proposed with the introduction of gain in HMMs also provides a convenient route to facilitate injection of light into hyperbolic modes and overcomes the problem of light incoupling, which are otherwise not directly accessible from within the light cone.

The results of this chapter are important for active components with HMMs, and for the use of exceptional points in active multilayers. Most of the work of this chapter was presented in [132].

7

Angular incidence and strong coupling in tilted cavities

In this chapter we combine the results of Chapter 5 on the extremely sharp Fano resonances in tilted HMM cavities with various concepts introduced in Chapter 6 on active HMMs. In particular we study the interaction between the Fano resonances and an excitonic line of absorption embedded in the dielectric compound of the asymmetric cavity. The energy exchange and strong coupling with Fano resonances has never been studied systematically before, to the best of our knowledge.

We first examine the angular dispersion of the Fano resonances excited in the tilted cavities described in Chapter 5, and show that the anisotropy of this medium is responsible for interesting dispersive behaviours, with excitation of different modes following the direction of propagation of light. The interference of the Fabry-Perot resonances that originate from the propagating modes and the evanescent background is physically more interesting under non-normal incidence, as the evanescent modes are not purely evanescent, but they also have a real effective index part, which differs for the two directions of energy flow. In particular, changing the wavevector parallel to the interfaces can lead either to sharper and inversed Fano resonances, or to the extinction of the Fano resonances, meaning that we have a complete control on the background effect by incidence angle.

Finally, we introduce a loss line in the cavity, and determine that the angular properties allow various intriguing phenomena linked to the strong coupling, such as enhancement of the Rabi splitting and even absorption-assisted transparency. Furthermore, the anisotropy in the direction of propagation does not change the angular dispersion and Rabi splitting, but has a deep impact on the amplitude of the absorbance peaks.

In Section 7.1 we describe the angular dispersive properties of the asymmetric cavity in the lossless case. Next, we examine in Section 7.2 the interaction of the Fano resonances with an excitonic line of absorption, and describe the anisotropic effects. We finally conclude in Section 7.3.

7.1 Angular dispersion

We discussed in Chapter 5 the origins of the Fano resonances in tilted cavities (Figure 5.1). They originate from the interference between the Fabry-Perot effect (created by the round-trips of a propagating mode) and a slowly varying background (via a purely evanescent mode). The excitation of these two modes is directly connected to the conservation of the momentum (Equation 5.11) in the transverse direction y (see Figure 5.1 of Chapter 5 for notations). For non-normal incidence ($k_y \neq 0$), however, both Fabry-Perot resonances and the background still exist but are intrinsically different. In fact, the transverse momentum conservations at the interfaces between the HMM and the AHM are:

$$\mathrm{Re}(k_y) = \mathrm{Re}(k'_x)\sin\theta + \mathrm{Re}(k'_y)\cos\theta \tag{7.1}$$

$$\mathrm{Im}(k_y) = \mathrm{Im}(k'_x)\sin\theta + \mathrm{Im}(k'_y)\cos\theta = 0 \tag{7.2}$$

with k'_x and k'_y the wavevectors in the natural axis coordinates of the tilted cavity. For these coordinates, Equation 2.31 is valid and is expressed as:

$$\begin{aligned}\cos(k'_y D\cos\theta) = &\frac{(\kappa'_d\varepsilon_m + \kappa'_m\varepsilon_d)^2}{4\kappa'_d\kappa'_m\varepsilon_d\varepsilon_m}\cosh(\kappa'_d d_d\cos\theta + \kappa'_m d_m\cos\theta)\\ &- \frac{(\kappa'_d\varepsilon_m - \kappa'_m\varepsilon_d)^2}{4\kappa'_d\kappa'_m\varepsilon_d\varepsilon_m}\cosh(\kappa'_d d_d\cos\theta - \kappa'_m d_m\cos\theta)\end{aligned} \tag{7.3}$$

with d_d the dielectric thickness in the surrounding HMMs, d_m the metal thickness, D the period, κ_d and κ_m the plasmonic decay coefficients in the dielectric and metal, respectively. We state that Equation 7.2 is equal to zero because we excite the cavity from the left with a purely real transverse momentum k_y. In this chapter, we use a lossless Drude model for silver, with thickness of the silver layers $d_m = 10$ nm and for TiO_2 $d_d = 20$ nm. The optical parameters are the same as in Chapter 5. Finally, in order to have sharper Fano resonances, we choose a geometric tilting angle of the cavity layers $\theta = 55°$ (see Figure 5.1 for graphic representation of this angle).

By solving Equations 7.3, 7.1 and 7.2 numerically in the (k'_x, k'_y) coordinates and using a coordinate transformation to express the solution in the (k_x, k_y) coordinates, we note that anisotropy of the cavity plays an important role, as it leads to the excitation of modes with different k_x momenta depending on the energy flow

direction (meaning the orientation of the period-integrated Poynting vector in the x direction). Indeed, there are two different solutions (as seen in Figure 7.1) for propagating modes (purely real momentum), but only one is excited at a time because of causality. In particular, light propagating from left to right (Figure 7.1a) has to have energy flow towards the positive direction while light propagating from right to left (Figure 7.1b) needs an energy flow towards negative direction. Since the effective index of the propagating mode is different in the two directions of energy flow, for a round-trip, the phase accumulated during the propagation in one way is not the same than in the other one. Moreover, the angular dispersion of both modes is completely different, with the mode linked to energy flow from left to right having decreasing effective index with increasing k_y momentum, and vice versa for the other direction.

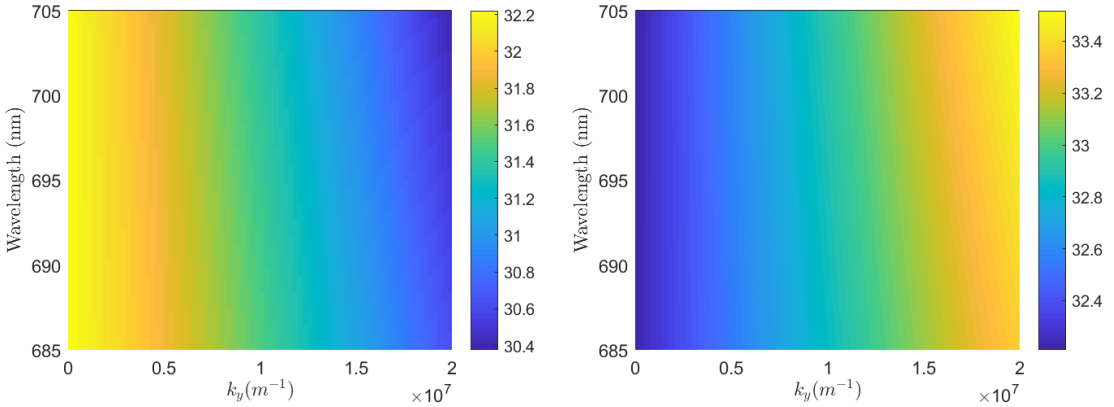

(a) From left to right

(b) From right to left

Figure 7.1: Angular dispersion of the real part of the effective refractive index in x direction of the propagating mode for an asymmetric tilted cavity with tilting angle $\theta = 55°$: (a) from left to right. (b) From right to left.

Figure 7.2 shows the reflectance map obtained with exact calculation as a function of the k_y momentum for a cavity width $B = 34.75$ nm. Because of the particular anisotropic behaviour of the cavity, Equation 5.15 is no longer usable, since determining the Fresnel coefficients of reflection and transmission at each interface without an exact homogenization theory is impossible[133]. However, Equation 5.16 governing the constructive interference of the Fabry-Perot resonances is still valid but should be replaced (to take care of the two different propagating modes) by:

$$[k_{x,r}(k_y) + k_{x,l}(k_y)]\, B + 2\varphi(k_y) = 2\pi m \tag{7.4}$$

with m an integer, $k_{x,r}$ and $k_{x,l}$ the momentum of the propagating mode with energy flow to the right and to the left, respectively, 2φ the phase change at the interfaces and B the cavity width. Using the effective index obtained in Figure 7.1 with Equation 7.4, we fit the constructive interference zone, showing a good correspondence with the exact calculation. The inset of Figure 7.2 shows the fitted value of the reflection phase change at the interfaces. This phase has a minor contribution on the constructive interference regime, but has to be taken into account to have a perfect fit.

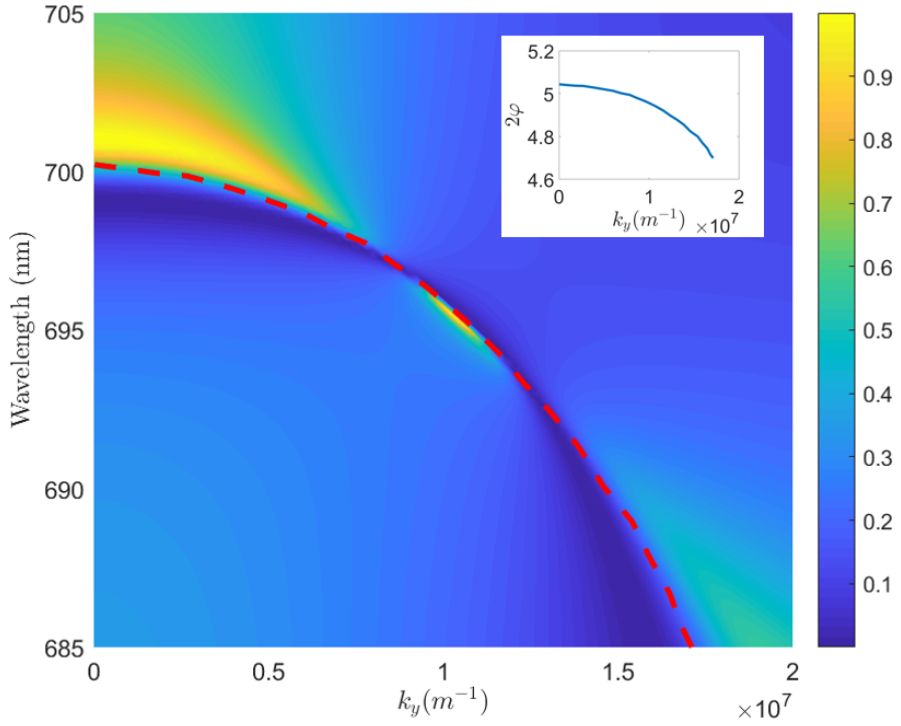

Figure 7.2: Angular dispersion of the reflectance for a cavity width $B = 34.75$ nm. Red dashed curve is the constructive interference regime obtained with Equation 7.4 with $m = 4$. Inset shows the fitted angular dispersion of the reflection phase φ.

We remark immediately in Figure 7.2 that angular incidence has a deep impact not only on the peak position, but also on the shape and amplitude of the Fano resonances. This is also clearly seen in Figure 7.3 with the reflectance spectra of the cavity for various incident k_y momenta. Increasing the k_y momentum leads to a diminution of the amplitude of the Fano resonances as shown by the blue, red and yellow curves in Figure 7.3. At $k_y = 1.025 \times 10^7\, m^{-1}$, the situation is completely different with the Fano reflectance reaching again 100%, but with opposite Fano parameter q (see Equation 3.15) with respect to the situation at $k_y = 0$ (the reflectance goes from 100 to 0% instead of 0 to 100%) and a much sharper resonance.

This evolution in the amplitude and asymmetry of the Fano resonances is explained by the different nature of the slowly varying background. As mentioned before, there is no pure evanescent mode that fulfills momentum conservation (Equations 7.1 and 7.2) as it was the case at normal incidence ($k_y = 0$). However, there are complex solutions (k'_x, k'_y) to the exact dispersion relation (Equation 7.3) that fulfill the transverse momentum conservation. Again, there is an anisotropic behaviour of these complex modes, with the mode with exponential decrease of the field from left to right equal to the opposite of the complex conjugate of the mode with exponential decrease from right to left, or:

$$n_{c,r} = -n^*_{c,l} \tag{7.5}$$

with $n_{c,r}$ and $n_{c,l}$ the complex mode refractive index with exponential decrease from left to right and right to left, respectively. Figure 7.4 shows the angular dispersion

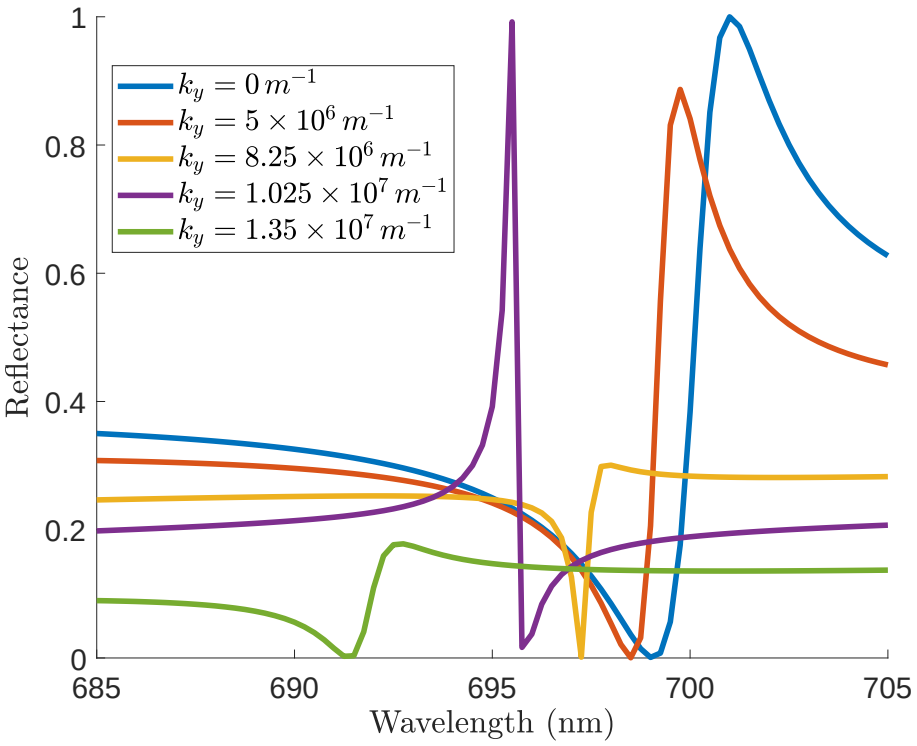

Figure 7.3: Reflectance spectra for various k_y momenta ranging from 0 to $1.35 \times 10^7\ m^{-1}$, for a cavity width $B = 34.75$ nm.

of these two complex modes.

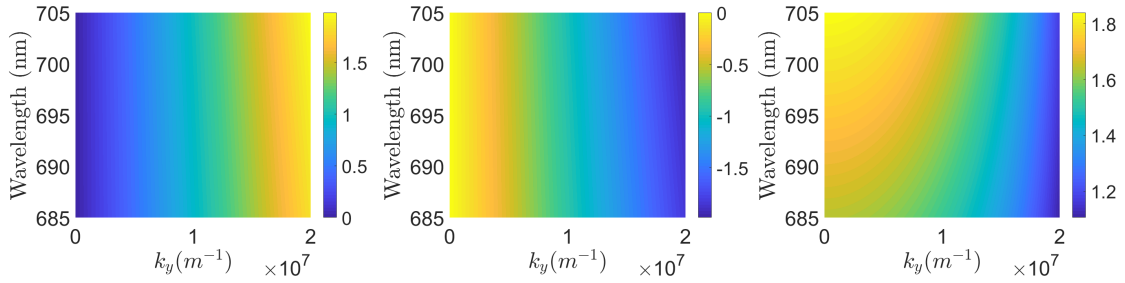

Figure 7.4: Angular dispersion of the real and imaginary part of the effective refractive index in x direction of the complex mode for an asymmetric tilted cavity with tilting angle $\theta = 55°$: (a) real part of the refractive index of the complex mode with exponential decrease from left to right. (b) Real part of the refractive index of the complex mode with exponential decrease from right to left. (c) Imaginary part of both complex modes.

A clear difference caused by this new type of background is observed for instance in reflectance spectra with variation of the cavity size (Figure 7.5). The width dispersion of the point with extremely sharp Fano resonances (bright spot in Figure 7.2, $k_y = 1.025 \times 10^7\,m^{-1}$ and $\lambda_0 = 695.5$ nm) shows that only the resonances with

even order undergo complete resonance from 0 to 100% (Figure 7.5a). Odd order resonances mainly follow the background. Note that we had already discussed the effect of the order of the resonance on the sharpness of the peaks for the graphene multilayer under normal incidence. In the non-normal incidence case, the order has an effect not only on the linewidth of the peaks but also on their amplitude.

Another example of the different physical effect of the complex mode background is given in Figure 7.5b, where the reflectance just follows the background without complete 0 to 100% variation as before, for any size of the cavity (for $k_y = 8.5 \times 10^6\, m^{-1}$ and $\lambda_0 = 697$ nm). The latter means that the coupling to the continuum background is very weak, and so the Fano parameter $q \to \pm\infty$.

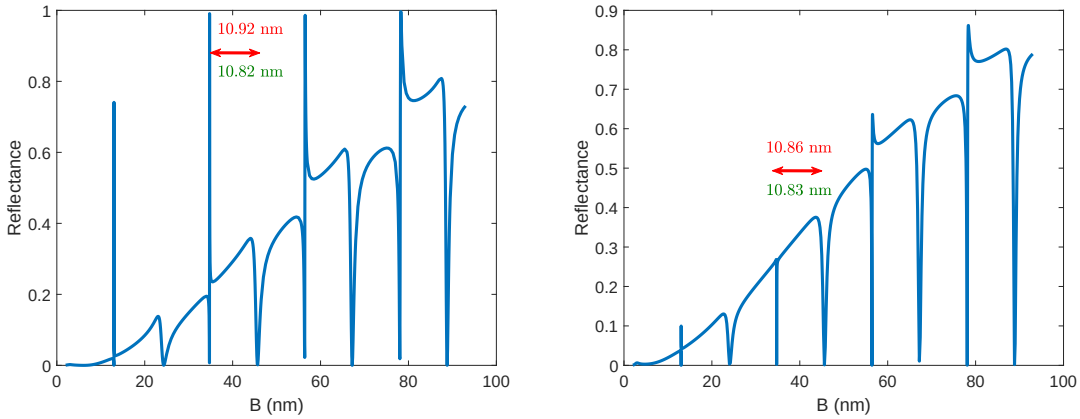

(a) $k_y = 1.025 \times 10^7\, m^{-1}$ and $\lambda_0 = 695.5$ nm (b) $k_y = 8.5 \times 10^6\, m^{-1}$ and $\lambda_0 = 697$ nm

Figure 7.5: Influence of the cavity width on the exact reflectance of a cavity with tilting angle $\theta = 55°$. (a) For $k_y = 1.025 \times 10^7\, m^{-1}$ and $\lambda_0 = 695.5$ nm and (b) for $k_y = 8.5 \times 10^6\, m^{-1}$ and $\lambda_0 = 697$ nm. Red arrows show the distance between two successive resonances, red values correspond to the measured distance, while green values correspond to the theoretical distance.

Note that we limit ourselves to a small range of wavelength and momentum. The underlying reason of this restriction is that for larger momenta, we exit the single mode cavity regime (meaning only one propagating mode in a given direction) and the analysis becomes more complicated. Figure 7.6 shows just for curiosity what the reflectance map of wider multimodal cavity ($B = 121.7$ nm) looks like for larger wavelength and momentum range.

In the next section, we take advantage of the peculiar angular behaviour to control the strong coupling between these asymmetric resonances and the absorption line of an exciton.

7.2 Fano-exciton strong coupling

We now introduce an excitonic absorption line in the tilted cavity. The situation is similar to Chapter 6, we infiltrate the dielectric compound of the AHM cavity with

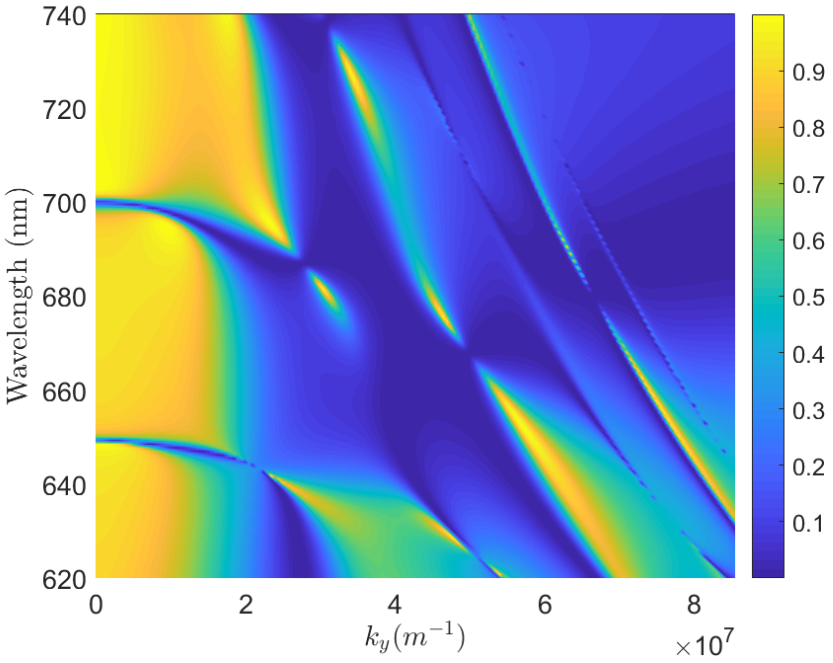

Figure 7.6: Angular dispersion of the reflectance for a cavity width $B = 121.7$ nm. Above around $k_y = 2 \times 10^7\ m^{-1}$, the cavity becomes multimodal.

two-level dyes, leading to a dielectric permittivy simlar to Equation 6.4:

$$\varepsilon_{\mathrm{TiO_2}} = 7.29 + g_a L(\omega_a, \gamma_a) \tag{7.6}$$

with $L(\omega_j, \gamma_j) = -\frac{1}{\pi}\frac{2\omega_j}{(\omega^2-\omega_j^2-\gamma_j^2)+2i\gamma_j\omega}$ the normalized second-order Lorentzian lineshape function, $g_a = 10^{14}$ the oscillator coupling strength, $\gamma_a = 0.001\omega_p$ the linewidth (with $\omega_p = 1.26 \times 10^{16}$ rad/s the plasma frequency of silver) and ω_a the peak frequency of the excitonic line.

We divide this section in three parts. The first part describes the interaction between the excitonic line and different types of Fano resonances at normal incidence. The second part examines the influence of the background on the Rabi splitting, and the apparition of absorption-enduced transparency in the non-normal incidence case (described in the previous section). The last part takes care of the asymmetry in the y direction that appears due to the loss.

7.2.1 Normal incidence

At normal incidence, there are three different limiting cases of Fano resonances (see Chapter 5). The first case is when the cavity is so small that the resonance peak is just a peak of reflectance (dashed blue curve in Figure 7.7a), the second case is the typical asymmetric Fano resonance (dashed blue curve in Figure 7.7b), and the third case is when the cavity is so large that the background vanishes and the resonance is almost entirely a Fabry-Perot resonance (reflectance dip, dashed blue curve in Figure 7.7c). In all cases, an absorption line centered around a wavelength

of 700 nm (which is the resonant wavelength of the cavity) is used, so that there is no detuning between the Fano resonance and the excitonic line.

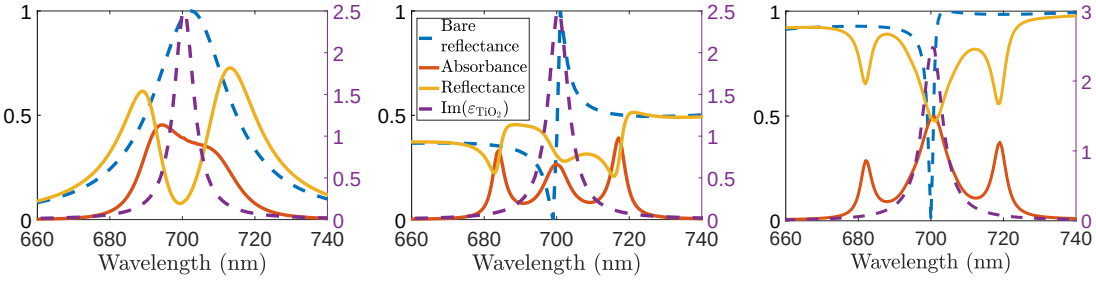

(a) $B = 2.8$ nm (b) $B = 34.75$ nm (c) $B = 121.7$ nm

Figure 7.7: Reflectance and absorbance spectra of various dye-infiltrated cavities. (a) For $B = 2.8$ nm. (b) For $B = 34.75$ nm. (c) For $B = 121.7$ nm. In the three figures, the blue dashed curve is the reflectance of the cavity without excitonic line, orange and yellow solid curves are the absorbance and reflectance of the infiltrated cavity, respectively. Dashed purple curve is the imaginary part of the permittivity of the infiltrated dielectric $\mathrm{Im}(\varepsilon_{\mathrm{TiO_2}})$, scale on the right hand side.

In the first case (small cavity width $B = 2.8$ nm), we see in Figure 7.7a that two distinct peaks of reflectance appear (yellow curve, with loss) instead of one (blue curve, without loss) with the introduction of the absorption line (purple curve). This is however not yet the strong coupling regime, as we can see via the absorbance curve (orange curve) that the coupling is not strong enough to have two distinct peaks. In other words, the Rabi splitting is smaller than the linewidth of the two absorbance peaks, which is a weak coupling signature as discussed in Chapters 3 and 6. The two peaks of reflectance correspond to the single peak of the lossless structure with a large absorption at the central frequency, which cause a dip.

However, the situation is different when the excitonic line interacts with a typical asymmetric Fano resonance (cavity width $B = 34.75$ nm), see Figure 7.7b. For the reflectance (yellow curve), three distinct asymmetric Fano resonances appear, but none of them have complete transmission or reflection. The absorbance peak around $\lambda_0 = 700$ nm (orange curve) is caused by uncoupled light due to a shift of the Fano resonance linked to the introduction of loss. Indeed, infiltration of excitons modifies the permittivity of the dielectric, causing a small detuning between the Fano resonance and the excitonic line of absorption. In this case, we are clearly in the strong coupling regime since the absorbance peaks (orange curve) are distinct, separated by a Rabi energy of about 80 meV.

The last case is the quasi-pure Fabry-Perot resonance (large cavity width $B = 121.7$ nm), which has similar features than the previous case, but it presents instead three reflectance dips and not three asymmetrical Fano resonances. Moreover, the central peak caused by the detuning is here more pronounced, wich is intuitively obvious since the cavity is larger.

7.2.2 Angular incidence

As demonstrated in Section 7.1, introducing a momentum in the y direction creates various types of Fano resonance due to a different interference between the Fabry-Perot resonances and the complex evanescent background because of anisotropy. In this section we examine the impact of this Fano type change on the strong coupling regime of the cavity.

We use the same geometry as for Figure 7.2: $\theta = 55°$, $B = 34.75$ nm. We examine the interaction of the Fano resonance with the excitonic line in two regimes. The first regime is when no detuning between the two oscillators occurs at normal incidence ($\lambda_0 = 700$ nm and $k_y = 0$, Figure 7.8a), and the second regime is when there is no detuning with the bright spot in Figure 7.2 ($\lambda_0 = 695.5$ nm and $k_y = 1.025 \times 10^7\, m^{-1}$). At this spot we thus have interaction with a Fano resonance with opposite Fano parameter (Figure 7.8b).

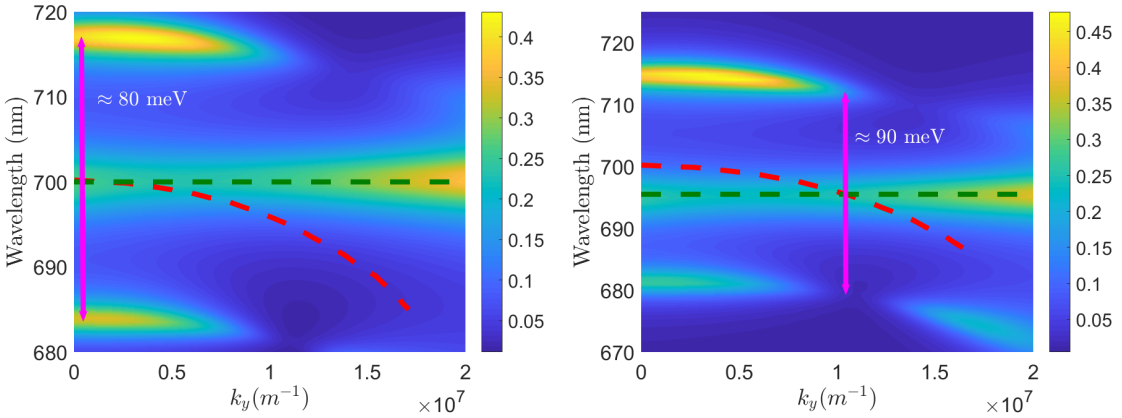

(a) Exciton centered on $\lambda_0 = 700$ nm

(b) Exciton centered on $\lambda_0 = 695.5$ nm

Figure 7.8: Angular dispersion of the cavity absorbance and strong coupling of the Fano resonance with the excitonic line centered on (a) $\lambda_0 = 700$ nm. (b) $\lambda_0 = 695.5$ nm. Red dashed curve is the Fano angular dispersion without absorption, green dashed curve is the excitonic line and magenta arrow shows the Rabi splitting where there is no detuning between the two oscillators.

First of all, one immediately notices that strong coupling is reached in both cases, since there are two distinctly separated peaks of absorbance in Figure 7.8. Note that there is also a part of the exciton that does not couple in both figures. At normal incidence, the Rabi splitting is about 80 meV while at the bright spot of Figure 7.2, the Rabi splitting is slightly enhanced to 90 meV. This difference is mainly due to the sharpening of the Fano resonance caused by the complex background, as discussed in Section 7.1.

The main difference between the two situations is however not related to the Rabi splitting, but concerning the transparency zones that appears at the k_y momentum for which there is small detuning (at the heads of the magenta arrow in Figure 7.8b). Indeed, we expected a maximum of absorbance around $k_y = 1.025 \times 10^7\, m^{-1}$ in Figure 7.8b since it is the momentum for which the detuning is about zero (similarly to the maximum of absorbance appearing at the zero-detuning zone around $k_y = 0$

in Figure7.8a). Except for the uncoupled excitonic line at $\lambda_0 = 695.5$ nm, the absorption of the coupled modes is very weak at this momentum ($k_y = 1.025 \times 10^7\, m^{-1}$), and the transmission becomes very high compared to the case without absorption. The reason of this comes simply from the refractive indices of the propagating modes in the cavity. Introducing absorption in the cavity not only leads to absorption, but also on a slight change of the refractive index. For instance, at $k_y = 1.025 \times 10^7\, m^{-1}$ and $\lambda_0 = 695.5$ nm, the real part of the refractive index of the propagating mode with energy flow from left to right changes from 31.41 to 32.11, while in the other direction from 32.9 to 33.3460. The mean refractive index of the cavity is thus increased by the introduction of loss and the Fano resonance shifts thus slightly to higher wavelength to ensure the constructive interference condition of Equation 7.4.

Because the bright spot in Figure 7.2 was surrounded by zones where the background was inefficient and the resonances were broad and small in amplitude, the crossing between the Fano resonance and the excitonic line occurs then at this inefficient zone due to the shift of the refractive index. The coupling with the excitonic line is thus very weak at this point and the absorption is large only at the peak frequency of the exciton.

7.2.3 Asymmetry in y direction

In this section we discuss the effect of the direction of the transverse k_y momentum on the strong coupling (so incidence going up or down along y, respectively). Since the structure we study is not symmetric in the y direction, the scattering properties of the cavity depend on the direction of the momentum k_y in the presence of loss. Without loss, the scattering properties are the same for positive and negative k_y, with the only variation that the mode with energy flow from left to right becomes the mode with energy flow from right to left, and inversely. From reciprocity [134] reflectance is always the same for positive or negative k_y momenta. Indeed, coupling from the input of port 1 (s_1^+) and the output of port 2 (s_2^-) is the same as the coupling from the input of port 2 (s_2^+) and the output of port 1 (s_1^-) in Figure 7.9, which illustrates our situation. Since there are no losses, transmittance is also the same for both positive (from port 1 to port 3) and negative k_y (from port 2 to port 4) excitation because of unitarity (no reciprocity however between these two transmittances).

In presence of losses, however, reciprocity ensures that the reflectance is the same for positive or negative k_y momenta, but not for transmittance, the difference arising from the absorbance. This effect is demonstrated clearly in Figure 7.10 for a cavity with an excitonic line of absorption centered at $\lambda_0 = 695.5$ nm and a cavity width $B = 34.75$ nm. As stated before, the reflectance for positive k_y (dark blue curve) is exactly the same than the one for negative k_y (red dashed curve). The asymmetry effect is however significant for the transmittance (yellow (+) and purple (-) curves) and absorbance (green (+) and light green (-) curves).

Even if the asymmetry has a very weak effect on the Rabi splitting due to the strong coupling between the two oscillators (the absorbance peaks are around 680 nm, 700 nm and 712 nm for green and light blue curves in Figure 7.10), we can

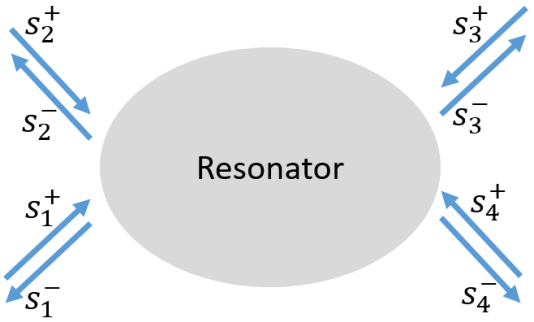

Figure 7.9: Schematic of an optical resonator system coupled with multiple ports similar to our cavity design. Arrows illustrate the incoming and outgoing waves.

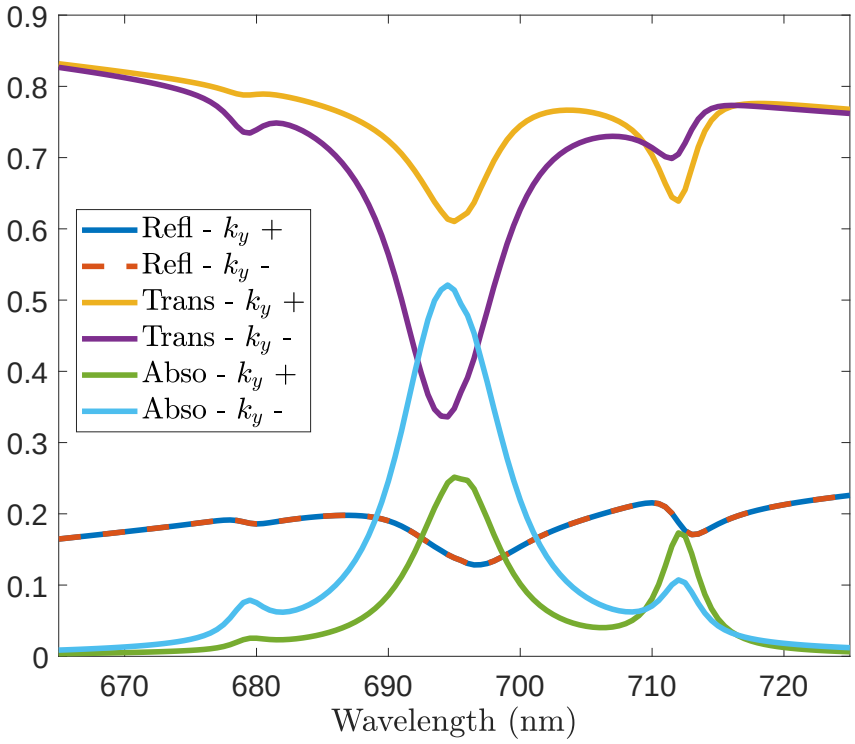

Figure 7.10: Scattering spectrum of the infiltrated cavity for $k_y = \pm 1.025 \times 10^7\, m^{-1}$. Dark blue and red dashed curves correspond to the reflectance, yellow and purple curves to the transmittance, green and light blue curves to the absorbance for the positive and negative transverse momentum k_y, respectively.

see that absorbance is different for the negative transverse momentum for each peak. Note that this phenomenon is not related to the precise k_y we use for the simulation, it applies for all k_y, see Figure 7.11. The angular dispersion is the same in both directions, because the four modes in play (two propagating and two complex modes) are the same and thus lead to the same constructive interference conditions. The only change stems from the coupling of light with these modes and this influences the field profile in the cavity, with a higher absorbance typically for

the negative k_y momenta (absorbance can however be slightly higher for positive k_y momenta around the transparency zone, as seen in Figure 7.10). Since the modes excited in the cavity are the same for the two directions, the previous discussion in Section 7.2.2 on the transparency zone still holds and explains the apparition of the transparency zone also for negative k_y (no coupling between the two oscillators) at the same magnitude of k_y.

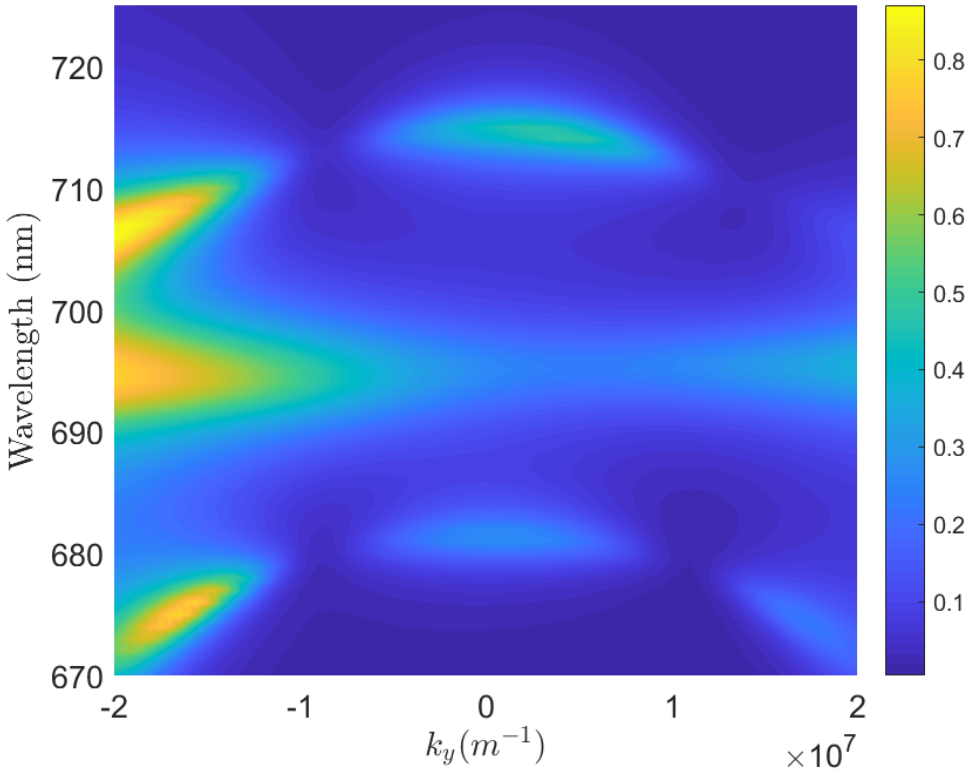

Figure 7.11: Asymmetric absorbance map of the infiltrated cavity with width $B = 34.75$ nm with respect to the direction of the transverse momentum k_y.

7.3 Conclusion

This chapter analyzed the angular dispersion of the Fano resonances introduced in Chapter 5. The interference between fast oscillating resonances and a slowly varying background still holds for non-normal incidence. We highlighted that the presence of a non-zero transverse momentum leads to anisotropy in the direction of propagation, with the mode flowing from left to right being different from the mode flowing in the other direction. Moreover, we have provided evidence that the nature of the background differs, since it originates from two different complex modes (one being the opposite and complex conjugate of the other) and not from a purely evanescent mode. This leads to interesting physical phenomena like an order-dependance of the Fabry-Perot resonances (asymmetrical 0-to-100% resonances, or an inefficiency of the background), and quasi-pure Fabry-Perot resonances.

We then combine these specificities to study their interaction with an excitonic absorption line, which was not reported yet to the best of our knowledge. We demonstrated that the Fano parameter has an influence on the Rabi splitting, and can even have a deep impact such as slowing down the exchange of energy between the two oscillators, and driving them out of the strong coupling regime. Furthermore, we highlighted the generation of absorption-assisted transparency zones, and an asymmetry in the coupling between negative and positive transverse momenta.

To conclude, one should note that an exact homogenization theory, not available to this day for these metamaterials, is required to have a complete understanding of the phenomena appearing in this chapter. Indeed, homogenization is useful to describe the Fresnel coefficients, the coupling mechanisms at the interfaces, and the energy transport of the propagating and complex modes.

8

Conclusion and outlook

Throughout this work we studied and exploited the rich properties of hyperbolic metamaterials in various fundamental structures and configurations. The high-momentum waves and extremely large photonic density of states, together with the ease of fabrication, are of crucial importance for a myriad of photonic applications, such as the hyperlens and spontaneous emission engineering. In the following we propose a concise summary of this work and discuss further opportunities.

We started in Chapter 4 with a fundamental study of the dispersive behaviour of atypical hyperbolic metamaterials, modeling a two-dimensional array of square or rectangular silver nanorods in a TiO_2 matrix. We explored four different geometrical regimes, in connection with four different mode symmetries of the plasmonic bands: small square nanorods (nanorod size much smaller than the x and y periods), large square nanorods (nanorod size on the order of the period), medium square nanorods (intermediate size), and finally, the rectangular nanorod regime (with broken symmetry between x and y). For the small nanorods the metallic corners (that are the most elementary structures in this type of design) couple to their nearest neighbors through the metal-dielectric interfaces along the same nanorod. For this reason, the dispersion relation of the plasmonic bands of the two-dimensional array of small nanorods can be seen as the interaction between all single nanorods, as could have been intuitively guessed. The situation is different for the large nanorod case, where the metallic corners are connected mainly with the corners of the adjacent nanorods,

through the dielectric medium. The dispersion relation of the metamaterials is no longer interpreted as a collective interaction of single nanorods, but as a collective coupling between all the four-corner structures of the array. Furthermore, changing the coupling between the elementary excitations also influences the modal symmetry of the modes at the significant points of the Brillouin zone. This change was also demonstrated for the medium size and rectangular nanorod studies, where we highlighted the influence of the frequency regime on the relevant elementary excitation.

Next, in Chapter 5, we explored the engineering of Fano resonances with a specific design based on the typical hyperbolic multilayer. The structure consists of a cavity surrounded by two identical HMMs, the cavity being this same HMM, but with the optical axis tilted. In this way, exciting the fundamental propagating mode at normal incidence ($k_y = 0$) of the surrounding HMM leads to the excititation of a propagating mode with extremely large effective index in the cavity, together with an evanescent mode. We have shown that the round-trips of the propagating mode in the cavity generates sharp Fabry-Perot resonances, even for extremely compact cavities as small as 5 nm in the visible regime, while a slow increase of the reflection is observed due to the evanescent mode. The interference of these two distinct processes leads to the generation of highly asymmetric Fano resonances with extreme variations of the scattering behaviour of the cavity, as the reflectance goes from 0 to 100% by changing the wavelength or cavity width over only a few nanometers. This extreme sensitivity could be very useful in the specific domain of sensing for example. This mechanism is fairly general, and also works in other regimes such as the terahertz range, which we prove using graphene-based multilayers. In particular, we shown cavities as small as 0.5 μm, with a wavelength in free-space of 100 μm, together with an extreme tuning of the scattering properties with the graphene doping level. A variation of only a few percent of electron-volt changes completely the position and finesse of these Fano resonances. Finally, we discussed that ohmic losses have a deep impact on the robustness of the Fano resonances, as many are cancelled out without a careful preliminary study of the ideal geometric parameters of the asymmetric cavity.

In Chapter 6 we further address this loss issue, using dispersive four-level dyes to overcome the ohmic loss in hyperbolic multilayers. We started from the theory of passive HMMs to properly design our structure, so that pumping of the dyes and population inversion could be possible, without requiring gratings or other incoupling systems to couple with the high-momentum waves. Rather, by smartly adjusting the intersection point between the two plasmonic bands, we numerically demonstrated that pumping of the dyes is possible inside the light cone, which makes our structure easier to fabricate. We developed a semi-classical model to describe the interaction of excitonic lines with the HMM modes. An important parameter is the coupling strength of the excitonic line with light. Therefore we explored two distinct regimes, one regime where the coupling constant is weak (the weak coupling or perturbative regime), and one where the coupling constant is large (the strong coupling strength regime). In the weak coupling regime both absorption and emission lines exert a similar weak perturbation of the mode. In the strong coupling strength regime, however, absorption and emission lines have completely distinct behaviours. At the absorption line the interaction leads to a coherent exchance of energy, and to

a Rabi splitting of the hyperbolic modes into two new polaritons. Our model allows to analytically determine the Rabi energy of the coupling, which is usually not possible with typical models found in the literature. On the other hand, the emission line exerts a different distorsion of the plasmonic mode as we observed a 'fork-like' feature, similar to what is observed in $\mathcal{PT}$-symmetric systems. These results were in very good agreement with exact calculations using the transfer-matrix method. Surprisingly, even if our active multilayer is not properly $\mathcal{PT}$-symmetric, we proved both analytically and numerically that exceptional points exist in an infinite stack at the intersection between the plasmonic band edges and the gain-loss compensation boundaries.

Chapter 7 combines the two previous chapters and studies the interaction of Fano resonances with excitonic absorption lines, which has never been done to the best of our knowledge. Since strong coupling is typically demonstrated through the angular dispersive behaviour of the polaritons, we started with the transverse momentum dispersion of the Fano resonances in the tilted cavities. From an analytical examination of the dispersion relation of the HMMs, together with the conservation of the transverse momentum at the interfaces of the tilted cavity, we demonstrate (for non-normal incidence) an anisotropy of the excited propagating modes dependent on their Poynting vector directions. The slowly varying background, generated at normal incidence by a purely evanescent mode, is replaced by a background of two complex modes, that is also linked to the cavity anisotropy. The varying nature of the underlying processes leads to a control, through the Fano parameter, of the shape and amplitude of the resonances, in particular through the generation of extremely sharp peaks, with opposite asymmetry to the one obtained at normal incidence. We then examined the interaction of an excitonic absorption line with various Fano resonances, and demonstrated the influence of the Fano parameter on the strong coupling regime and the Rabi splitting. Moreover, we discussed the generation of an absorption-induced transparency zone for certain transverse momenta and anisotropic absorbances of the cavity.

As we have seen throughout this thesis, the scope of applications of HMMs is very wide, and is mainly limited by the ohmic losses of metals, like for many other plasmonic devices. Indeed, the optical properties of gold and silver are not suitable anymore for the extreme confinement of the electromagnetic fields towards which photonics is moving. But that is not the only problem of these noble metals, as they are also hardly tunable, expensive, and not CMOS-compatible, in addition to having bad mechanical properties. Graphene sheets (explored in Chapter 5) are an alternative to the typical metals, but they have the disadvantage to support plasmon polaritons only in the terahertz regime, and they are hard to integrate in multilayer configurations. New plasmonic platforms are thus actively explored nowadays, for example by the Boltasseva group (Purdue University) [135–137]. Alternatives to silver and gold are for instance dilute metals (metals with reduced carrier concentration and thus loss), transparent conducting oxides like ITO or heavily-doped ZnO, two-dimensional semiconductors such as MoS_2, and metal nitrides like titanium nitride (TiN). Unfortunately, to this day the optical properties of such materials are either not satisfactory, or their fabrication and deposition are not mastered or too expensive. Another direction of development for HMMs, from the point-of-view of

integration in smart devices, is the scaling of their period down to the nanometer range. However, this leads naturally into the quantum domain with unprecedented phenomena. Scaling down the metallic layers also decreases the mean-free path of the carriers, and thus inceases the losses. Again, this will not be possible until new plasmonic alternatives are available. For these reasons, when low-loss plasmonic materials are discovered and produced at a large scale, the field of hyperbolic metamaterials should experience a new golden age.

Appendices

A

Exciton coupling in 1D periodic system

A.1 Field amplitude equation

The wave equation for the electric field reads

$$\frac{1}{c^2}\partial_t^2\mathbf{E} = -\nabla\times\nabla\times\mathbf{E} - \mu_0\partial_t^2\mathbf{P} \tag{A.1}$$

For TM polarised waves in a one dimensional system $\mathbf{H} = (0, H_y, 0)$ and $\mathbf{E} = (E_x, 0, E_z)$ Eq. (A.1) then becomes

$$\frac{1}{c^2}\partial_t^2\mathbf{E} = \partial_z^2\mathbf{E} - \partial_x\partial_z\mathbf{E} - \mu_0\partial_t^2\mathbf{P}, \tag{A.2}$$

where $\mathbf{P} = \mathbf{P}[\mathbf{E}]$ captures the dynamic polarization response of all dispersive materials, e.g. the metal and the gain layers. For a periodic system of metal and dielectric layers we split the polarization into two parts $\mathbf{P}[\mathbf{E}] = \Theta^{(m)}(z)\mathbf{P}^{(m)}[\mathbf{E}] + \Theta^{(g)}(z)\mathbf{P}^{(g)}[\mathbf{E}]$ with geometry factors $\Theta^{(g/m)}(z)$ that are 1 inside the respective layer and 0 otherwise. Let us assume that $\mathbf{u}_j(z,t) = \hat{\mathbf{u}}_j(z)e^{-i\Omega_j t}$ are solutions of the passive system, i.e. for $\mathbf{P}^{(g)} = 0$. The normal modes $\mathbf{u}_j$ form a complete basis and solve

$$-\frac{\Omega_j^2}{c^2}\mathbf{u}_j = \partial_z^2\mathbf{u}_j - \partial_x\partial_z\mathbf{u}_j - \mu_0\Theta^{(m)}(z)\partial_t^2\mathbf{P}^{(m)}[\mathbf{u}_j] \tag{A.3}$$

Next we consider the system with gain. With the introduction of gain the (cold cavity) system becomes pertubed. We can still expand the electric field in terms of the unperturbed eigenmodes, i.e.,

$$\mathbf{E}(t) = \sum_j \hat{E}_j(t)\mathbf{u}_j(z,t) \tag{A.4}$$

where $\hat{E}_j(t)$ are now time-dependent amplitudes that are slowly varying in time. We insert the ansatz for the electric field into Eq. (A.2). Assuming that the polarization responses are linear and isotropic we obtain,

$$\sum_j 2i\frac{\Omega_i}{c^2}\mathbf{u}_j\partial_t\hat{E}_j(t) \approx \mu_0\sum_j \Omega_j^2\Theta^{(g)}(z)\mathbf{u}_j P^{(g)}[\hat{E}_j(t)e^{-i\Omega_j t}] \tag{A.5}$$

For the derivation of this equation we made use of Eq. (A.3) for the passive structure and the slowly-varying envelope approximation,

$$\begin{aligned}\partial_t^2(\hat{E}_j(t)\mathbf{u}_j(z,t)) &= -\Omega_j^2\mathbf{u}_j(z,t)\hat{E}_j(t) - 2i\Omega_j\mathbf{u}_j(z,t)\partial_t\hat{E}_j(t) + \mathbf{u}_j(z,t)\partial_t^2\hat{E}_j(t)\\ &\approx -\Omega_j^2\mathbf{u}_j(z,t)\hat{E}_j(t) - 2i\Omega_j\mathbf{u}_j(z,t)\partial_t\hat{E}_j(t)\end{aligned} \tag{A.6}$$

and approximated the time-derivative of the polarization by $\partial_t^2 P^{(g)}[E_j(t)e^{-i\Omega_j t}] \approx -\Omega_j^2 P^{(g)}[E_j(t)e^{-i\Omega_j t}]$. In a last step we project Eq. (A.5) onto the normal modes $\mathbf{v}_i$ associated with the adjoint (left-handed) eigenvalue problem. Using $\langle\mathbf{v}_i,\mathbf{u}_j\rangle = \delta_{ij}$ yields

$$2i\frac{\Omega_i}{c^2}e^{-i\Omega_i t}\partial_t\hat{E}_i(t) \approx \mu_0\sum_j \omega_j^2\Gamma_{ij}P^{(g)}[\hat{E}_j(t)e^{-i\Omega_j t}] \tag{A.7}$$

where

$$\Gamma_{ij} = \langle\mathbf{v}_i, \Theta^{(g)}(z)\mathbf{u}_j\rangle \tag{A.8}$$

is the confinement factor. Generally, the gain medium will couple the various modes due to the spatial rectification. If the perturbation induced by the gain medium is sufficiently small, however, we can assume that $\Gamma_{ij} \approx 0$ for $i \neq j$. In this case Eq. (A.7) reduces to

$$e^{-i\Omega_i t}\partial_t\hat{E}_i(t) \approx -\frac{i\Omega_i}{2\varepsilon_0}\Gamma_i P^{(g)}[\hat{E}_i(t)e^{-i\Omega_i t}] \tag{A.9}$$

where $\Gamma_i = \Gamma_{ii}$. We rewrite this equation in terms of the fast amplitudes $E_i = \hat{E}_i e^{-i\Omega_i t}$ and define $P_i = P^{(g)}[E_i]$ for convenience. This gives the final result

$$\partial_t E_i = -i\Omega_i E_i - \frac{i\Omega_i}{2\varepsilon_0}\Gamma_i P_i \tag{A.10}$$

A.2 Maxwell-Bloch equations

The Maxwell-Bloch equation for the polarization of a two-level system is

$$\partial_t \rho_{12} = -i\Omega_{12}\rho_{12} - ig(\rho_{22} - \rho_{11}) \tag{A.11}$$

where ρ_{ij} are the elements of the density matrix of the two-level system, and $\rho_{21} = \rho_{12}^*$. When including dephasing the transition frequency Ω_{12} becomes complex, i.e. $\Omega_{12} = \omega_{12} - i\gamma_{12}$ where γ_{12} is the dephasing rate. The Rabi frequency $g = \boldsymbol{\mu}_{12} \cdot \mathbf{E}/\hbar$ depends on $\boldsymbol{\mu}_{12}$, the dipole matrix element. An equation for the (complex) macroscopic polarization is obtained from Eq. (A.11) by taking the volume average $\mathbf{P} = N\boldsymbol{\mu}_{12}\rho_{12}$,

$$\partial_t \mathbf{P} = -\Omega_{12}\mathbf{P} - i\frac{\boldsymbol{\mu}_{12}(\boldsymbol{\mu}_{12} \cdot \mathbf{E})}{\hbar}(N_2 - N_1) \tag{A.12}$$

with N, $N_1 = N\rho_{11}$ and $N_2 = N\rho_{22}$ the density of two-level systems, the density of atoms in the ground state and the density of atoms in the excited states, respectively.

Considering isotropicaly oriented dipole, we can rewrite Eq. (A.12) as

$$\partial_t \mathbf{P} = -i\Omega_{12}\mathbf{P} + i\sigma_{12}\mathbf{E} \tag{A.13}$$

with

$$\sigma_{12} = -\frac{\boldsymbol{\mu}_{12}^2(N_2 - N_1)}{3\hbar} \tag{A.14}$$

the cross-section of the transition. Assuming harmonic dependency of time ($\sim e^{-i\omega t}$) and with some algebraic manipulations, we obtain

$$\mathbf{P} = \varepsilon_0\chi(\omega)\mathbf{E} = \varepsilon_0\frac{\pi\sigma_{12}}{\varepsilon_0}\left[-\frac{1}{\pi}\frac{1}{(\omega - \omega_{12}) + i\gamma_{12}}\right]\mathbf{E} = \varepsilon_0 f\mathcal{L}(\omega)\mathbf{E} \tag{A.15}$$

introducing the susceptibility $\chi(\omega)$, the coupling strength $f = \pi\sigma/\varepsilon_0$ of the oscillator and $\mathcal{L}(\omega)$ the complex Lorentzian of transition line. The corresponding causal response function produces the second order Lorentzian line-shape function

$$L(\omega) = \mathcal{L}(\omega) + \mathcal{L}^*(-\omega), \tag{A.16}$$

which has the explicit form

$$L(\omega) = -\frac{1}{\pi}\frac{2\omega_{12}}{(\omega^2 - \omega_{12}^2 - \gamma_{12}^2) + 2i\gamma_{12} * \omega} \tag{A.17}$$

A.3 Vacuum Rabi Splitting

To understand the interaction of an excitonic line with an optical mode, we combine Eqs (A.10) and (A.13) to obtain the system of coupled equations

$$\partial_t \begin{pmatrix} \mathbf{E} \\ \mathbf{P}/\varepsilon_0 \end{pmatrix} = -i\Omega_{\pm} \begin{pmatrix} \mathbf{E} \\ \mathbf{P}/\varepsilon_0 \end{pmatrix} = \begin{pmatrix} -i\Omega_m & iA_m \\ iK_{12} & -i\Omega_{12} \end{pmatrix} \begin{pmatrix} \mathbf{E} \\ \mathbf{P}/\varepsilon_0 \end{pmatrix}, \tag{A.18}$$

where Ω_m is the complex frequency of the optical mode, $A_m = \Omega_m\Gamma/2$ and $K_{12} = \sigma_{12}/\varepsilon_0$. The new complex eigenfrequencies $\Omega_{\pm}$ of the coupled system are

$$\Omega_{\pm} = \frac{1}{2}(\Omega_m + \Omega_{12}) \pm \frac{1}{2}\sqrt{4K_{12}A_m + (\Omega_m - \Omega_{12})^2}. \tag{A.19}$$

Bibliography

[1] P. D. Cunningham, N. N. Valdes, F. A. Vallejo, L. M. Hayden, B. Polishak, X.-H. Zhou, J. Luo, A. K.-Y. Jen, J. C. Williams, and R. J. Twieg, "Broadband terahertz characterization of the refractive index and absorption of some important polymeric and organic electro-optic materials," *Journ. of Appl. Phys.*, vol. 109, p. 043505, 2011.

[2] A. K. Geim, "Graphene: Status and prospects," *Science*, vol. 324, p. 1530, June 2009.

[3] Q. H. Wang, K. Kalantar-Zadeh, A. Kis, J. N. Coleman, and M. S. Strano, "Electronics and optoelectronics of two-dimensional transition metal dichalcogenides," *Nature Nanotechnology*, vol. 7, p. 699, 2012.

[4] V. G. Veselago, "The electrodynamics of substances with simultaneously negative values of epsilon and mu," *Phys. Usp.*, vol. 10, p. 509, 1968.

[5] D. R. Smith, W. J. Padilla, D. C. Vier, S. C. Nemat-Nasser, and S. Schultz, "Composite medium with simultaneously negative permeability and permittivity," *Phys. Rev. Lett.*, vol. 84, no. 18, p. 4184, 2000.

[6] V. A. Podolskiy and E. E. Narimanov, "Strongly anisotropic waveguide as a nonmagnetic left-handed system," *Phys. Rev. B*, vol. 71, pp. 201101–, May 2005.

[7] Z. Jacob, L. V. Alekseyev, and E. Narimanov, "Optical hyperlens: Far-field imaging beyond the diffraction limit," *Opt. Express*, vol. 14, no. 18, p. 8247, 2006.

[8] L. Ferrari, C. Wu, D. Lepage, X. Zhang, and Z. Liu, "Hyperbolic metamaterials and their applications," *Prog. Quantum Electron.*, vol. 40, pp. 1–40, 2015.

[9] I. I. Smolyaninov and V. N. Smolyaninova, "Hyperbolic metamaterials: Novel physics and applications," *Solid-State Electronics*, vol. 136, pp. 102–112, 2017.

[10] "https://www.scopus.com."

[11] Z. Liu, H. Lee, Y. Xiong, C. Sun, and X. Zhang, "Far-field optical hyperlens magnifying sub-diffraction-limited objects," *Science*, vol. 315, no. 5819, p. 1686, 2007.

[12] Y. Xiong, Z. Liu, and X. Zhang, "A simple design of flat hyperlens for lithography and imaging with half-pitch resolution down to 20 nm," *Appl. Phys. Lett.*, vol. 94, p. 203108, 2009.

[13] C. L. Cortes, W. Newman, S. Molesky, and Z. Jacob, "Quantum nanophotonics using hyperbolic metamaterials," *J. Opt*, vol. 14, no. 6, p. 063001, 2012.

[14] D. Lu, J. J. Kan, E. E. Fullerton, and Z. Liu, "Enhancing spontaneous emission rates of molecules using nanopatterned multilayer hyperbolic metamaterials," *Nat. Nanotechnol.*, vol. 9, no. 1, pp. 48–53, 2014.

[15] Z. Jacob, J.-Y. Kim, G. V. Naik, A. Boltasseva, E. E. Narimanov, and V. M. Shalaev, "Engineering photonic density of states using metamaterials," *Appl. Phys. B*, vol. 100, no. 1, p. 215, 2010.

[16] S.-A. Biehs, M. Tschikin, and P. Ben-Abdallah, "Hyperbolic metamaterials as an analog of a blackbody in the near field," *Phys. Rev. Lett.*, vol. 109, no. 10, p. 104301, 2012.

[17] S.-A. Biehs, M. Tschikin, R. Messina, and P. Ben-Abdallah, "Super-planckian near-field thermal emission with phonon-polaritonic hyperbolic metamaterials," *Appl. Phys. Lett.*, vol. 102, p. 131106, Apr. 2013.

[18] C. Argyropoulos, N. M. Estakhri, F. Monticone, and A. Alù, "Negative refraction, gain and nonlinear effects in hyperbolic metamaterials," *Opt. Express*, vol. 21, no. 12, pp. 15037–15047, 2013.

[19] T. Galfsky, H. N. S. Krishnamoorthy, W. Newman, E. E. Narimanov, Z. Jacob, and V. M. Menon, "Active hyperbolic metamaterials: enhanced spontaneous emission and light extraction," *Optica*, vol. 2, no. 1, pp. 62–65, 2015.

[20] B. Janaszek, A. Tyszka-Zawadzka, and P. Szczepanski, "Control of gain/absorption in tunable hyperbolic metamaterials," *Opt. Express*, vol. 25, no. 12, pp. 13153–13162, 2017.

[21] M. A. K. Othman, C. Guclu, and F. Capolino, "Graphene-based tunable hyperbolic metamaterials and enhanced near-field absorption," *Opt. Express*, vol. 21, no. 6, p. 7614, 2013.

[22] L. Zhang, Z. Zhang, C. Kang, B. Cheng, L. Chen, X. Yang, J. Wang, W. Li, and B. Wang, "Tunable bulk polaritons of graphene-based hyperbolic metamaterials," *Opt. Express*, vol. 22, no. 11, p. 14022, 2014.

[23] G. T. Papadakis, D. Fleischman, A. Davoyan, P. Yeh, and H. A. Atwater, "Optical magnetism in planar metamaterial heterostructures," *Nature Communications*, vol. 9, no. 1, pp. 296–, 2018.

[24] M. N. Gjerding, R. Petersen, T. G. Pedersen, N. A. Mortensen, and K. S. Thygesen, "Layered van der waals crystals with hyperbolic light dispersion," *Nature Communications*, vol. 8, no. 1, p. 320, 2017.

[25] W. Cai and V. Shalaev, *Optical Metamaterials: Fundamentals and Applications*. Springer, 2010.

[26] B. H. L. Novotny, *Principles of Nano-Optics*. Cambridge University Press, 2006.

[27] A. V. Zayats and S. A. Maier, *Active Plasmonics and Tuneable Plasmonic Metamaterials*. John Wiley & Sons, 2013.

[28] H.-S. P. Wong and D. Akinwande, *Carbon Nanotube and Graphene Device Physics*. Cambridge: Cambridge University Press, 2010.

[29] X. Li, H. Zhu, K. Wang, A. Cao, J. Wei, C. Li, Y. Jia, Z. Li, X. Li, and D. Wu *Adv. Mater.*, vol. 22, p. 2743, 2010.

[30] Q. Bao and K. Loh *ACS Nano*, vol. 6, p. 3677, 2012.

[31] P. R. Wallace, "The band theory of graphite," *Phys. Rev.*, vol. 71, p. 622, 1947.

[32] M. P. Marder, *Condensed Matter Physics*. John Wiley and Sons, 2010.

[33] S. Maier, *Plasmonics: Fundamentals and applications*. Springer, 2007.

[34] G. A. Niklasson, C. G. Granqvist, and O. Hunderi, "Effective medium models for the optical properties of inhomogeneous materials," *Appl. Opt.*, vol. 20, no. 1, p. 26, 1981.

[35] T. Li and J. B. Khurgin, "Hyperbolic metamaterials: beyond the effective medium theory," *Optica*, vol. 3, no. 12, pp. 1388–1396, 2016.

[36] J. Garnett, "Colours in metal glasses and in metallic films," *Phil. Trans. R. Soc. Lond.*, vol. 203, no. 359-371, p. 385, 1904.

[37] V. A. Markel, "Introduction to the maxwell garnett approximation: tutorial," *J. Opt. Soc. Am. A*, vol. 33, no. 7, p. 1244, 2016.

[38] D. A. G. Bruggeman, "Calculation of various physics constants in heterogenous substances. i. dielectricity constants and conductivity of mixed bodies from isotropic substances," *Annalen der Physik*, vol. 416, no. 7, p. 636, 1935.

[39] H. Su, Y. Li, X.-Y. Li, and K. S. Wong, "Optical and electrical properties of au nanoparticles in two-dimensional networks: an effective cluster model," *Opt. Express*, vol. 17, p. 22223, Nov 2009.

[40] G. P. De Loor, "Dielectric properties of heterogeneous mixtures with a polar constituent," *Appl. Sc. Res. B*, vol. 11, p. 310, May 1964.

[41] H. Looyenga, "Dielectric constants of heterogeneous mixtures," *Physica*, vol. 31, no. 3, p. 401, 1965.

[42] X. Chen, T. M. Grzegorczyk, B.-I. Wu, J. Pacheco, and J. A. Kong, "Robust method to retrieve the constitutive effective parameters of metamaterials," *Physical Review E*, vol. 70, no. 1, 2004.

[43] V. Popov, A. V. Lavrinenko, and A. Novitsky, "Operator approach to effective medium theory to overcome a breakdown of maxwell garnett approximation," *Phys. Rev. B*, vol. 94, no. 8, p. 085428, 2016.

[44] Q. Li, Y. Chen, and V. G. Harris, "Particle-size distribution modified effective medium theory and validation by magneto-dielectric co-ti substituted bam ferrite composites," *Journal of Magnetism and Magnetic Materials*, vol. 453, p. 44, 2018.

[45] I. Tsukerman, "Classical and non-classical effective medium theories: New perspectives," *Phys. Lett. A*, vol. 381, no. 19, p. 1635, 2017.

[46] A. Poddubny, I. Iorsh, P. Belov, and Y. Kivshar, "Hyperbolic metamaterials," *Nat. Photonics*, vol. 7, no. 12, pp. 948–957, 2013.

[47] D. R. Smith, P. Kolinko, and D. Schurig, "Negative refraction in indefinite media," *J. Opt. Soc. Am. B*, vol. 21, no. 5, p. 1032, 2004.

[48] J. N. W. R. D. M. J. D. Joannopoulos, S. G. Johnson, *Photonic Crystals*. Prinston University Press, 2008.

[49] S. V. Zhukovsky, A. A. Orlov, V. E. Babicheva, A. V. Lavrinenko, and J. E. Sipe, "Photonic-band-gap engineering for volume plasmon polaritons in multiscale multilayer hyperbolic metamaterials," *Phys. Rev. A*, vol. 90, no. 1, p. 013801, 2014.

[50] A. A. Orlov, P. M. Voroshilov, P. A. Belov, and Y. S. Kivshar, "Engineered optical nonlocality in nanostructured metamaterials," *Phys. Rev. B*, vol. 84, no. 4, p. 045424, 2011.

[51] G. Rosenblatt and M. Orenstein, "Competing coupled gaps and slabs for plasmonic metamaterial analysis," *Opt. Express*, vol. 19, no. 21, pp. 20372–20385, 2011.

[52] A. Zangwill, *Modern Electrodynamics*. Cambridge University Press.

[53] U. Fano, "Effects of configuration interaction on intensities and phase shifts," *Phys. Rev.*, vol. 124, p. 1866, 1961.

[54] M. F. Limonov, M. V. Rybin, A. N. Poddubny, and Y. S. Kivshar, "Fano resonances in photonics," *Nature Photonics*, vol. 11, p. 543, 2017.

[55] B. Luk'yanchuk, N. I. Zheludev, S. A. Maier, N. J. Halas, P. Nordlander, H. Giessen, and C. T. Chong, "The fano resonance in plasmonic nanostructures and metamaterials," *Nat Mater*, vol. 9, no. 9, pp. 707–715, 2010.

[56] A. E. Miroshnichenko, S. Flach, and Y. S. Kivshar, "Fano resonances in nanoscale structures," *Rev. Mod. Phys.*, vol. 82, no. 3, pp. 2257–2298, 2010.

[57] S. Fan, W. Suh, and J. D. Joannopoulos, "Temporal coupled-mode theory for the fano resonance in optical resonators," *J. Opt. Soc. Am. A*, vol. 20, no. 3, p. 569, 2003.

[58] S. R.-K. Rodriguez, "Classical and quantum distinctions between weak and strong coupling," *Eur. J. Phys.*, vol. 37, no. 2, p. 025802, 2016.

[59] P. Torma and W. L. Barnes, "Strong coupling between surface plasmon polaritons and emitters: a review," *Reports on Progress in Physics*, vol. 78, no. 1, p. 013901, 2015.

[60] S. Wang, S. Li, T. Chervy, A. Shalabney, S. Azzini, E. Orgiu, J. A. Hutchison, C. Genet, P. Samori, and T. W. Ebbesen, "Coherent coupling of ws2 monolayers with metallic photonic nanostructures at room temperature," *Nano Lett.*, vol. 16, no. 7, p. 4368, 2016.

[61] A. Demetriadou, J. M. Hamm, Y. Luo, J. B. Pendry, J. J. Baumberg, and O. Hess, "Spatiotemporal dynamics and control of strong coupling in plasmonic nanocavities," *ACS Photonics*, vol. 4, no. 10, p. 2410, 2017.

[62] M. S. Skolnick, T. A. Fisher, and D. M. Whittaker, "Strong coupling phenomena in quantum microcavity structures," *Semiconductor Science and Technology*, vol. 13, no. 7, p. 645, 1998.

[63] C. Cohen-Tannoudji, B. Diu, and F. Laloe, *Mécanique quantique*, vol. 1. Hermann, 1998.

[64] C. M. Bender and S. Boettcher, "Real spectra in non-hermitian hamiltonians having $\mathcal{PT}$ symmetry," *Phys. Rev. Lett.*, vol. 80, no. 24, p. 5243, 1998.

[65] R. El-Ganainy, K. G. Makris, M. Khajavikhan, Z. H. Musslimani, S. Rotter, and D. N. Christodoulides, "Non-hermitian physics and pt symmetry," *Nature Physics*, vol. 14, p. 11, 2018.

[66] B. Saleh and M. Teich, *Fundamentals of Photonics*. Wiley, 2007.

[67] A. Pick, B. Zhen, O. D. Miller, C. W. Hsu, F. Hernandez, A. W. Rodriguez, M. Soljačić, and S. G. Johnson, "General theory of spontaneous emission near exceptional points," *Opt. Express*, vol. 25, no. 11, pp. 12325–12348, 2017.

[68] Z. Lin, A. Pick, M. Loncar, and A. W. Rodriguez, "Enhanced spontaneous emission at third-order dirac exceptional points in inverse-designed photonic crystals," *Phys. Rev. Lett.*, vol. 117, pp. 107402–, Aug. 2016.

[69] S. Longhi, "Optical realization of relativistic non-hermitian quantum mechanics," *Phys. Rev. Lett.*, vol. 105, no. 1, p. 013903, 2010.

[70] T. Goldzak, A. A. Mailybaev, and N. Moiseyev, "Light stops at exceptional points," *Phys. Rev. Lett.*, vol. 120, no. 1, p. 013901, 2018.

[71] K. L. Tsakmakidis, O. Hess, R. W. Boyd, and X. Zhang, "Ultraslow waves on the nanoscale," *Science*, vol. 358, no. 6361, p. 1, 2017.

[72] "https://www.comsol.com."

[73] A. C. Polycarpou, "Introduction to the finite element method in electromagnetics," *Synthesis Lectures on Computational Electromagnetics*, vol. 1, no. 1, p. 1, 2006.

[74] O. D. Miller, S. G. Johnson, and A. W. Rodriguez, "Effectiveness of thin films in lieu of hyperbolic metamaterials in the near field," *Phys. Rev. Lett.*, vol. 112, no. 15, pp. 157402–, 2014.

[75] K. V. Sreekanth, T. Biaglow, and G. Strangi, "Directional spontaneous emission enhancement in hyperbolic metamaterials," *J. Appl. Phys.*, vol. 114, no. 13, p. 134306, 2013.

[76] X. Yang, J. Yao, J. Rho, X. Yin, and X. Zhang, "Experimental realization of three-dimensional indefinite cavities at the nanoscale with anomalous scaling laws," *Nat. Photonics*, vol. 6, no. 7, pp. 450–454, 2012.

[77] D. Keene and M. Durach, "Hyperbolic resonances of metasurface cavities," *Opt. Express*, vol. 23, no. 14, pp. 18577–18588, 2015.

[78] S. V. Zhukovsky, O. Kidwai, and J. E. Sipe, "Physical nature of volume plasmon polaritons in hyperbolic metamaterials," *Opt. Express*, vol. 21, no. 12, pp. 14982–14987, 2013.

[79] S. V. Zhukovsky, A. Andryieuski, J. E. Sipe, and A. V. Lavrinenko, "From surface to volume plasmons in hyperbolic metamaterials: General existence conditions for bulk high-k waves in metal-dielectric and graphene-dielectric multilayers," *Phys. Rev. B*, vol. 90, no. 15, p. 155429, 2014.

[80] J. Elser, R. Wangberg, V. A. Podolskiy, and E. E. Narimanov, "Nanowire metamaterials with extreme optical anisotropy," *Appl. Phys. Lett.*, vol. 89, no. 26, p. 261102, 2006.

[81] N. Vasilantonakis, M. E. Nasir, W. Dickson, G. A. Wurtz, and A. V. Zayats, "Bulk plasmon-polaritons in hyperbolic nanorod metamaterial waveguides," *Laser & Photonics Reviews*, vol. 9, no. 3, pp. 345–353, 2015.

[82] P. Berini, "Plasmon-polariton waves guided by thin lossy metal films of finite width: Bound modes of symmetric structures," *Phys. Rev. B*, vol. 61, no. 15, pp. 10484–10503, 2000.

[83] F. Vaianella and B. Maes, "Describing the dispersion of plasmonic nanorod arrays via coupling of elementary excitations," *Phys. Rev. B*, vol. 93, no. 16, p. 165417, 2016.

[84] C. Wu, A. Salandrino, X. Ni, and X. Zhang, "Electrodynamical light trapping using whispering-gallery resonances in hyperbolic cavities," *Phys. Rev. X*, vol. 4, no. 2, pp. 021015–, 2014.

[85] Z. Huang and E. E. Narimanov, "Zeroth-order transmission resonance in hyperbolic metamaterials," *Opt. Express*, vol. 21, no. 12, pp. 15020–15025, 2013.

[86] M. Hasan and I. Iorsh, "Interaction of light with a hyperbolic cavity in the strong-coupling regime with fano resonance," in *Days on Diffraction (DD)*, pp. 1–6, 2015.

[87] S. Fan and J. D. Joannopoulos, "Analysis of guided resonances in photonic crystal slabs," *Physical Review B*, vol. 65, no. 23, p. 235112, 2002.

[88] I. V. Iorsh, I. V. Shadrivov, P. A. Belov, and Y. S. Kivshar, "Cavity-enhanced absorption and fano resonances in graphene nanoribbons," *Phys. Rev. B*, vol. 88, no. 19, pp. 195422–, 2013.

[89] B. Dastmalchi, P. Tassin, T. Koschny, and C. M. Soukoulis, "A new perspective on plasmonics: Confinement and propagation length of surface plasmons for different materials and geometries," *Adv. Opt. Mater.*, vol. 4, no. 1, pp. 177–184, 2016.

[90] P. Tassin, T. Koschny, M. Kafesaki, and C. M. Soukoulis, "A comparison of graphene, superconductors and metals as conductors for metamaterials and plasmonics," *Nat. Photonics*, vol. 6, no. 4, pp. 259–264, 2012.

[91] X. Ni, S. Ishii, M. D. Thoreson, V. M. Shalaev, S. Han, S. Lee, and A. V. Kildishev, "Loss-compensated and active hyperbolic metamaterials," *Opt. Express*, vol. 19, no. 25, pp. 25242–25254, 2011.

[92] I. S. Nefedov, C. A. Valagiannopoulos, S. M. Hashemi, and E. I. Nefedov, "Total absorption in asymmetric hyperbolic media," *Sci. Rep.*, vol. 3, p. 2662, 2013.

[93] A. D. Boardman, P. Egan, and M. McCall, "Optic axis-driven new horizons for hyperbolic metamaterials," *EPJ Applied Metamaterials*, vol. 2, p. 11, 2015.

[94] B. Maes, P. Bienstman, and R. Baets, "Switching in coupled nonlinear photonic-crystal resonators," *J. Opt. Soc. Am. B*, vol. 22, no. 8, p. 1778, 2005.

[95] R. Won *Nat Photon*, vol. 4, p. 411, 2010.

[96] F. Bonaccorso, Z. Sun, T. Hasan, and A. C. Ferrari *Nat Photon*, vol. 4, p. 611, 2010.

[97] I. V. Iorsh, I. S. Mukhin, I. V. Shadrivov, P. A. Belov, and Y. S. Kivshar, "Hyperbolic metamaterials based on multilayer graphene structures," *Phys. Rev. B*, vol. 87, no. 7, p. 075416, 2013.

[98] A. Andryieuski, A. V. Lavrinenko, and D. N. Chigrin, "Graphene hyperlens for terahertz radiation," *Phys. Rev. B*, vol. 86, no. 12, p. 121108, 2012.

[99] K. V. Sreekanth, A. De Luca, and G. Strangi, "Experimental demonstration of surface and bulk plasmon polaritons in hypergratings," *Sci. Rep.*, vol. 3, p. 3291, 2013.

[100] I. S. Nefedov, C. A. Valagiannopoulos, and L. A. Melnikov, "Perfect absorption in graphene multilayers," *Journal of Optics*, vol. 15, no. 11, p. 114003, 2013.

[101] A. Y. Nikitin, F. Guinea, F. J. Garcia-Vidal, and L. Martin-Moreno, "Fields radiated by a nanoemitter in a graphene sheet," *Phys. Rev. B*, vol. 84, pp. 195446–, Nov. 2011.

[102] L. A. Falkovsky, "Optical properties of graphene," *Journal of Physics: Conference Series*, vol. 129, no. 1, p. 012004, 2008.

[103] L. A. Falkovsky and A. A. Varlamov, "Space-time dispersion of graphene conductivity," *Eur. Phys. J. B*, vol. 56, no. 4, p. 281, 2007.

[104] C. H. Gan, H. S. Chu, and E. P. Li, "Synthesis of highly confined surface plasmon modes with doped graphene sheets in the midinfrared and terahertz frequencies," *Phys. Rev. B*, vol. 85, no. 12, p. 125431, 2012.

[105] A. Fallahi and J. Perruisseau-Carrier, "Design of tunable biperiodic graphene metasurfaces," *Phys. Rev. B*, vol. 86, no. 19, p. 195408, 2012.

[106] P. B. Johnson and R. W. Christy, "Optical constants of the noble metals," *Phys. Rev. B*, vol. 6, no. 12, pp. 4370–4379, 1972.

[107] F. Vaianella and B. Maes, "Fano resonance engineering in slanted cavities with hyperbolic metamaterials," *Phys. Rev. B*, vol. 94, no. 12, p. 125442, 2016.

[108] E. Kamenetskii, A. Sadreev, and A. Miroshnichenko, *Fano Resonances in Optics and Microwaves*. Springer, 2018.

[109] A. Andryieuski, S. V. Zhukovsky, and A. V. Lavrinenko, "Rough metal and dielectric layers make an even better hyperbolic metamaterial absorber," *Opt. Express*, vol. 22, no. 12, pp. 14975–14980, 2014.

[110] C. Guclu, S. Campione, and F. Capolino, "Hyperbolic metamaterial as super absorber for scattered fields generated at its surface," *Phys. Rev. B*, vol. 86, no. 20, p. 205130, 2012.

[111] O. Hess, J. B. Pendry, S. A. Maier, R. F. Oulton, J. M. Hamm, and K. L. Tsakmakidis, "Active nanoplasmonic metamaterials," *Nat. Mater.*, vol. 11, no. 7, pp. 573–584, 2012.

[112] S. Wuestner, A. Pusch, K. L. Tsakmakidis, J. M. Hamm, and O. Hess, "Overcoming losses with gain in a negative refractive index metamaterial," *Phys. Rev. Lett.*, vol. 105, no. 12, p. 127401, 2010.

[113] N. Meinzer, M. Ruther, S. Linden, C. M. Soukoulis, G. Khitrova, J. Hendrickson, J. D. Olitzky, H. M. Gibbs, and M. Wegener, "Arrays of ag split-ring resonators coupled to ingaas single-quantum-well gain," *Opt. Express*, vol. 18, no. 23, pp. 24140–24151, 2010.

[114] M. A. Noginov, G. Zhu, A. M. Belgrave, R. Bakker, V. M. Shalaev, E. E. Narimanov, S. Stout, E. Herz, T. Suteewong, and U. Wiesner, "Demonstration of a spaser-based nanolaser," *Nature*, vol. 460, pp. 1110–1113, 2009.

[115] M. A. Noginov, G. Zhu, M. Bahoura, J. Adegoke, C. E. Small, B. A. Ritzo, V. P. Drachev, and V. M. Shalaev, "Enhancement of surface plasmons in an ag aggregate by optical gain in a dielectric medium," *Opt. Lett.*, vol. 31, no. 20, pp. 3022–3024, 2006.

[116] S. Xiao, V. P. Drachev, A. V. Kildishev, X. Ni, U. K. Chettiar, H.-K. Yuan, and V. M. Shalaev, "Loss-free and active optical negative-index metamaterials," *Nature*, vol. 466, pp. 735–740, 2010.

[117] A. Fang, T. Koschny, M. Wegener, and C. M. Soukoulis, "Self-consistent calculation of metamaterials with gain," *Phys. Rev. B*, vol. 79, no. 24, p. 241104, 2009.

[118] M. Wan, P. Gu, W. Liu, Z. Chen, and Z. Wang, "Low threshold spaser based on deep-subwavelength spherical hyperbolic metamaterial cavities," *Appl. Phys. Lett.*, vol. 110, p. 031103, Jan. 2017.

[119] J. S. T. Smalley, F. Vallini, B. Kant, and Y. Fainman, "Modal amplification in active waveguides with hyperbolic dispersion at telecommunication frequencies," *Opt. Express*, vol. 22, no. 17, pp. 21088–21105, 2014.

[120] R.-Q. Li, F. J. Garcia-Vidal, and A. I. Fernandez-Dominguez, "Plasmon-exciton coupling in symmetry-broken nanocavities," *ACS Photonics*, vol. 5, no. 1, pp. 177–185, 2018.

[121] J. Feist, J. Galego, and F. J. Garcia-Vidal, "Polaritonic chemistry with organic molecules," *ACS Photonics*, vol. 5, no. 1, pp. 205–216, 2018.

[122] P. Shekhar and Z. Jacob, "Strong coupling in hyperbolic metamaterials," *Phys. Rev. B*, vol. 90, no. 4, p. 045313, 2014.

[123] A. Lupu, H. Benisty, and A. Degiron, "Switching using pt symmetry in plasmonic systems: positive role of the losses," *Opt. Express*, vol. 21, no. 18, pp. 21651–21668, 2013.

[124] S. Phang, A. Vukovic, S. C. Creagh, P. D. Sewell, G. Gradoni, and T. M. Benson, "Localized single frequency lasing states in a finite parity-time symmetric resonator chain," *Sci. Rep.*, vol. 6, p. 20499, 2016.

[125] E. E. Narimanov, "Photonic hypercrystals," *Phys. Rev. X*, vol. 4, no. 4, p. 041014, 2014.

[126] I. Iorsh, A. Poddubny, A. Orlov, P. Belov, and Y. S. Kivshar, "Spontaneous emission enhancement in metal-dielectric metamaterials," *Phys. Lett. A*, vol. 376, no. 3, pp. 185–187, 2012.

[127] J. K. Kitur, G. Zhu, Y. A. Barnakov, and M. A. Noginov, "Stimulated emission of surface plasmon polaritons on smooth and corrugated silver surfaces," *J. Opt.*, vol. 14, no. 11, p. 114015, 2012.

[128] M. A. Noginov, V. A. Podolskiy, G. Zhu, M. Mayy, M. Bahoura, J. A. Adegoke, B. A. Ritzo, and K. Reynolds, "Compensation of loss in propagating surface plasmon polariton by gain in adjacent dielectric medium," *Opt. Express*, vol. 16, no. 2, pp. 1385–1392, 2008.

[129] W. Chen, M. D. Thoreson, S. Ishii, A. V. Kildishev, and V. M. Shalaev, "Ultra-thin ultra-smooth and low-loss silver films on a germanium wetting layer," *Opt. Express*, vol. 18, no. 5, pp. 5124–5134, 2010.

[130] O. V. Shramkova and G. P. Tsironis, "Propagation of electromagnetic waves in *pt*-symmetric hyperbolic structures," *Phys. Rev. B*, vol. 94, no. 3, pp. 035141–, 2016.

[131] O. Novotny, I. Mufti, and A. G. Vicentini, "Analytical partial derivatives of the phase- and group velocities for rayleigh waves propagating in a layer on a half-space," *Stud. Geophys. Geod.*, vol. 49, no. 3, pp. 305–321, 2005.

[132] F. Vaianella, J. M. Hamm, O. Hess, and B. Maes, "Strong coupling and exceptional points in optically pumped active hyperbolic metamaterials," *ACS Photonics*, vol. 5, no. 6, p. 2486, 2018.

[133] J. Lekner, "Reflection and refraction by uniaxial crystals," *Journal of Physics: Condensed Matter*, vol. 3, no. 32, p. 6121, 1991.

[134] D. Jalas, A. Petrov, M. Eich, W. Freude, S. Fan, Z. Yu, R. Baets, M. Popovi, A. Melloni, J. D. Joannopoulos, M. Vanwolleghem, C. R. Doerr, and H. Renner, "What is - and what is not - an optical isolator," *Nature Photonics*, vol. 7, p. 579, July 2013.

[135] A. Boltasseva and H. A. Atwater, "Low-loss plasmonic metamaterials," *Science*, vol. 331, pp. 290–, Jan. 2011.

[136] G. V. Naik, V. M. Shalaev, and A. Boltasseva, "Alternative plasmonic materials: Beyond gold and silver," *Adv. Mater.*, vol. 25, no. 24, p. 3264, 2013.

[137] P. R. West, S. Ishii, G. V. Naik, N. K. Emani, V. M. Shalaev, and A. Boltasseva, "Searching for better plasmonic materials," *Laser & Photon. Rev.*, vol. 4, p. 795, 2010.